

Université
de Toulouse

THÈSE

En vue de l'obtention de

HABILITATION A DIRIGER DES RECHERCHES DE L'UNIVERSITÉ DE TOULOUSE

Délivré par : *l'Institut National Polytechnique de Toulouse (INP Toulouse)*

Présentée et soutenue le *XX/XX/2024* par :

Omar Dounia

Contribution to the modeling of reaction waves in confined media: application to novel combustion technologies and safety.

JURY

RONAN VICQUELIN	Professeur des Universités	Rapporteur
ASHWIN CHINNAYYA	Professeur des Universités	Rapporteur
PIERRE BOIVIN	Chargé de Recherche	Rapporteur
NABIHA CHAUMEIX	Directrice de Recherche	Examinatrice
PASCALE DOMINGO	Directrice de Recherche	Examinatrice
CHRISTOPHE PROUST	Directeur de Recherche	Examineur
LAURENT SELLE	Directeur de Recherche	Examineur

École doctorale et spécialité :

MEGEP : Dynamique des fluides

Unité de Recherche :

CERFACS

Parrain :

Dr. Laurent Selle

Rapporteurs :

Pr. Ronan Vicquelin, Pr. Ashwin Chinnayya et Dr. Pierre Boivin

Contents

I	Research topics, outlook and future work	3
1	General introduction	5
2	Towards the reliable prediction of large-scale explosions	7
2.1	Dynamics of very-lean H ₂ /air deflagrations in confined and obstructed chambers	7
2.2	Impact of stratification on flame acceleration	19
2.3	Deflagration to Detonation Transition (DDT)	29
3	Fundamentals of the chemical inhibition of propagating flames	33
3.1	Context	33
3.2	The controlling parameters of 1D flame inhibition	34
3.3	Modeling challenges of the inhibition of deflagration waves	48
4	Mechanisms controlling the dynamics of reaction waves in novel combustion technologies	53
4.1	Flames embedded in porous media	53
4.2	Reaction waves in Pressure Gain Combustion (PGC) systems	62
5	Outlook and futur work	77
5.1	Impact of mixture inhomogeneities on flame acceleration	77
5.2	N-dimensional description of flame mitigation	78
5.3	LES strategy for capturing DDT	78
5.4	Plasma effects on hydrogen combustion	79
5.5	LES of Rotating Detonation Engines	80

II Curriculum, Supervision and publications	81
6 Narrative Curriculum Vitae, supervision and training	83
6.1 Narrative CV	83
6.2 Supervision and associated projects	84
6.3 Funded Projects (coordination, participation ...)	88
7 Publications, conferences and lectures	91
7.1 List of publications	91
7.2 Invited talks	93
Bibliography	102

Part I

Research topics, outlook and future work

General introduction

Since the beginning of my scientific career as a researcher, most of my research activities have revolved around the theoretical and numerical modelling of propagating reaction waves, with a focus on safety applications and novel technologies. My research were grouped into three categories in this manuscript:

- In chapter 2, I describe my research centered around the accurate modeling of large-scale explosions, focusing on revisiting classical modeling strategies tailored for large-scale applications to properly account for the intricacies of hydrogen combustion. Another aspect, scarcely addressed in the literature, is the impact of mixture inhomogeneities on propagating deflagrations, even though most realistic explosion scenarios undeniably involve some level of stratification. My contributions to the modeling of stratified deflagrations is therefore also discussed. Finally, the chapter concludes on the Deflagration to Detonation transition and tools to track its triggering conditions in numerical simulations.
- Chapter 3 delves into my research on the controlling parameters of flame inhibition, focusing first on the fundamental description of the 1D flame/inhibitor interaction problem, including : (i) the impact of inhibition chemistry on the gas-phase radical scavenging process associated to the efficient chemical inhibition, and (ii) the formulation of explicit criteria that efficient powders must satisfy to effectively activate the efficient chemical inhibition. Finally, emphasis is placed on the modeling challenges still facing the inhibition of deflagration waves.
- Chapter 4 is dedicated to the mechanisms controlling the dynamics of reaction waves in novel combustion technologies, including porous media burners, constant-volume-combustion chambers and rotating detonation chambers.

This manuscript is intended as an extended summary of my research. An effort was made to restrict the presentation to the main messages, keeping technical details to a minimum. Readers acquainted with the subject can (hopefully) appreciate the core ideas of each research aspect and the details, when provided, are there to provide the reader naïve

to specific fields with the necessary tools/background to understand the main messages. The curious reader may, however, find further details in the supporting articles. The manuscript concludes with medium and long-term research perspectives for the coming years.

Towards the reliable prediction of large-scale explosions

Sommaire

2.1	Dynamics of very-lean H₂/air deflagrations in confined and obstructed chambers	7
2.2	Impact of stratification on flame acceleration	19
2.3	Deflagration to Detonation Transition (DDT)	29

2.1 Dynamics of very-lean H₂/air deflagrations in confined and obstructed chambers

2.1.1 Context and funding

All the work presented in this section has been possible thanks to the industrial support of CERFACS's partners. TotalEnergies, GRTGaz and AirLiquid expressed the need to develop a high-fidelity CFD code capable of accurately predicting the dynamics of hydrogen explosions at scales of industrial relevance. This need led to the project LEFEX funded by all three partners. Two research axes were at the center of this project: (1) development of accurate models able to take into account the specificities of hydrogen-combustion and their impact on the dynamics of explosions; (2) building a state-of-the-art Adaptive Mesh Refinement (AMR) strategy that could allow to increase the range of affordable geometrical scales. I will mostly talk in this manuscript about my contribution to the research axis (1).

Within axis (1), a particular focus was on very lean H₂/air flames for two reasons: (1) in terms of safety measures related to H₂ leaks, it is standard practice in the industry to

avoid the formation of H_2/air mixtures with volumetric concentrations of H_2 above 10%; (2) mixtures close to this threshold are known to be prone to instabilities that can favor an escalation in the explosion hazards. The understanding and accurate modeling of the propagation of very lean H_2/air flames was therefore at the center of axis (1) and the next sections.

2.1.2 Lean H_2/air flames: early stages of flame acceleration

2.1.2.1 Very-lean H_2/air propagation: intrinsic instability

As part of the PhD thesis of **J. J. Hok**, we focused our attention on the mechanisms governing the early stages of very-lean H_2/air flame acceleration in confined environment. Bearing in mind the necessity to reproduce these mechanisms in the context of large scale explosions, this phase also serves as a baseline for exploring potential modeling options suitable in a TF-LES framework.

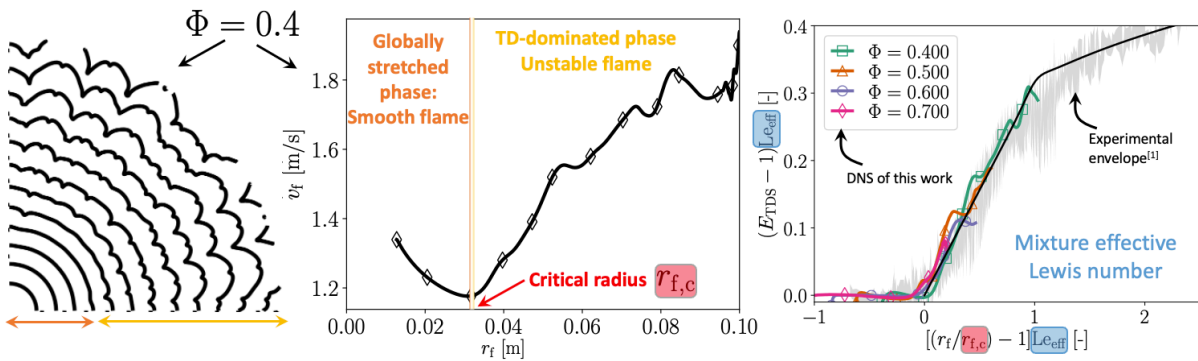


Figure 2.1: Illustration for the self-propagation of thermo-diffusively unstable cylindrical flames obtained with 2D Flame Resolved Simulations (FRS): (left) iso-contours of temperature showing the flame shape for a H_2/air at $\phi = 0.356$; (middle) corresponding flame propagation speed as function of the flame radius; (right) self-similarity space governing the propagation of thermo-diffusively unstable spherical flames for increasing equivalence ratio ϕ (FRS vs Goullier [1] experiments). Adapted from [2].

Compared to conventional fuels, very lean H_2/air flames tend to self-accelerate, a certain distance from ignition, even in the absence of confinement or obstruction. This is highlighted in Fig. 2.1(middle) using flame-resolved 2D cylindrical flame simulations, where as soon as the flame radius r_f exceeds a critical value $r_{f,c}$ a sharp increase of the flame speed is observed. This self-acceleration is accompanied by a marked cellular structure displayed in Fig. 2.1(left). Of course, this behavior is well understood and is related to the thermo-diffusively unstable nature of these flames, induced by an unbalance between thermal diffusion and molecular diffusion of species (both reactants). Dispersion relations for both planar [3–8] and spherical flame configurations [9–13] have been obtained and allow to understand the driving terms of this instability. Their general expression is

recalled here:

$$\text{Planar: } \frac{\omega^{\text{pla}}}{s_L^0 k} = \omega_{\text{DL}}^{\text{pla}} - \frac{\delta_d}{1/k} \Omega_d^{\text{pla}} \quad (2.1)$$

$$\text{Spherical: } \frac{\dot{A}/A}{\dot{r}_f/r_f} = \omega_{\text{DL}}^{\text{sph}} - \frac{\delta_d}{r_f} \Omega_d^{\text{sph}} \quad (2.2)$$

$$\text{with, } \Omega_d^* = [B_1^* + \beta (\text{Le}_{\text{eff}} - 1) B_2^* + \text{Pr} B_3^*] \text{ and } \forall i B_i \geq 0 \text{ and } B_i^{\text{sph}} \geq 0 \quad (2.3)$$

where δ_d is the diffusive flame thickness. k is the wave number of the harmonic perturbation and A its amplitude for the spherical configuration. $\omega/(s_L^0 k)$ and ω_{DL} are the normalized growth rate of the global and hydrodynamic (Darrieus-Landau) instability associated to the planar flame configuration and $(\dot{A}/A)/(\dot{r}_f/r_f)$ and ω_{DL}^{sph} their spherical counterpart. Independently of the configuration (planar or spherical), Eq. (2.1)-(2.2) show that two terms B_1 and B_3 , carrying heat diffusion and viscosity effects respectively, tend to stabilize the flame against hydrodynamic destabilizing effects (ω_{DL}). The factor $\beta(\text{Le}_{\text{eff}} - 1)$ drives the thermo-diffusive part of the instability. $\beta \equiv Ta(T_b - Tu)/T_b^2$ is the Zeldovich number, which measures the thermal sensitivity of the reaction zone and Le_{eff} is a mixture property characterizing the unbalance between thermal diffusion and molecular diffusion of species (both reactants). It is defined here as a weighted mean of the Lewis number of the reactants.

$$\text{Le}_{\text{eff}} \equiv \frac{Le_E + Le_D(1 + \beta X)}{2 + \beta X} \text{ where } \phi > 1 : X \equiv \phi - 1 \text{ and } \phi < 1 : X \equiv \frac{1}{\phi} - 1 \quad (2.4)$$

E and D stand for the reactant in excess and the deficient one respectively. If we concentrate on spherical flames, Eq. (2.2) highlights three important features of spherical flame propagation:

- for mixtures with $\text{Le}_{\text{eff}} < \text{Le}^*$ s.t. $\Omega_d^{\text{sph}} < 0$, the flame is unconditionally unstable $\forall r_f > 0$ and the instability is dominated by its thermo-diffusive part except at sufficiently large radius $r_f \rightarrow \infty$.
- for mixtures with $\text{Le}_{\text{eff}} > \text{Le}^*$, we have $\Omega_d^{\text{sph}} > 0$ and diffusion stabilizes the flame at small radius. However, at sufficiently large radius $r_f > r_{f,c}$ s.t. $\omega_{\text{DL}}^{\text{sph}} > \frac{\delta_d}{r_f} \Omega_d^{\text{sph}}$, the hydrodynamic instability kicks in and promotes instability (self-acceleration).
- for mixtures with $\text{Le}^* < \text{Le}_{\text{eff}} < 1$ and for a sufficiently large flame radius $r_f > r_{f,c}$, a combination of hydrodynamic ($\omega_{\text{DL}}^{\text{sph}}$) and thermo-diffusive ($\frac{\delta_d}{r_f} \beta (\text{Le}_{\text{eff}} - 1) B_2^{\text{sph}}$) effects contributes to the unstable nature of flame propagation. This is the case for most mixtures considered in this manuscript.

(M1) A modeling perspective: a pragmatic modeling of unstable flame propagation

From a modeling perspective, the main implication of these theoretical considerations is that two parameters seem to control the typical behavior observed in Fig. 2.1(middle):

$r_{f,c}$ and Le_{eff} . The question arises therefore as to whether these two parameters can be used as scaling parameters for the behavior of hydrogen/air flames. The PhD thesis of Goullier [1] provided a positive answer to this question as shown in Fig. 2.1(right) where a self-similarity space was uncovered for lean hydrogen/air flames up to near-stoichiometry. In Fig. 2.1(right), E_{TDS} is defined as the ratio between the flame propagation speed v_f and that of its stable (still stretch-sensitive) counterpart, see [1, 2] for further details. The DNS results of J. J. Hok also confirmed this behavior, as shown in Fig. 2.1(right), which paved the way for a simple and pragmatic modeling option for unstable self-propagating H_2 /air flames, requiring only : (1) $r_{f,c}$, which can be extracted from experimental correlations; (2) Le_{eff} , which can be computed for an arbitrary mixture using relations of the like of Eq. 2.4; (3) the self-similarity law extracted from Fig. 2.1(right). This will be exploited in Section 2.1.4.

2.1.2.2 Very-lean H_2 /air deflagration waves in confined environments

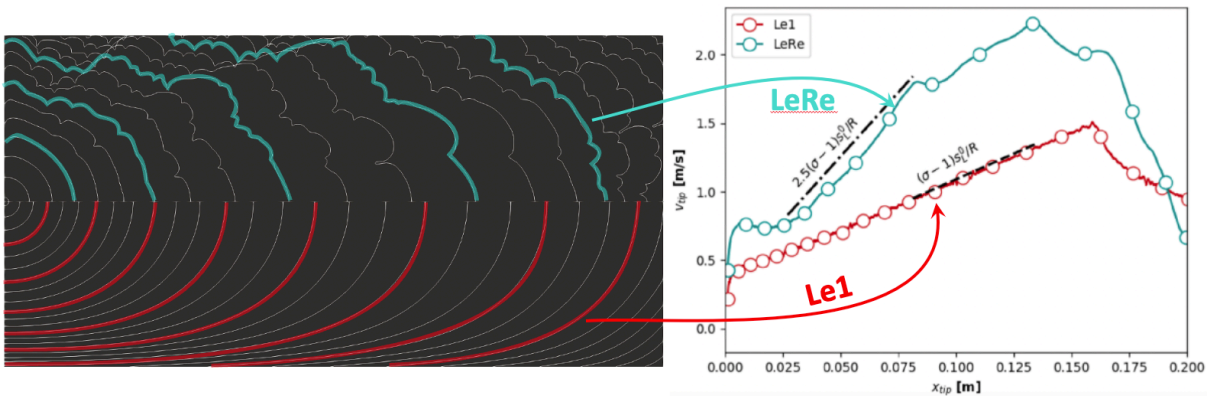


Figure 2.2: Illustration for the 2D finger flame acceleration for unity Lewis number (Le1) and realistic Lewis number (LeRe) 1-step hydrogen chemistries. The case corresponds to $\phi = 0.356$, $T_u = 296 K$ and $P = 1 atm$. Both chemistries (Le1 and LeRe) share the same fundamental flame properties, namely s_L^0 , δ_L^0 and T_{ad} . Tube dimensions: $(R_{tube}, L_{tube}) = \delta_L^0 Pe_{tube} (1, 4)$ with $Pe_{tube} = 100$. Adapted from [14].

The dynamics of very-lean H_2 /air deflagration waves, addressed so far, do not take into account the presence of confinement. In many safety applications, however, ignition occurs in confined environments, a condition known to promote flame acceleration. This is illustrated in Fig. 2.2 where a flame is ignited at the center of left wall and propagates in a domain confined by the side walls. Generally, *i.e.* for conventional fuels (red curves, case Le1), the flame will exhibit a finger-like shape associated with an elongation of its surface and accompanied by an acceleration (exponential in time) as illustrated in Fig. 2.2(right). This phenomenon is not new and its first suggestion dates back to the late 90s [15]. Its theoretical description was later formalized by Bychkov and coworkers [16] and further generalized to account for weak compressibility effects in [17]. The acceleration associated

to the finger flame effect, see Fig. 2.2(right), is provided by the theory:

$$v_f \equiv \frac{dx_f}{dt} = \sigma s_L^0 + \alpha_f x_f \quad (2.5)$$

$$\text{Planar2D: } \alpha_f = (\sigma - 1)s_L^0/R_{\text{tube}} \ ; \ \text{Axysymmetric: } \alpha_f = 2\sqrt{\sigma(\sigma - 1)}s_L^0/R_{\text{tube}} \quad (2.6)$$

where $\sigma \equiv \rho_u/\rho_b$ is the gas dilatation ratio through the flame. Eq. (2.5) predicts the same acceleration observed in the 2D DNS simulations of J. J. Hok in Fig. 2.2(right), *i.e.* a linear evolution of the flame propagation speed with the flame position and a slope given by $\alpha_f = (\sigma - 1)s_L^0/R_{\text{tube}}$.

In the PhD of J. J. Hok, we were interested in the coupling between the finger flame acceleration mechanism and the self-acceleration induced by the flame instability. To do so, a chemistry with realistic transport properties (LeRe) and sharing the same fundamental properties obtained for the Unitary Lewis case (characteristic of a very lean H₂/air flame at $\phi = 0.356$) is tested on the finger flame problem. Figure 2.2(left) shows that in the LeRe case, the footprint of the finger flame is still visible but coupled to a markedly cellular structure. The consequence of this coupling is a clear enhancement of the flame acceleration observed in tubes (slope multiplied by nearly 2.5 in Fig. 2.2(right)). The present problem offers also the possibility to further investigate the complex coupling between the finger flame and instability-induced acceleration mechanisms by varying independently their relative "strengths". This can be done by simply changing the tube radius R_{tube} , which according to Eq. (2.5)-(2.6) controls the slope of the finger flame acceleration ($\propto 1/R_{\text{tube}}$) and will therefore either promote ($R_{\text{tube}} \searrow$) or mitigate ($R_{\text{tube}} \nearrow$) the finger flame acceleration. The limiting case is of course when $R_{\text{tube}} \rightarrow \infty$ and the unconfined case is recovered where no finger flamer acceleration is observed. Fig. 2.3 shows the impact of R_{tube} (degree of confinement) on the coupling observed in Fig. 2.2(left). Of course, when Unity Lewis numbers mixture are considered, a self-similar behavior is observed when the flame position is scaled with the tube radius, as expected from Eq. (2.5)-(2.6). For the LeRe case, the results of Fig. 2.3 are clearly characteristic of the competition between two phenomenon for dominance: when R_{tube} decreases, confinement-induced acceleration is enhanced and the net-behavior tends towards the classical finger flame, inversely when R_{tube} increases, the "strength" of the finger-flame acceleration is reduced and the cellular structure has more room to develop, which enhances its contribution to the overall acceleration.

(M2) A modeling perspective: existence of a saturation at early stages

In Fig. 2.3(right), an effective contribution of the flame instability is computed by simply dividing the flame propagation velocity of the LeRe case by its Le1 counterpart. The results show the existence of a near-saturation of this "efficiency" for sufficiently large distance from ignition and typically for $x_f \geq R_{\text{tube}}$. Also, this near-plateau increases with the tube radius, in accordance with the conclusions made just above. These two observations offer the possibility of a pragmatic saturation of the efficiency model suggested in Section 2.1.2.1 (M1) which could be bounded by its value when $r_f = R_{\text{tube}}$, hence when R_{tube} increases,

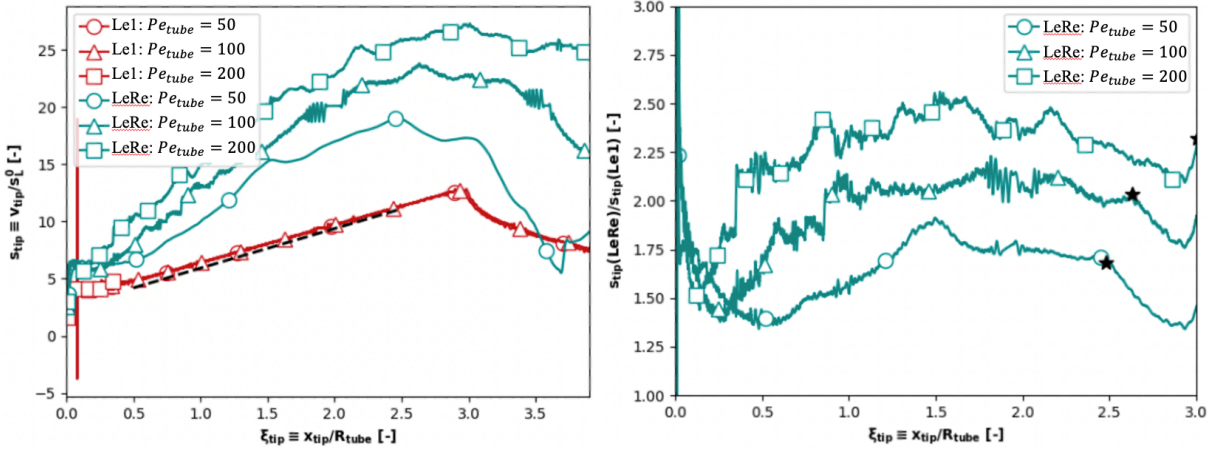


Figure 2.3: Impact of the tube radius on the propagation of thermo-diffusively unstable H_2/air flames. Evolution of the non-dimensional flame tip speed (left) and effective thermo-diffusive efficiency (right) with non-dimensional flame tip position. The case corresponds to $\phi = 0.356$, $T_u = 296 \text{ K}$ and $P = 1 \text{ atm}$. Both chemistries (Le1 and LeRe) share the same fundamental flame properties, namely s_L^0 , δ_L^0 and T_{ad} . Tube dimensions: $(R_{tube}, L_{tube}) = \delta_L^0 Pe_{tube} (1, 4)$ with $Pe_{tube} = 50, 100, 200$. Adapted from [14].

the bound for the efficiency increases also, thereby mimicking the behavior observed in Fig. 2.3(right) for the contribution of the instability to flame acceleration in confined environments. This conclusion combined with the model suggested in Section 2.1.2.1 (M1) will be exploited further in Section 2.1.4.

2.1.3 The problem with TFLES of very lean H_2/air propagating flames

The first DNS simulations presented in section 2.1.2 have suggested potential modeling solutions (see 2.1.2.1(M1) and 2.1.2.2(M2)) for the TFLES of very-lean H_2/air propagating flames, at least for the early stages of flame propagation when the flow is essentially laminar. But before implementing these models, J. J. Hok scrutinized the performance of the classical TFLES in [2]. *NB: of course the term TFLES is used here somewhat imprecisely since there is no use for LES models in the early stages of flame acceleration when the flow is essentially laminar. Here the term TFLES must be understood in the sense of the «simulation of flames in coarse, LES-type, meshes using the artificial thickening approach.»*

The Thickened Flame (TF or TFLES) model circumvents the problem of solving stiff reaction terms in coarse meshes by artificially thickening the flame to resolve it on a coarse grid [18, 19]. Its principle stems from simple scaling laws for the laminar flame speed and flame thickness ([20, 21]):

$$s_L^0 \propto \sqrt{D\dot{\omega}}, \text{ and } \delta_L^0 \propto \sqrt{\frac{D}{\dot{\omega}}} \quad (2.7)$$

$\dot{\omega}$ is any chemical source term and D represents a characteristic diffusivity (heat or species). The flame front can then be thickened by a factor F while preserving its laminar unstretched flame speed, following:

$$\begin{cases} D_{\text{th}} \mapsto F D_{\text{th}} \\ D_k \mapsto F D_k, \quad \forall k \in \llbracket 1, N_{\text{spec}} \rrbracket \\ \dot{\omega}_k \mapsto \frac{\dot{\omega}_k}{F}, \quad \forall k \in \llbracket 1, N_{\text{spec}} \rrbracket \end{cases} \implies \begin{cases} s_L^0 \mapsto s_L^0 \\ \delta_L^0 \mapsto F \delta_L^0 \end{cases} \quad (2.8)$$

The factor F is chosen generally to guarantee at least 7 grid cells per thickened flame thickness, *i.e.* $F \delta_L^0 = 7 \Delta x$. *NB: to avoid impacting diffusion processes in regions far away from the flame front, a flame sensor S is usually used to limit the impact of the TF transformation to the flame region [22], so that: $F'(x) = 1 + (F - 1)S(x)$.*

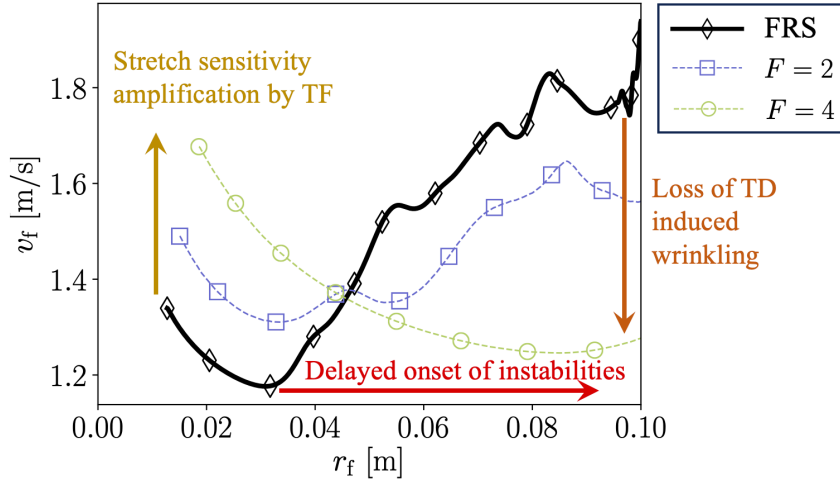


Figure 2.4: Impact of artificial flame thickening (TF) on the self-propagation of very lean H₂/air cylindrical flames: illustration with $\phi = 0.356$, $T_u = 296 \text{ K}$ and $P = 1 \text{ atm}$. FRS, $F = 2$ and $F = 4$ simulations correspond to the resolutions $\Delta x / \delta_L^0 = \{1/21, 1/3.5, 1/1.75\}$ respectively. In the TF simulations, the thickened flame front is always resolved on 7 mesh cells, *i.e.* $F \delta_L^0 = 7 \Delta x$. Adapted from [2].

The test case computed with a Flame Resolved (FRS) setup ($\Delta x / \delta_L^0 = 1/21$) in Fig. 2.1 (left and middle) was simulated again using coarser meshes ($\Delta x / \delta_L^0 = \{1/3.5, 1/1.75\}$) and the TF approach ($F = \{2, 4\}$, corresponding to $F \delta_L^0 = 7 \Delta x$). The results are shown in Fig. 2.4 and highlight the strong mesh dependency observed with the TF approach and its inability to reproduce the flame dynamics observed in the FRS simulations. Two problems with the TF approach are also emphasized in Fig. 2.4:

- (P1: Stretch sensitivity enhancement by F) Focusing of the first stages of propagation just after ignition, the TF simulations exhibit an increasing sensitivity to stretch with increasing F , which can be related to the sensitivity of flames to stretch. Indeed, in the weak stretch limit, it has been established that the flame consumption speed

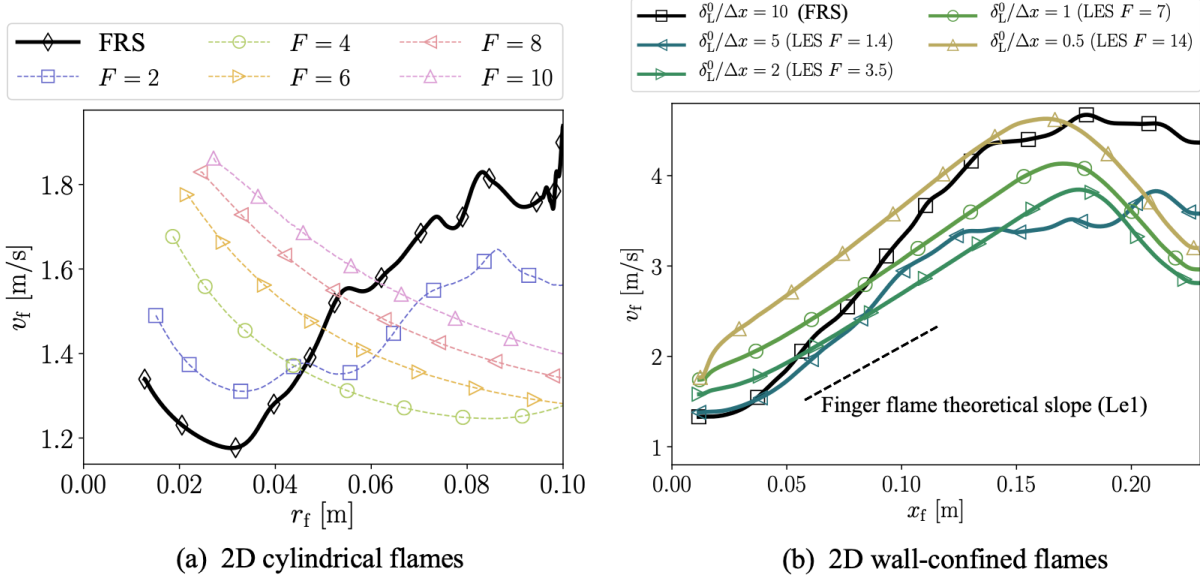


Figure 2.5: Impact of artificial flame thickening (TF) on the self-propagation of very lean H_2/air cylindrical flames (a) and wall-confined 2D flames (b): illustration with $\phi = 0.356$, $T_u = 296 \text{ K}$ and $P = 1 \text{ atm}$. In the TF simulations, the thickened flame front is always resolved on 7 mesh cells, *i.e.* $F\delta_L^0 = 7\Delta x$. Adapted from [2].

evolves linearly with stretch [10, 23–26]:

$$\frac{s_c}{s_L^0} = 1 - \mathcal{L}_c \frac{\mathbb{K}}{s_L^0} \quad \text{with:} \quad \mathcal{L}_c \propto \delta_L^0 (\text{Le}_{\text{eff}} - 1) \xrightarrow{\text{TF}} \mathcal{L}_c \propto \mathbf{F} \delta_L^0 (\text{Le}_{\text{eff}} - 1) \quad (2.9)$$

where \mathcal{L}_c is the Markstein length. It is clear that introducing the TF transform enhances the sensitivity of flames to stretch by a factor F , which for the case of very lean H_2/air flames ($\text{Le}_{\text{eff}} - 1 < 0$) leads to an artificial increase in the flame speed with increasing F ;

- (P2: Loss in the contribution of thermo-diffusive instability) Beyond the critical radius for the onset of instabilities, the TF simulations are shown to exhibit a reduced contribution of the instabilities with increasing F and a delayed onset of instabilities (increase in $r_{f,c}$) by a factor nearly equal to F . These two behaviors can be explained by two factors: (i) the use of coarse meshes, unable to adequately capture the development of the instabilities; (ii) and the thickening procedure, which, much like in Eq. (2.9), has a strong effect on the dispersion relations (2.2):

$$\frac{\dot{A}/A}{\dot{r}_f/r_f} = \omega_{\text{DL}}^{\text{sph}} - \frac{\delta_L}{r_f} \Omega_d^{\text{sph}} \xrightarrow{\text{TF}} \frac{\dot{A}/A}{\dot{r}_f/r_f} = \omega_{\text{DL}}^{\text{sph}} - \mathbf{F} \frac{\delta_L}{r_f} \Omega_d^{\text{sph}} \quad (2.10)$$

where F is seen to enhance the contribution of the stabilizing term Ω_d^{sph} and coincidentally increase the range of stability $r_f \leq r_{f,c}$, with $r_{f,c} = \mathbf{F} \delta_L \Omega_d^{\text{sph}} / \omega_{\text{DL}}^{\text{sph}}$.

Additional simulations for increasing values of F were further performed and highlighted in Fig. 2.5 for both cylindrical (a) and 2D wall-confined (b) flame configurations. For both

cases, a dramatic effect of the TF approach on the propagation of lean H₂/air flames is observed with a strong mesh (hence F) dependance of the flame propagation speed that hinders the reliability of the classical TF for the simulation of thermo-diffusively sensitive propagating flames. These observations called for a revisit of the TF approach to solve the two problems (P1)-(P2) discussed above. This was the central contribution of the PhD of **J. J. Hok**, discussed in the next section.

2.1.4 A modeling strategy for the simulation of very lean H₂/air propagating flames in LES meshes

Our first attempt at modeling lean H₂/air flames in LES, tested in the PhD of **F. Meziat**, was quite pragmatic [27]. It consisted in two elementary bricks already available in the literature:

- To solve the issue of the amplification of the sensitivity of flames to stretch by TF, the transport based correction of P. Quillatre [28, 29], called **TF-adapt**, was adopted, in which the Lewis number of each species is modified so that the Marstein length in absence of thickening ($F = 1$) is recovered, thereby counteracting the undesired effect observed in (P1):

$$Le_k \mapsto Le_k^* = 1 + \frac{Le_k - 1}{F} \implies \mathcal{L}_c^* \propto \mathbf{F} \delta_L^0 (Le_{\text{eff}}^* - 1) = \delta_L^0 (Le_{\text{eff}} - 1) = \mathcal{L}_c^{F=1} \quad (2.11)$$

- The correlation of Berger et al. [30] was used to account for the contribution of the cellular structure to flame acceleration that are not captured in LES meshes (P2). The associated efficiency function E_{TDS} is introduced as follows:

$$\begin{cases} D_{\text{th}} \mapsto E_{\text{TDS}} F D_{\text{th}} \\ D_k \mapsto E_{\text{TDS}} F D_k^*, \quad \forall k \in \llbracket 1, N_{\text{spec}} \rrbracket \\ \dot{\omega}_k \mapsto E_{\text{TDS}} \frac{\dot{\omega}_k}{F}, \quad \forall k \in \llbracket 1, N_{\text{spec}} \rrbracket \end{cases} \implies \begin{cases} s_c \mapsto E_{\text{TDS}} s_L^0 \\ \delta_L \mapsto F \delta_L^0 \end{cases} \quad (2.12)$$

However, serious limitations of this first solution were soon observed:

- The **TF-adapt** model (2.11) is based on the linear relation between consumption speed and stretch, which is only valid in the weak stretch limit: $Ka = \delta_L^0 \mathbb{K} / s_L^0 \ll 1$. The problem is that the thickening factor F decreases the range of applicability of the weak stretch regime, in terms of stretch:

$$Ka = \frac{\delta_L^0 \mathbb{K}}{s_L^0} \ll 1 \iff \mathbb{K} \ll \frac{s_L^0}{\delta_L^0} \xrightarrow{\text{TF}} Ka = \frac{\mathbf{F} \delta_L^0 \mathbb{K}}{s_L^0} \ll 1 \iff \mathbb{K} \ll \frac{s_L^0}{\mathbf{F} \delta_L^0} \quad (2.13)$$

which means that the range of stretch values for which the **TF-adapt** correction is valid decreases with increasing F , which drastically hinders its applicability to large-scale simulations where large values $F = O(10)$ are expected. Moreover, and

somewhat related, it is shown in Fig. 2.6(a) that the **TF-adapt** correction is unable to correctly solve the amplification introduced by the TF approach when applied on very stretch sensitive flames.

- The correlation of Berger et al. [30] is based on statistically planar flame configurations and is therefore radius independent: the instability is considered to be fully developed, and the efficiency function is activated right from the start ($E_{\text{TDS}} > 1 \forall r_f \geq 0$), which is conceptually inconsistent with the spherically propagating flames as observed in Fig. 2.1.

We adopted a new paradigm [2, 31] during the PhD of **J. J. Hok**, called **TD-S-TF**, which bypasses these two limitations:

(S1) S-TF: the **S-TF** part of the model solves the limitations of **TF-adapt** by seeking the Lewis number correction that is able to guarantee the correct flame consumption speed of flames subjected to a stretch target \mathbb{K}_t located beyond the weak stretch limit. In spirit, the **S-TF** model can be understood as a shooting correction that uses the Lewis number, which controls the slope at the origin of the $s_c - \mathbb{K}$ curve, to match the consumption speed at the target stretch. The problem is therefore formulated as an optimisation problem, in which $\forall k \in \llbracket 1, N_{\text{spec}} \rrbracket$:

$$\left\{ \begin{array}{l} D_{\text{th}} \mapsto F_{\text{th}} D_{\text{th}} \\ D_k \mapsto F_{\text{sp}} D_k \\ \dot{\omega}_k \mapsto \frac{\dot{\omega}_k}{F_{\text{r}}} \end{array} \right. \quad \text{with} \quad \left\{ \begin{array}{l} F_{\text{th}} = F \\ F_{\text{r}} = \frac{1}{F} \left(\frac{F}{F_{\text{sp}}} \right)^{2\gamma} \\ F_{\text{sp}} \end{array} \right. \quad \begin{array}{l} \implies \delta_{\text{L}}^0 \mapsto F \delta_{\text{L}}^0 \\ \implies s_c \xrightarrow{\mathbb{K} \rightarrow 0} s_{\text{L}}^0 \\ \text{s.t.} \quad \min_{F_{\text{sp}}} \frac{|s_c(F) - s_c(F=1)|}{s_c(F=1)} \Big|_{\mathbb{K}=\mathbb{K}_t} \end{array} \quad (2.14)$$

where γ controls the laminar flame speed dependance on the deficient reactant diffusivity, $s_{\text{L}}^0 \propto D_{\text{F}}^{\gamma}$. F/F_{sp} corresponds to the correction of the Lewis number: $\text{Le}_k \mapsto F/F_{\text{sp}} \text{Le}_k$. Written this way, the **S-TF** model generalizes the formulation of the TF transform and conserves its constitutive behavior (conserving s_{L}^0 and thickening the flame). Both TF and TF-adapt appear as particular cases of the **S-TF** model. The capacity of the **S-TF** model to drastically reduce the limitations of TF-adapt is highlighted in Fig. 2.6(a) in a 1D counterflow premixed flames configuration. The **S-TF** results remain close to the FRS simulations even for large values of F , which is not the case for TF-adapt and of course even less for TF. The application of **S-TF** on spherically propagating cylindrical flames, in Fig. 2.6(b), confirms its capacity to capture the effect of stretch on flames, whatever the nature of the stretch itself (curvature or strain).

(S2) TD-S-TF: As already discussed in Section 2.1.2.1, the efficiency function proposed by Goulier [1] to model the effective contribution of the cellular instability to flame acceleration is used instead of the Berger correlation since it intrinsically accounts for the transient nature of the self-propagating flames. It depends on two parameters: the flame radius r_f , which can be computed on the fly in the simulation; and the effective Lewis number Le_{eff} . Coupling the efficiency of Goulier with the **S-TF** is also consistent

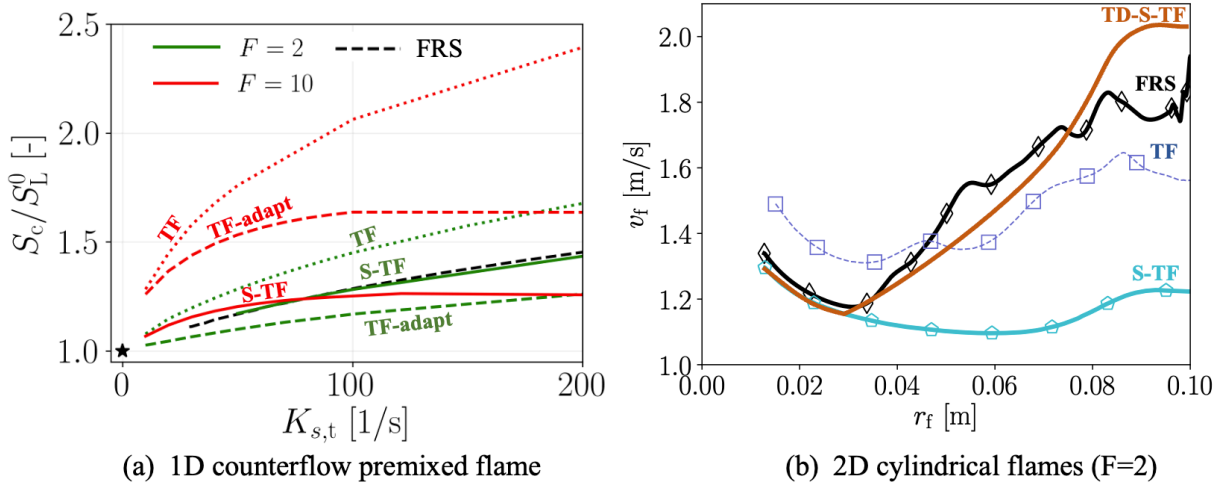


Figure 2.6: (a) Illustration of the performance of the S-TF model using 1D counterflow premixed flames for $F = 2, 10$. (b) Illustration of the TD-S-TF strategy using cylindrical self-propagating flames for $F = 2$. The case corresponds to $\phi = 0.356$, $T_u = 296\text{ K}$ and $P = 1\text{ atm}$. Adapted from [2].

with the definition of the efficiency proposed by Goulier, which is obtained with respect to the ideally stable (stretch sensitive) flame counterpart, an ideal case reproduced by the $S - TF$ as shown in Fig. 2.6(b). Compared to the TF approach, the **TD-S-TF** provides an accurate prediction of the dynamics of spherically propagation very-lean H₂/air flames: (i) during both the stable and unstable phases of propagation as shown in Fig. 2.6(b); (ii) with a drastically enhanced mesh independence as highlighted in Fig. 2.7(a), a result that can be largely attributed to the **S-TF** correction of the problem of amplification of stretch sensitivity by the thickening procedure. Finally, the application of the **TD-S-TF** to the finger flame case, where the saturation of the Goulier efficiency discussed in Section 2.1.2.2(M2) is retained, showcases the excellent performance of the **TD-S-TF** in confined configurations as well (see Fig. 2.7(b)) and paves the way for its use in the prediction of very-lean H₂/air deflagration problems.

2.1.5 First attempts at the turbulent stage of flame propagation and current limitations

The **TD-S-TF** model has shown its capacity to accurately reproduce the propagation of very-lean H₂/air flames when the flow is essentially laminar. The question arises as to how do we model the turbulent stage eventually reached in deflagrations, or more specifically: how do we model the interaction between turbulence and intrinsic flame instabilities in LES? This is still an open question in the combustion community, one that is still at the center of several PhD theses at CERFACS. We will discuss here only the first attempts that we tried with **F. Meziat** [27] and **J. J. Hok** [32], essentially driven by pragmatism. The strategy assumed an independence between thermo-diffusive and turbulence effects. This assumption corresponds to an extreme case where multiple contributions to flame acceleration are assumed to be uncorrelated [33, 34]. The **TD-S-TF**

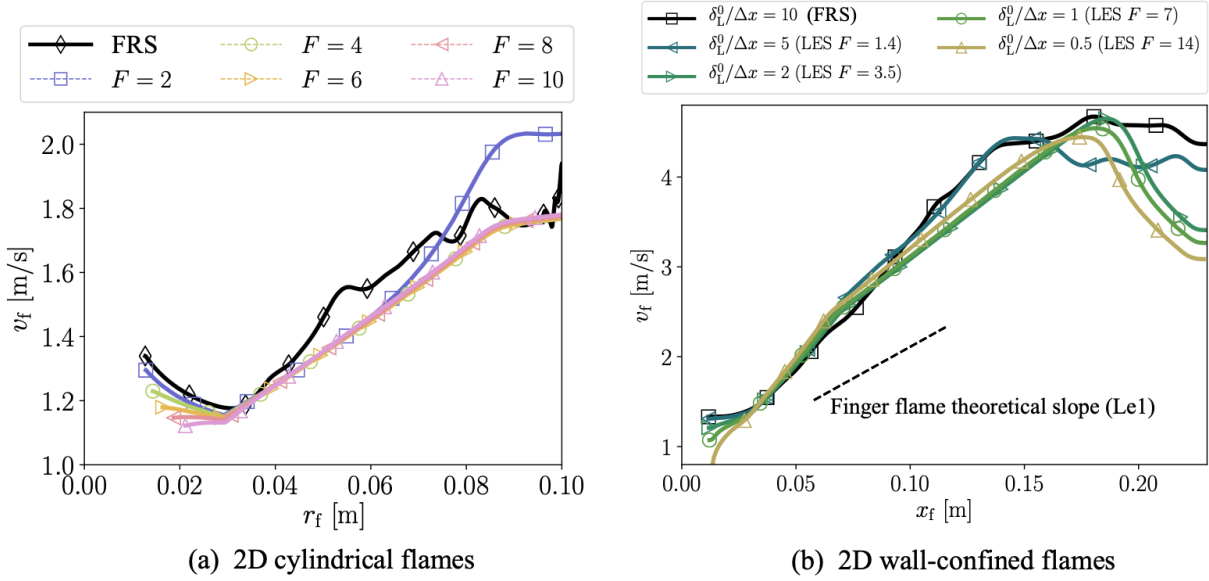


Figure 2.7: Performance of the TD-S-TF modeling strategy on the problem of self-propagation of very lean H_2/air cylindrical flames (a) and wall-confined 2D flames (b): illustration with $\phi = 0.356$, $T_u = 296 \text{ K}$ and $P = 1 \text{ atm}$. In the TF simulations, the thickened flame front is always resolved on 7 mesh cells, *i.e.* $F\delta_L^0 = 7\Delta x$. Adapted from [2].

model is therefore used with the Goulier efficiency function E_{lam} for its accurate prediction of flame dynamics in the laminar regime and a classical Charlette formulation \mathcal{E} [35], suited for weakly stretch-sensitive hydrocarbon flames, is used to account for turbulent wrinkling. Under the assumption of independence between thermo-diffusive and turbulence effects, the coupling between both effects in LES amounts to simply using an overall efficiency $E = E_{\text{TDS}}\mathcal{E}$ during the whole flame propagation. This strategy was tested in the ENACCEF-2 configuration, a 7.65 m long tube equipped with 9 annular obstacles, with a blockage ratio of 63%, placed in the first 2.5 m section of the tube, thereby providing a strong flame acceleration. Two very-lean H_2/air mixtures were considered ($\phi = 0.356$ and $\phi = 0.42$) to test the capacity of this simple strategy to account for progressively leaner (and more unstable) flames. Fig. 2.8 shows an overall good agreement between the experimental data and the prediction of the LES for the case $\phi = 0.42$, both in terms of the early stages of flame acceleration before the first obstacle and in the turbulent high-speed regime towards the end of the obstructed region. This is not the case for the most unstable case $\phi = 0.356$ where the simple TD-S-TF – \mathcal{E} strategy fails to accurately capture the strong flame acceleration observed in the experiments.

These results echo recent DNS observations of different groups [36, 37], which suggest a more complex coupling between intrinsic instabilities and turbulence at moderate to high turbulence levels. Further efforts are therefore needed to propose a reliable modeling strategy for the propagation of very-lean H_2/air fast deflagration waves. This is the subject of ongoing research at CERFACS and many other groups as well. More promising results were obtained recently in the PhD of **F. Meziat**.

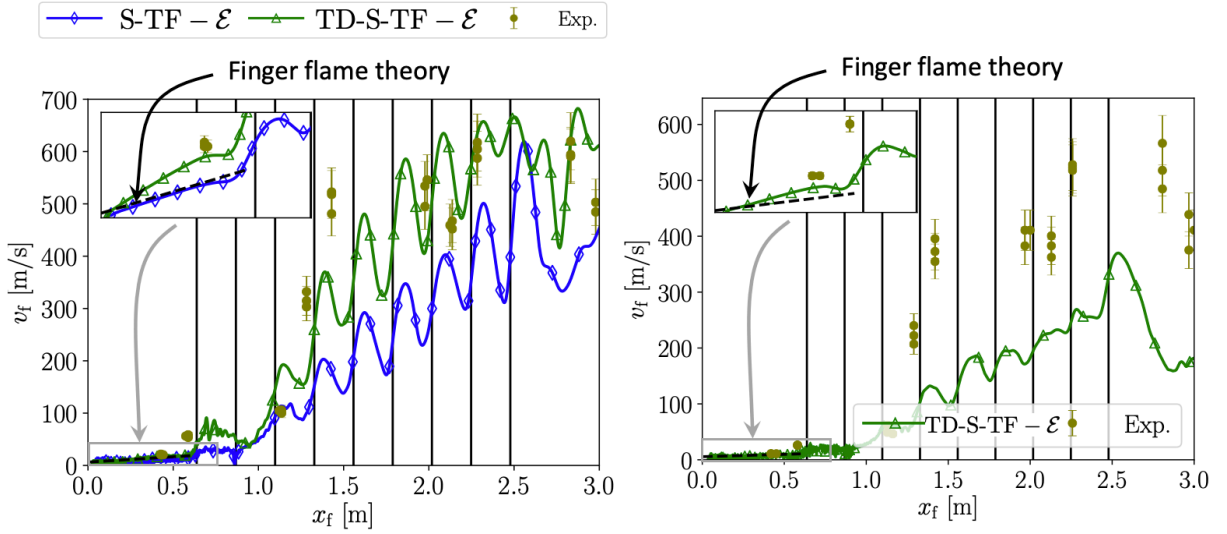


Figure 2.8: Performance of a simple strategy $\text{TD-S-TF} - \mathcal{E}$ for the coupling between thermo-diffusive and turbulent effects: ENACCEF-2 test case (a) $\phi = 0.42$; (b) $\phi = 0.356$. In, $\text{TD-S-TF} - \mathcal{E}$, the overall efficiency function reads $E = E_{\text{TDS}}\mathcal{E}$, where E_{TDS} accounts for the contribution of the cellular instability to flame acceleration following Goullier et al. [1] and \mathcal{E} models turbulent wrinkling in weakly stretch sensitive flames, following Charlette formulation [35]. In the obstructed region, $\Delta x = 4 \text{ mm}$ corresponding to $F \approx 50$ ($F \approx 30$) for $\phi = 0.42$ and $\phi = 0.356$ respectively. Details of the numerical setup can be found in [32].

2.2 Impact of stratification on flame acceleration

2.2.1 Context and funding

The work presented in this section was supported by two funding sources. AIRBUS, under the project STOHYC, formulated several problems linked to the safety scenarios associated to hydrogen aircraft applications. These problems can be grouped into two categories: explosions and jet-flames. We will only discuss the former in this manuscript. More specifically, the idea within STOHYC is to concentrate on realistic explosion scenarios where the initial conditions before ignition are characterized by hydrogen stratification. The question arises as to: (i) how stratification impacts the explosion; and (ii) how do we accurately predict that in LES. Section 2.2.3 delves into this issue.

A similar problem is encountered during the ignition of a hydrogen plume above a liquid hydrogen spill/pool. The evaporation of the liquid hydrogen pool/spill leads to a formation of highly stratified mixture (both in mixture and temperature). A collaboration with IMFT, around the PEPR- H_2 project ESKHYMO, delved into the impact of this stratification on the early stage of flame acceleration. This is the subject of Section 2.2.2.

2.2.2 Impact of axial stratification on the early stages of flame acceleration: controlling parameters

To understand the parameters controlling flame acceleration in stratified mixtures, we opted for the simplest test case allowing to perform DNS and theoretical derivations to extract the controlling parameters in Missey et al. [38]. The test case is illustrated in Fig. 2.9 where an axial stratification is imposed before ignition in a 2D finger flame configuration (see Section 2.1.2.2). The stratification of fresh gases is imposed by a linear temperature profile with a constant gradient of $\nabla T = \pm 1200 \text{ K/m}$, corresponding to $\Delta T = \pm 24 \text{ K}$ at $x = R$. The equivalence ratio varies with fresh gases temperature according to the perfect mixing relation $\phi = p_m(T)$ observed experimentally above liquid hydrogen pools. In total, 5 cases are considered and correspond to: (A) reference homogeneous case at $\phi = 1$ and $T = 220 \text{ K}$; (A-*) mixture stratification with mixture A at the ignition point $x = 0$ and a stratification towards richer (resp. leaner) H_2/air mixtures mimicking flame propagation towards (resp. away from) the liquid pool; (B and C) stratification test cases with ignition in mixtures far away and very close to the liquid pool in B and C respectively - and flame propagation towards and far way from the liquid pool. An illustration of the variation of the flame parameter σ_{sL} fro each test case is shown in Fig. 2.9(c).

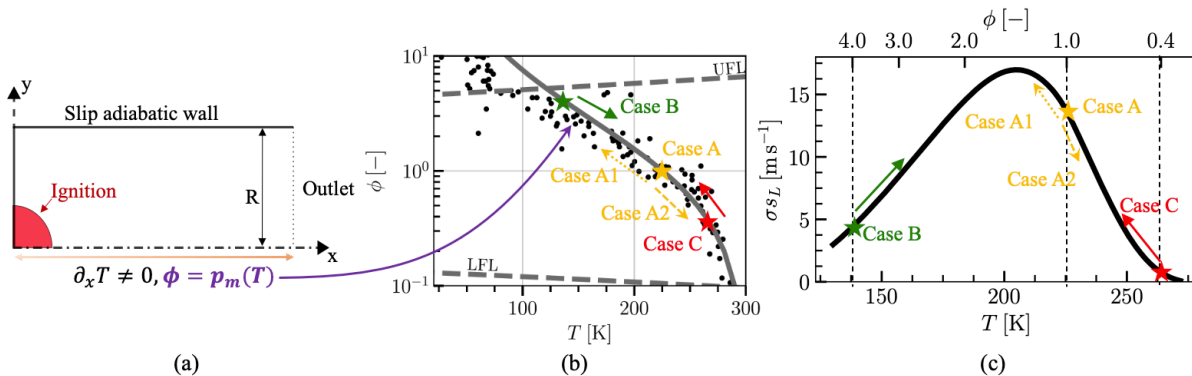


Figure 2.9: Illustration of the axially-stratified finger flame test case. (a) Combined temperature ($\partial_x T \neq 0$) and mixture ($\phi = p_m(T)$) stratification in a finger flame setup. (b) Temperature and mixture stratification above a liquid hydrogen pool and validity of the perfect mixing relation $\phi = p_m(T)$. (c) Variation of the flame property σ_{sL} along the perfect mixing line. Adapted from [38].

The results of Flame Resolved Simulations are displayed in Fig. 2.10 and show that stratification can have either an enhancing or mitigating effect on flame acceleration depending on the direction of stratification: stratification towards more (less resp.) reactive mixtures as in A-1 (A-2 resp.) enhances (mitigates resp.) the finger flame acceleration (reference case A). In all cases, a quasi-linear relation between the flame speed and flame position is observed, a footprint of the finger flame acceleration mechanism, except for case C for which the mixture is very-lean at ignition and is impacted by the onset of flame instabilities (cellular structure observed in Fig. 2.10(a)) thereby drastically enhancing flame acceleration for $\xi_{tip} \geq 1$ in Fig. 2.10(c), in accordance with the observations of Section 2.1.2.2.

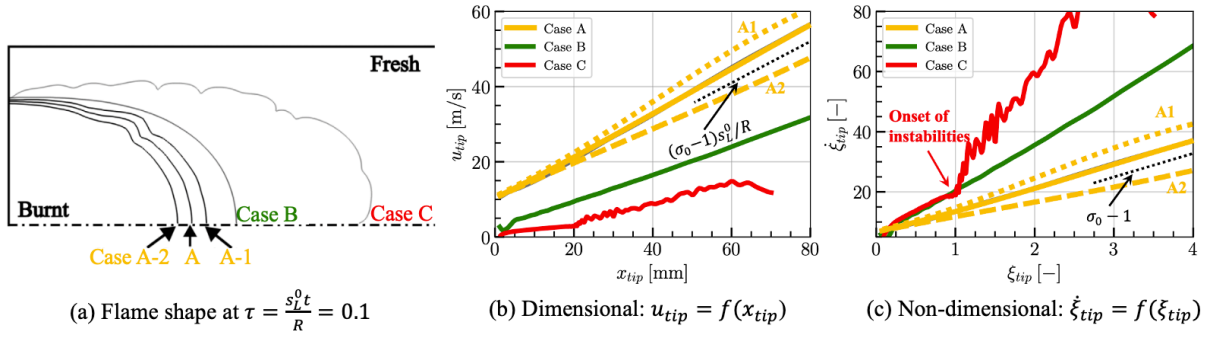


Figure 2.10: Flame Resolved Simulations (FRS) of the axially-stratified finger flame problem. (a) Flame isocontour ($T = 350 \text{ K}$) at iso-reduced time $\tau \equiv s_L^0 t / R$; (b) Flame tip propagation speed u_{tip} vs flame tip position x_{tip} in dimensional form. (c) Non-dimensional form of (b) where $\xi_{tip} = u_{tip} / s_L^0$ and $\zeta_{tip} = x_{tip} / R$. s_L^0 corresponds to the mixture state at the origin $x = 0$. R is the tube radius. Adapted from [38].

To highlight which parameters control the impact of stratification on FA in the finger flame test case, it is possible to extend the finger flame theory [16] to take into account stratification, which reads for the 2D case (details can be found in [38]):

$$\text{(SFT)} \quad \frac{dx_{tip}}{dt} = \sigma_0 s_L^0 \mathbf{f}_{\sigma_{s_L}}(x_{tip}) + \frac{(\sigma_0 - 1) s_L^0}{R} \mathbf{f}_{\rho_b}(x_{tip}) x_{tip} \quad (2.15)$$

$$\text{with: } \mathbf{f}_{\vartheta}(x_{tip}) \equiv \frac{\vartheta(x_{tip})}{\vartheta(x_{tip} = 0)} \text{ for } \vartheta = \{\sigma_{s_L}, \rho_b\} \quad (2.16)$$

$\mathbf{f}_{\sigma_{s_L}}$ and \mathbf{f}_{ρ_b} are stratification parameters which account for the impact of stratification on the planar flame speed σ_{s_L} and burnt gases density ρ_b . In the homogeneous case, *i.e.* when the mixture is equal everywhere to its state at the ignition point, $\mathbf{f}_{\sigma_{s_L}}$ and \mathbf{f}_{ρ_b} are both unity and the classical finger flame equation [16] is retrieved. Eq. (2.15) is a 1st-order ode with x_{tip} -dependent parameters $\mathbf{f}_{\vartheta}(x_{tip})$ and cannot be solved analytically in the general case. Eq. (2.15) also requires a knowledge about the unburnt gases properties at the flame tip position. A simple closure is to assume a frozen stratification, where the mixture composition and temperature are not impacted by flame propagation and are equal to their value imposed before ignition:

$$\text{(SFT)}_{fr} : \quad \text{Eq. (2.15) with } \mathbf{f}_{\vartheta}(x_{tip}) = \mathbf{f}_{\vartheta}(x_{tip})|_{t=0} \quad (2.17)$$

As shown in Fig 2.11(a), the Stratified Finger flame theory under frozen stratification $(\text{SFT})_{fr}$ is unable to correctly reproduce the flame acceleration observed in cases A-1 and A-2. This is because the flame acts as a permeable piston that sets fresh gases into motion, thereby influencing the stratification that the flame actually sees in front of it during its propagation. In other words, stratification evolves in time. To highlight the importance of this effect, the stratification parameters \mathbf{f}_{ϑ} are extracted from the FRS simulation $\mathbf{f}_{\vartheta, \text{eff}}$ and compared to their frozen counterpart $\mathbf{f}_{\vartheta, \text{fr}}$ in Fig. 2.11(b). Two main conclusions can be drawn from this figure, valid for both cases A-1 and A-2:

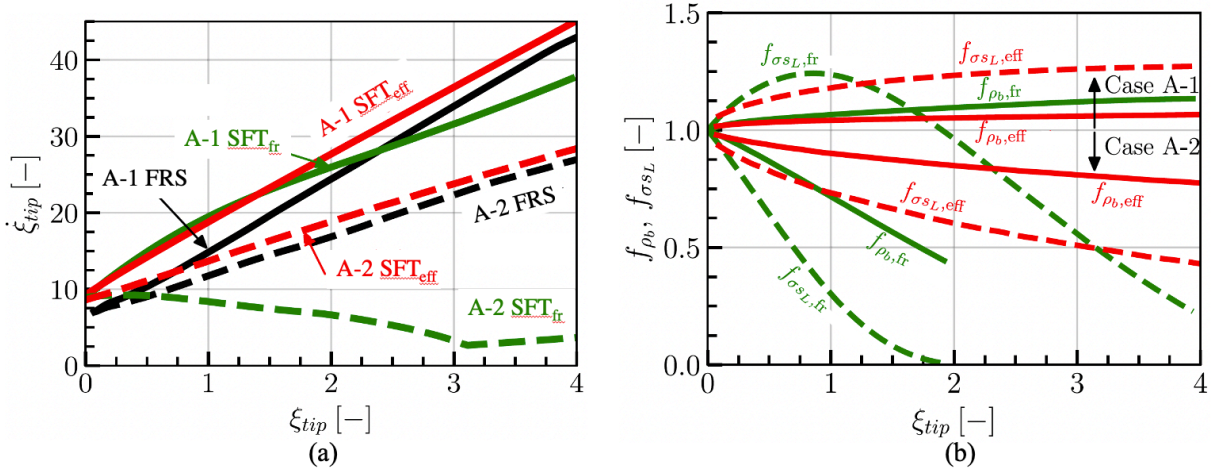


Figure 2.11: (a) Evolution of the flame speed $\dot{\xi}_{tip}$ with flame position ξ_{tip} for the stratified cases A-1 and A-2. (b) Evolution of the stratification parameters $f_{\sigma_{SL}}$ and f_{ρ_b} with flame position. SFT_{eff} and SFT_{fr} correspond to flame resolved simulations under effective and frozen stratification respectively. SFT refers to Stratified Finger flame Theory Eq. (2.15)-(2.16). Indices $_{fr}$ and $_{eff}$ refer to the state of the stratification either frozen (initial stratification) or effective (evolving in time and extracted from the FRS simulations). Adapted from [38].

- the main driving parameter of the impact of stratification of flame acceleration is $f_{\sigma_{SL}}$, an indicator of the evolution of the mixture reactivity with flame position. $f_{\sigma_{SL}}$ shows the largest deviations from unity, hence has the strongest impact on Eq. (2.15) either as an enhancer (A-1) or mitigator (A-2) of flame acceleration. The impact of stratification on burnt gases density, which controls the flow in the burnt gases and characterized by f_{ρ_b} plays only a supporting role.
- flame propagation acts as a damper for the stratification: $|\mathbf{f}_{\vartheta,eff} - 1| \leq |\mathbf{f}_{\vartheta,fr} - 1|$. The flame pushes the gases ahead of it and the impact of a stratified layer is only felt later during flame propagation. This delay in time reduces the slope of the stratification curves $\mathbf{f}_{\vartheta}(x_{tip})$.

Fig 2.11(a) further shows that taking into account the time evolution of the stratification parameters drastically improves the predictive capability of the STF equation (2.15). This is done by imposing the stratification extracted from the FRS simulations directly into Eq (2.15). The highly stretch-sensitive flames in cases B and C remains out of the scope of the simple finger-flame theory, which does not account for neither stretch effects of flame surface production by flame instabilities. This part is the subject of ongoing work.

2.2.3 Impact of stratification on flame acceleration in obstructed channels: a LES investigation.

In the PhD thesis of **E. Matas Mur**, we investigated the impact of stratification on larger-scale deflagrations. The test case corresponds to the Gravent explosion channel [40].

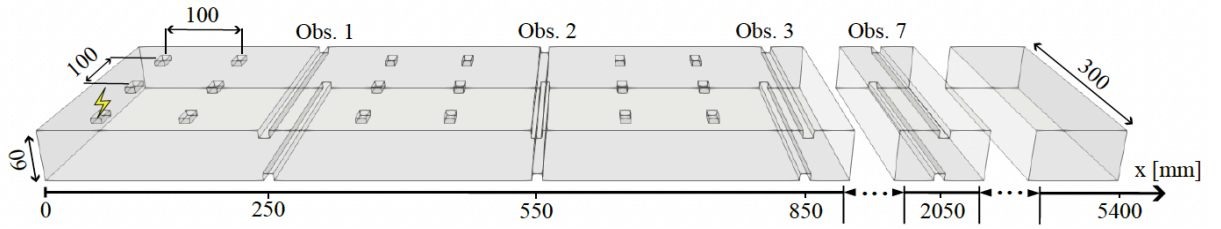


Figure 2.12: Schematic of the BR30hS300 configuration of the GraVent channel. The dimensions of the channel are $5400 \times 300 \times 60 \text{ mm}^3$. It is equipped with 7 rows of rectangular obstacles of dimensions $12 \times 9 \text{ mm}^2$ on the top and bottom plates. The first obstacle is located 250 mm away from the ignition plate (marked with a lightning sign) and the distance between obstacles is $S = 300 \text{ mm}$. 162 injectors are uniformly distributed over the entire top wall in 3 rows and 54 columns. The separation between injectors is 100 mm in the axis of the channel and in the transverse axis. The dimensions of the injectors are the following: $12 \times 26 \times 7 \text{ mm}^3$. Adapted from [39].

Fig. 2.12 shows its important features: 7 rectangular obstacles are placed in the path of stratified H_2 /air deflagration waves with a blockage ratio of 30%. H_2 is injected through 162 injectors located on the top plate (small boxes observed in Fig. 2.12). Stratified mixtures can be created by playing with the delay between injection and ignition. For large delay time, typically 60 s , homogeneous conditions are retrieved. However, for much smaller delay time, a stratification profile can be obtained in the explosion channel. An extreme case corresponding to a delay of 3 s is shown in Fig. 2.13 for three global H_2 volume fractions, *i.e.* $\overline{X_{\text{H}_2}} = \{17.5, 25, 30\} \%$. The profiles observed for the three cases are diffusion driven.

The three conditions shown in Fig. 2.13 are imposed as initial conditions for LES simulations and are denoted $S17.5$, $S25$ and $S30$, where S indicates stratification and the following numbers correspond to the average volume fraction considered $\overline{X_{\text{H}_2}}$. Additionally, their homogeneous counterpart were also simulated and will be denoted by $H17.5$, $H25$ and $H30$.

2.2.3.1 Brief description of the numerical setup

General Approach: The GraVent case presents a significant challenge for numerical simulations due to its relatively large volume of approximately 100 liters, making Direct Numerical Simulation (DNS) impractical at this scale. To overcome the scaling aspect, a LES approach is adopted using AVBP. Convective terms are resolved using a two-step Taylor-Galerkin finite element scheme [41], achieving third-order accuracy in both time and space, while diffusive terms are discretized with a finite element method. To handle pressure discontinuities corresponding to shocks, a selective filter is applied over the pressure fields, followed by a second-order artificial viscosity term to smooth under-resolved gradients. To avoid influencing the onset of the initial kernel by heat losses, an adiabatic slip wall is used for the ignition plate. The rest of the channel walls are modeled using an iso-thermal law of the wall with $T_{\text{wall}} = 300 \text{ K}$. The mesh is characterized by a global resolution of

$\Delta x = 2 \text{ mm}$ in the obstructed region, except for a local refinement around each obstacle of $\Delta x = 1.2 \text{ mm}$ to capture flow contraction effects, and a coarser resolution past the last obstacle (not the region of interest in this study). All the details of the mesh can be found in [39].

Chemistry: Contrary to the LES shown in the first section of this chapter, we switched in these first studies involving stratification to the San Diego detailed chemical scheme [42] because it straightforwardly accounts for non-uniform mixture conditions.

Subgrid scale modeling: To accurately account for subgrid scale (SGS) turbulence, the WALE model [43] is employed. To resolve the flame structure, the dynamic flame thickening (DTF-LES) method is utilized, ensuring at least five cells within the flame front, coupled with Charlette’s efficiency model [35] to account for the unresolved wrinkling induced by turbulence at the subgrid-scale. Furthermore, a simple strategy is adopted to model the lean-part of the profiles shown in Fig. 2.13. Effects related to thermo-diffusive instabilities are modeled using an additional efficiency function based on Berger’s correlation [44], which accounts for temperature, equivalence ratio, and pressure. It is assumed that the effects addressed by the two models do not interfere with each other, similarly to the pragmatic approach used in Section 2.1.5.

This modeling strategy corresponds to a first attempt at reproducing stratification effects on large-scale deflagrations and are by no means a formulation of a well-posed paradigm. Further discussion is provided at the end of this section.

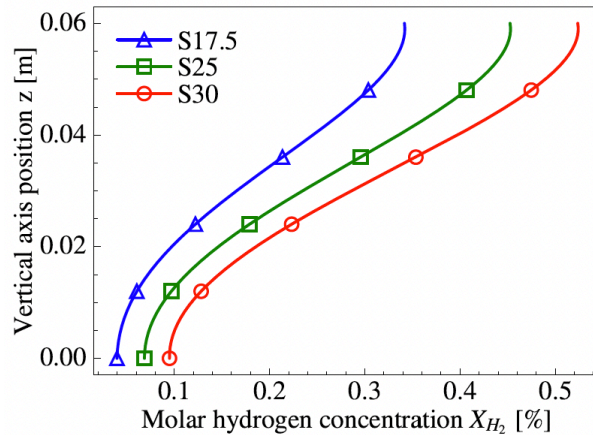


Figure 2.13: Stratification profiles in the three cases considered.

2.2.3.2 LES validation

Fig. 2.14 shows compares the flame speed evolution predicted by LES with the experimental data for all six cases considered (homogeneous and stratified). The LES correctly captures the trends observed in the experiments, namely: (1) the strong flame acceleration provided

by the obstacles in all cases, leading to supersonic flame speeds relative to the laboratory frame; (2) stratification does not necessarily promote flame acceleration and its impact depends on the global H_2 volume fraction \overline{X}_{H_2} ; (3) for globally lean mixtures, *i.e.* $\overline{X}_{H_2} < 20\%$, stratification has a strong promoting impact on flame acceleration as observed in Fig. 2.14(a), however no or mild inhibiting effect on FA is observed for globally richer mixtures, *i.e.* $\overline{X}_{H_2} \geq 25\%$.

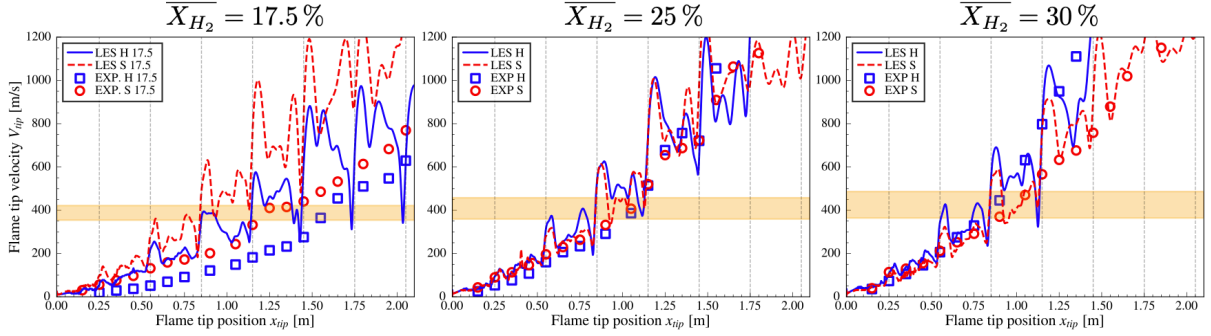


Figure 2.14: Flame tip velocity in a fixed reference frame as a function of the flame front position across the channel at different mean molar hydrogen concentrations: (a) 17.5 %, (b) 25%, (c) 30%. For each case, *S* and *H* denote stratified and homogeneous initial conditions. The orange shaded area showcases the ranges of speed of sound velocities found on the unburnt stratified mixture and gray vertical lines illustrate the presence of the obstacles. Adapted from [39].

The LES also confirms the results of Section 2.2.2 in that flame propagation has also a strong impact on the stratification profiles as highlighted in Fig. 2.15. One can clearly see: (i) the strong stratification-induced elongation of the flame due to the strong gradient of burning velocity along the flame front, (ii) but also the evolution of the stratification ahead of the flame, where enhanced turbulent mixing causes a departure from the initial stratification. This is an important feature that must be kept in mind for modeling purposes: the initial stratification can provide indications on potential FA trends but can not be used to characterize the whole flame propagation dynamics.

2.2.3.3 Delineating flame surface and burning-velocity gradient effects in stratified deflagrations.

The LES results correctly reproduce the trends observed experimentally on the impact of stratification on flame propagation. In the work of **E. Matas Mur** we used them to delineate flame surface and burning-velocity gradient effects in stratified deflagrations.

- We focus first on flame surface, which we define locally by:

$$A_{tot}^{\phi_i} = \iiint_{V^{\phi_i}} \Xi \cdot \Xi_{TD} \cdot |\nabla c| \, dv \quad \text{with} \quad c = \frac{Y_{H_2}(\vec{x}) - Y_{H_2}^b(\phi, T, P)}{Y_{H_2}^u(\phi, T, P) - Y_{H_2}^b(\phi, T, P)} \quad (2.18)$$

$|\nabla c|$ represents the Flame Surface Density (FSD), and V^{ϕ_i} stands for the volume

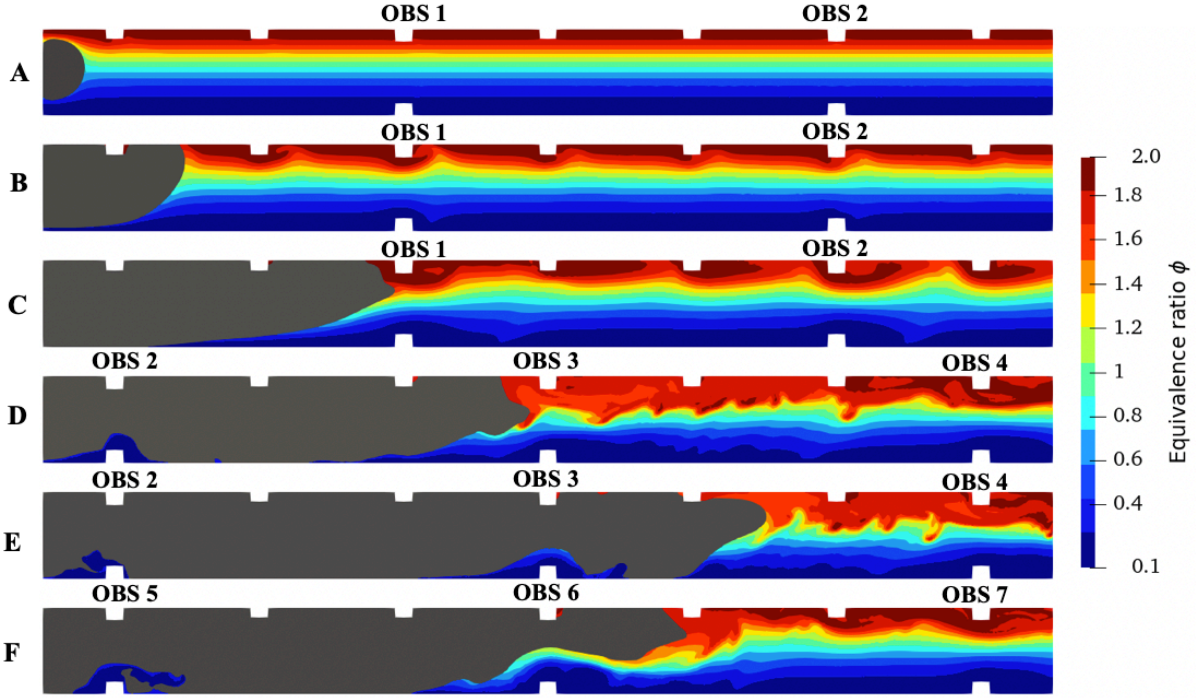


Figure 2.15: Evolution of the stratification in the unburnt gases with flame propagation: 2D Fields of equivalence ratio. The case corresponds to $\overline{X_{H_2}} = 25\%$. Adapted from [39].

where $|\phi - \phi_i| < \Delta\phi$. Ξ and Ξ_{TD} correspond to the contribution of the subgrid-scale turbulent wrinkling and flame instabilities on flame surface production. Fig. 2.16 shows PDF of normalized flame surface A_{tot}^ϕ (blue solid line) as a function of equivalence ratio ϕ for the three stratified cases at several instants indicated in Fig. 2.15. As suggested in Fig. 2.15, the majority of the flame surface is located in the lean regions for all cases because of the strong stratification-induced elongation of the flame. Furthermore, Fig. 2.17 displays the evolution of the global flame surface ($\int_\phi A_{tot}^\phi d\phi$) with the flame position and confirms that the stratification always leads to a drastic increase in flame surface. This result is of crucial importance: **the strong flame elongation observed in stratified deflagrations does not necessarily promote flame acceleration**. Even more, for the case $\overline{X_{H_2}} = 30\%$, stratification seems to mitigate flame acceleration, as observed in Fig. 2.14, despite the strong increase in flame surface relative to the homogeneous case observed in Fig. 2.17.

- The non-monotonic impact of stratification with respect to $\overline{X_{H_2}}$ observed in Fig. 2.14 can be explained by weighing local flame surface elements with their associated turbulent burning velocity ($s_L \cdot \Xi_{turb} \cdot \Xi_{TD}$):

$$S_{eq}^{\phi_i} = \frac{\iiint_{V^{\phi_i}} \sigma s_L \cdot \Xi_{turb} \cdot \Xi_{TD} \cdot |\nabla c| dV}{l \times H} \quad (2.19)$$

$\sigma = \rho_u/\rho_b$ is used by analogy with the effective flame displacement speed criterion introduced in [45]. Fig. 2.16 shows the PDF of S_{eq} as a function of equivalence ratio ϕ for the three stratified cases Fig. 2.15. It clearly highlights an important

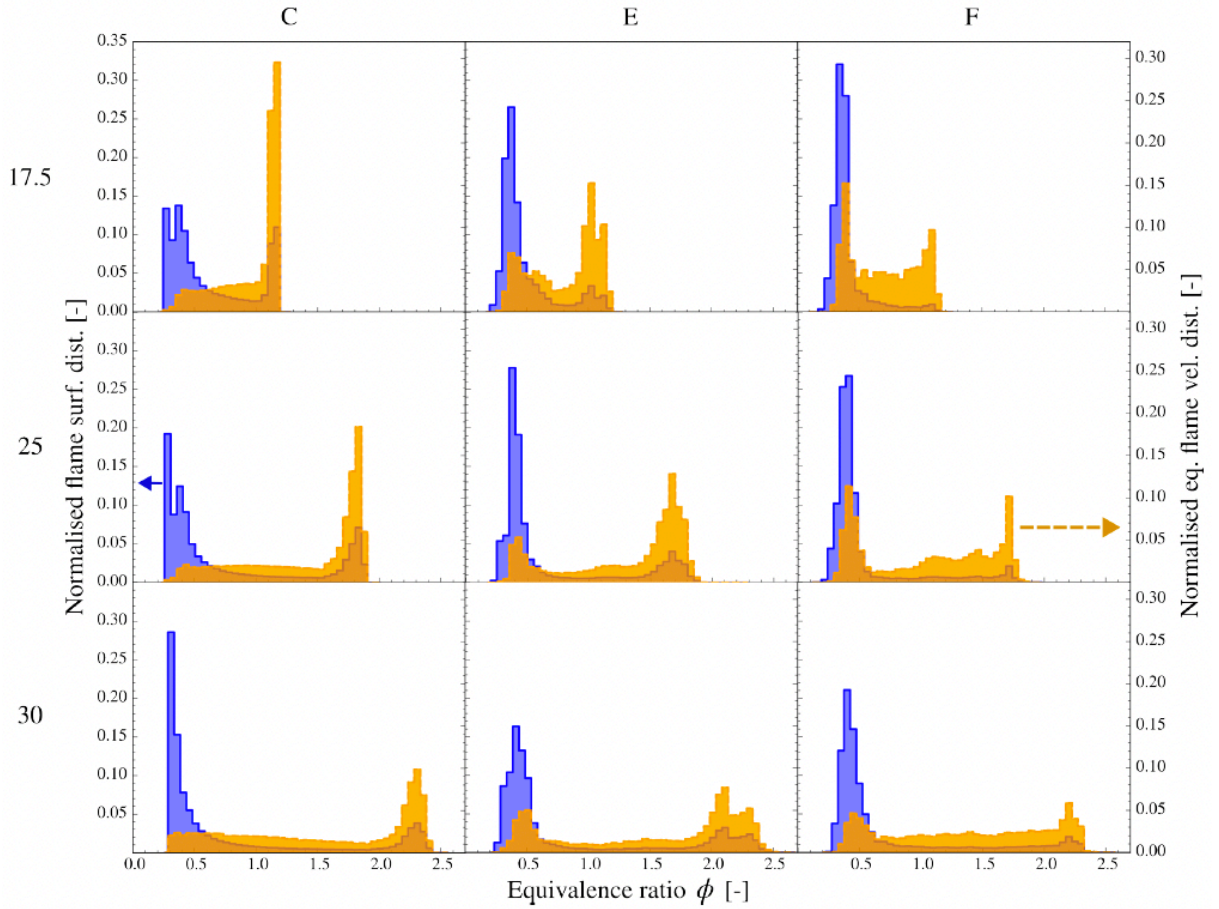


Figure 2.16: PDF of normalized total flame surface A_{tot} (blue solid line) and equivalent flame speed S_{eq} (orange dashed lines) as a function of equivalence ratio ϕ for S17.5, S25 and S30 at instants C, E, F indicated in Fig. 2.15. Adapted from [39].

feature of stratified H_2 /air deflagrations: **while a large part of the flame surface is contained in the lean region close to the flame skirt, due to flame elongation, its contribution to flame acceleration remains relatively small due to the low flame speeds encountered in very lean flames, hence the main contribution to the global burning velocity comes from the richer side, although the contribution of the lean side tends to increase in time.** This statement is of course strongly linked to the gradient of fundamental flame speed along the flame, and equivalently to the curve $s_L = f(\phi)$. Therefore, this conclusion will not necessarily hold for other fuels where lower gradients of fundamental flame speed may be found and a more pronounced contribution of the lean side to S_{eq} may be expected. Fig. 2.17(right) shows the evolution of the overall equivalent flame speed $S_{eq} = \int_{\phi} S_{eq}^{\phi} d\phi$ with flame position for all cases considered. It allows to explain the experimental observations: (1) Stratification induces a large increase in S_{eq} in the globally lean case ($\overline{X_{H_2}} = 17.5\%$) because of the aforementioned favorable flame surface increase and the contribution of richer flames, more reactive than their homogeneous counterpart; (2) for the two globally richer cases, $\overline{X_{H_2}} \geq 25\%$, the

fundamental flame speed at $X_{H_2} = \overline{X_{H_2}}$ is already high enough so that no more gain can be observed by the contribution of the richer side and the lean part mitigates the effect of flame elongation.

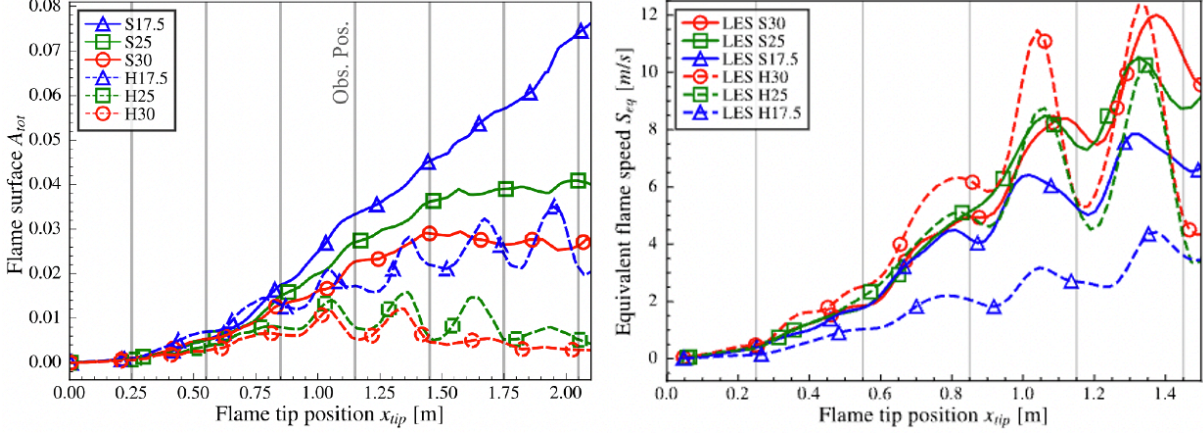


Figure 2.17: Evolution of the total flame surface (left) and equivalence flame speed (right) with the flame position. The gray vertical lines illustrate obstacle positions. Adapted from [39].

The analysis provided in Fig. 2.17(right) is a transient and 3D equivalent to the criterion proposed by Boeck et al, [45]. He derived a 0D approach based on the initial stratification profiles, which involves calculating the mean flame displacement speed $(\sigma_{sL})_{eff}$ along the vertical axis of the channel. This approach is equivalent to assuming a planar vertical flame front.

$$\sigma_{sL_{eff}} = \frac{1}{H} \int_H \sigma_{sL} dz \quad (2.20)$$

Fig. 2.18 compares $\sigma_{sL_{eff}}$ obtained with the homogeneous and initial stratified profiles for a range of global H_2 volume fraction. It allows to predict the promoting effect of stratification at globally lean conditions and the mitigating effect past a global concentration of 20 %. It however predicts a large mitigating effect at $\overline{X_{H_2}} = 30\%$, which is not observed in either the experiments or the LES. This is because of the Boeck criterion does not take into account the stratification-induced flame elongation and its associated flame surface production, which is not the case for S_{eq} , which combines both effects. The Boeck parameter is still a relevant and easy to compute characterizer of the potential effects of stratification on deflagrations.

2.2.4 S-TF and stratified explosions.

The results presented in Section 2.2.3 have been obtained with detailed chemistry. The goal now is to be able to reproduce these results using simple single-step chemistry more suitable for large-scale applications. Another limitation observed in Section 2.2.3 is regarding the over-prediction of flame acceleration observed in our LES compared to experiments for the overall lean case $\overline{X_{H_2}} = 17.5\%$. The focus is shifted now to the application of the

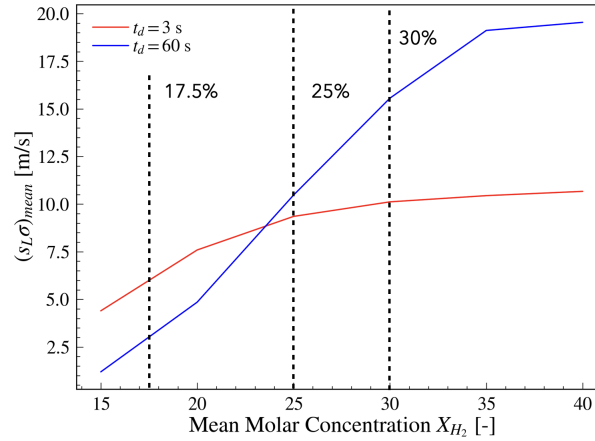


Figure 2.18: Evolution of the total flame surface (left) and equivalence flame speed (right) with the flame position. The gray vertical lines illustrate obstacle positions. Adapted from [39].

TD-S-TF strategy with single-step chemistry on the stratified Grauent cases to check the suitability of the approach for more realistic explosion scenarios. Intermediary results were already obtained and will be shared during the defense.

2.3 Deflagration to Detonation Transition (DDT)

As mentioned in the previous section, the deflagration can go through different regimes during flame acceleration, classified with respect to the flame propagation speed v_f : (i) slow deflagration, when $v_f < a_u$, with a_u the sound speed in the fresh gases; (ii) fast deflagrations, when $a_u < v_f < D_{CJ,deflag} = a_b$, with a_b the sound speed in the burnt gases; (iii) Quasi-detonations and detonations when $v_f > a_b$. The transition between the regimes (ii) and (iii) occurs «abruptly» and is referred to as the deflagration to Detonation Transition (DDT). The regime of fast deflagrations, characterized by the formation of compression waves and their coalescence/steepening into shock waves, often creates the necessary conditions to trigger DDT [46]. The accurate prediction of DDT therefore requires to take into account all the phenomena taking place from ignition to the time of DDT due to flame acceleration, which leads to computationally intensive simulations as shown in [47]. To circumvent this problem, the team of Matei Radulescu proposed in [48, 49] to bypass all the flame acceleration phase and mimic the conditions often observed right before DDT: the CJ-deflagration state, *i.e.* $v_f \approx D_{CJ,deflag} = a_b$. A schematic of the experimental setup is displayed in Fig. 2.19, where a pre-detonation channel allows to create a self-sustained detonation front which interacts with an obstacle with relatively high blockage ratio leading to detonation quenching. As shown in Fig. 2.19(bottom), a decoupling between the incident shock and the reaction wave behind it is observed when the detonation exits the obstructed layer and a decay of the reaction wave propagation speed towards the Chapman Jouguet deflagration speed is observed. This experimental setup has two advantages: (i) a well controlled fast flame conditions prior to DDT that can

be easily reproduced in numerical simulations; (ii) a detailed analysis of the mechanisms controlling DDT past the CJ deflagration state, both experimentally and numerically. In the work of Jaravel et al. [50], we used this ideal setup to delve into the potential modeling strategies for DDT, with a key parameter to reproduce: the run-up distance to DDT, *i.e.* the distance from the obstacle x_{DDT} at which DDT is observed.

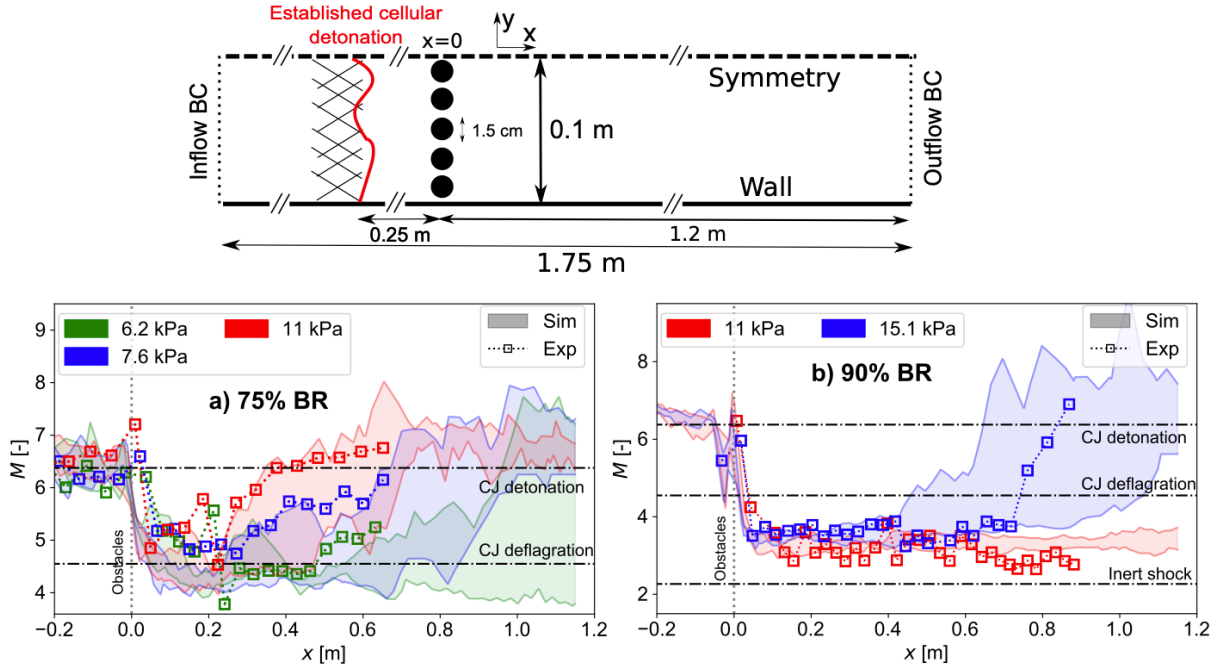


Figure 2.19: (Top) Schematic of the detonation quenching and re-initiation setup of the university of Ottawa [48, 49]. (Bottom) comparison between the experimental and numerical results for different values of initial pressure P_{init} and obstacle blockage ratio BR . $M \equiv v_r/a_u$ is the propagation Mach number of the self propagating reaction waves. Adapted from [50].

The mixture considered corresponds to a stoichiometric methane-oxygen mixture at an initial temperature of 300K. Both the initial pressure P_{init} and the obstacle blockage ratio BR serve as controlling parameters for the run-up distance x_{DDT} . To compare with the experimental data, we formed 2D DNS simulations in [50]. The results of Fig. 2.19(bottom) show that:

- Despite simplifying assumptions (one-step chemistry, two-dimensional flow), the DNS setup is able to capture the essential flow features observed experimentally as well as the impact of initial pressure and BR on the re-initiation propensity: capturing longer run-up distances and failed re-initiation for low P_{init} and high BR conditions.
- Ensemble simulations of five realizations are performed for each operating condition to address the stochastic nature of DDT, highlighting the significant variability of DDT location, see the simulation envelopes in Fig. 2.19(bottom).

We then used the DNS results to test whether it is possible to find reliable DDT indicators to use on-the-fly during the simulations for different modeling purposes: (i) automatically detect the transition between combustion regimes and switch between different sets of chemical parameters for flames, ignition and detonations when a unified set can not be found with simplified chemistry, in a manner similar to [51]; (ii) detect regions where resolution must be increased (ignition spots, ...); etc We opted for a Computational Singular Perturbation (CSP) based approach [52], relying on the analysis of the eigenvalues of the Jacobian of the chemical system, and is useful to characterize reactive mixture subject to events such as auto-ignition, flame and stabilization mechanism [53, 54]. Following [54, 55], the evolution of the source terms of the thermo-chemical system is governed by

$$\frac{D\omega}{Dt} = J_\omega(\omega + s), \quad (2.21)$$

where ω is the source term vector (of species and temperature), s is the diffusion contribution, and J_ω is the Jacobian of the chemical system. A chemical explosive mode (CEM) exists if J_ω has an unstable eigenvalue characterized by a positive real part λ_e . If multiple explosive modes are present, the CEM is identified as the mode with the largest λ_e , with corresponding left eigenvector b_e . By projection of Eq. 2.21 in the direction of the CEM, the following relation is obtained [54]

$$\frac{D\phi_\omega}{Dt} = \lambda_e\phi_\omega + \lambda_e\phi_s + \frac{Db_e}{Dt} \cdot \omega, \quad (2.22)$$

where

$$\phi_\omega = b_e \cdot \omega, \quad \phi_s = b_e \cdot s. \quad (2.23)$$

Xu *et al.* [54] introduced the local combustion mode indicator α as

$$\alpha = \phi_s / \phi_\omega. \quad (2.24)$$

This ratio compares the relative alignment of chemistry and diffusion source terms contribution with the chemical explosive mode. In the current context, there are two extreme regimes of interest: the fast flame regime where the diffusion in the preheat zone promotes the ignition of the mixture ($\alpha \gg 1$), and the detonation regime characterized by the autoignition of the mixture ($|\alpha| \ll 1$). Spontaneous hotspot ignition events are also controlled by auto-ignition and expected to also exhibit $|\alpha| \ll 1$. Mixed propagation modes with intermediate α values are also possible, for which the auto-ignition process can strongly support the flame propagation. Fig. 2.20(left) shows that the CEM parameter $\alpha^* = \alpha(c = 0.05)$ taken at the progress variable $c = 0.05$ is an excellent indicator of the combustion regime where detonation and deflagration waves are correctly detected, failed DDT events are also capture (case $P_{init} = 6.2kPa$) and intermediate values of α^* can serve to detect DDT regions.

The detailed analysis of the re-initiation mechanism in Fig. 2.20(right) shows that the transverse waves play a critical role in the detonation formation. Regions of high reactivity are typically formed behind Mach stems. This coherent coupling between reactivity

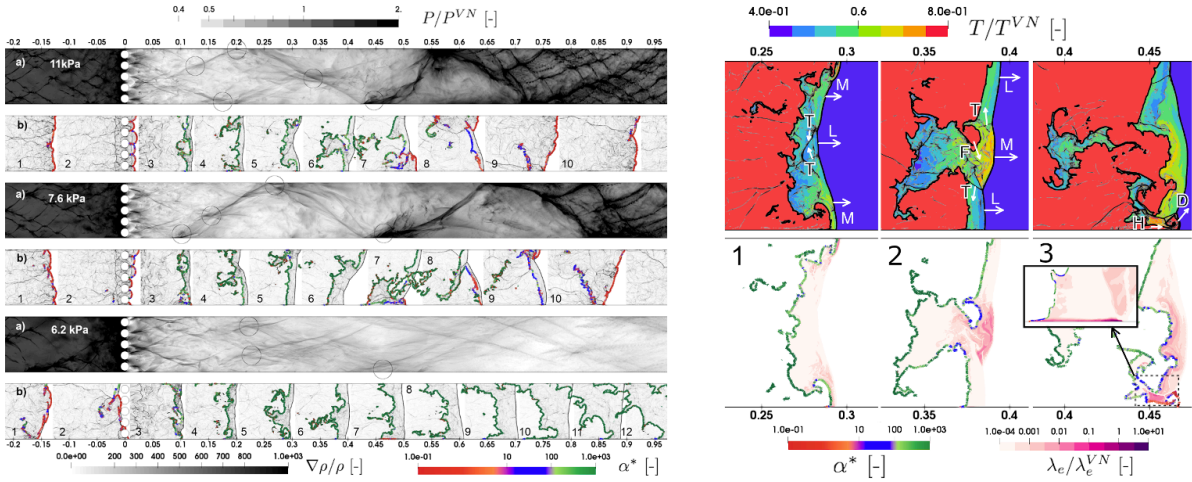


Figure 2.20: (left) Numerical soot foil (a) and (b) multiple frames of instantaneous numerical Schlieren for selected realizations at three different initial pressures and $BR = 75\%$. Isocontours of progress variable $c = 0.05$ are superimposed on numerical Schlieren fields and colored by $\alpha^* = \alpha(c = 0.05)$. (right) Snapshots in the region surrounding the successful detonation re-initiation for the case at $P_{init} = 11\text{kPa}$, $BR = 75\%$: temperature field with superimposed Schlieren (top) Isocontours at progress variable $c = 0.05$ superimposed on λ_e fields and colored by α^* . L: leading shock, T: transverse shock, M: Mach stem, F: flame finger, H: hotspot, D: detonation. Adapted from [50].

and pressure waves leads to the re-amplification of the transverse perturbations, which eventually triggers the detonation re-initiation. Regions of pressure wave amplification are also well capture by the chemical explosive mode, *i.e.* high chemical explosive mode $\lambda_e/\lambda_e^{VN} \gg 10^{-2}$.

In the context of LES modeling, where different models are to be used depending on the local combustion regime, this CSP based criterion is local and offers the possibility to be used to systematically identify deflagration, detonation and auto-ignition zones, and automatically switch between different modeling formulations, chemistry descriptions, resolution requirements when coupled to Adaptive Mesh Refinement (AMR) techniques.

Fundamentals of the chemical inhibition of propagating flames

Sommaire

3.1	Context	33
3.2	The controlling parameters of 1D flame inhibition	34
3.3	Modeling challenges of the inhibition of deflagration waves	48

3.1 Context

The high effectiveness of several compounds (gaseous, liquid or solid) in extinguishing flames has contributed to their wide use in industrial safety as fire suppressant. Until the 1970s, Halon 1301 (CBrF_3) was the most widely used fire suppressant in ground, sea and air systems [56] because of its remarkable performance and its low toxicity. However, following the Montreal protocol of 1987, the halons were banned from production in most developed countries due to their threat to the ozone layer. This sparked an intense period of search for Halon replacements and extensive research programs emerged aiming at: (1) identifying the Halon 1301 properties responsible for its exceptional effectiveness and (2) searching for substances that shared the most similarities with the Halon 1301 and could serve as alternatives for fire suppression. Examples for such programs are described in [57] and [58]. These research programs expanded upon the knowledge acquired back then on flame suppression chemistry, mostly related to halogen- (F, Cl, Br, ...) and alkali metal- (Li, Na, K, ...) containing species, to include extensive investigations on transition metal compounds (mostly Fe, Sn, Mn, ...) [59]. A ranking of these flame inhibitors is now available, based on their efficiency at suppressing a given flame.

Although injecting substances when fires are detected is a conventional technique to suppress fires in industrial fire safety, its application to gas explosions is not as mature.

Several programs emerged in the recent years to find efficient mitigation solutions to gas explosions using inhibitors that were already known to be efficient against fires. TotalEnergies has developed such a solution for natural gas explosions using potassium containing powders, and has proven their efficiency against deflagrations [60]. TotalEnergies funded several studies [61–64] at CERFACS aiming at: (i) understanding the mechanisms driving flame inhibition; (ii) modeling the impact of inhibitors on deflagration waves. The content of these studies is discussed in this chapter.

Before presenting the results, some definitions are useful for the reader naïve to the field. The term flame *inhibition* is used here to refer to the lowering of the overall exothermic reaction rate in the flame, by either thermal or chemical mean, without necessarily entailing suppression. Flame *suppression* is the state of flame inhibition where a flame front can not be sustained in a given flow. The mechanism by which inhibitors are able to efficiently act on flames can be complex and exhibit different natures. Liquid and solid substances intrinsically induce a thermal effect on the flame since evaporation/decomposition inside the flame provides a heat sink to the reaction zone. However, most of the compounds exhibiting high flame suppression effectiveness were shown to exhibit some sort of chemical action on the flame [58], including alkali salts [65–67]. This chemical action is carried out by one or several gaseous species liberated inside the reaction zone.

Section 3.2.1 delves into the fundamental description of the gas-phase kinetics associated to flame inhibition and Section 3.2.2 will include the decomposition/evaporation part to highlight its controlling parameters. Throughout this chapter, emphasis will be made on the case of H₂/air flames for their importance in the context of energy transition and the safety concerns they pose (see Chapter 2).

3.2 The controlling parameters of 1D flame inhibition

To investigate the controlling parameters of flame inhibition, a canonical 1D formulation of the flame/inhibitor problem is adopted. In it, a premixed flame at a given mixture and equivalence ratio ϕ is enriched on the unburnt gas side by various amounts of inhibitor agent (gaseous or solid). When in gaseous form, the reactive mixture is enriched while the equivalence ratio $\phi = X_{fuel}/sX_{O_2}$ is held constant (s is the molar stoichiometric coefficient). In other words, the addition of gaseous agent is performed at iso- ϕ , while X_{fuel} can vary.

3.2.1 Fundamentals of gas-phase flame inhibition: from dilution to auto-catalytic radical scavenging

3.2.1.1 Problem formulation

Most effective inhibitors are in liquid or solid forms at ambient conditions and their gas-phase effect on flame chemistry is carried by a set of gaseous agents they produce during their decomposition/evaporation in the flame [58]. To isolate the gas-phase effects

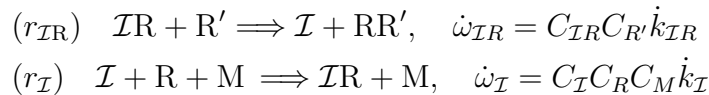
associated to the inhibition process, the gaseous inhibiting agent can be injected directly in the reactive mixture. We have clarified the set of assumptions allowing this simplification in [62, 63]. We briefly recall here the most important constituting assumptions (excluding the obvious ones leading to the 1-dimensionalisation):

- *fast liberation of the gaseous agent*: the gaseous agent is assumed to be liberated very early inside the flame front during the inhibitor/flame interaction; *i.e.* the thermal (evaporation for liquids and thermal decomposition for solids) and kinetic processes responsible for the production of the gaseous agent from the initial molecule are fast compared to the flame residence time $\tau_f = \delta_d/s_L$, with δ_d is the diffusive flame thickness;
- *negligible thermal perturbation* of evaporation and decomposition processes for liquid and solid inhibitors respectively.

These assumptions are valid for dispersed liquid/solid phases comprised of particles under a critical radius [63]. Despite these drastic simplifications, this problem is still useful to highlight the kinetics governing the intricate flame/inhibitor interaction. This problem has also been one of the major tools guiding the search for halons alternatives [58].

3.2.1.2 Elementary flame inhibition kinetics

The mechanism by which a chemical agent will act on flame chemistry can be complex and is not unique. However, it can be simplified down to a 2-step cycle [59, 68]:



where R and R' are two radical species, typically H, OH, O, HCO ... RR' is a stable product and M is a third body. \mathcal{I} stands for the active moiety, *i.e.* Na, K, Br, etc ... $\mathcal{I}R$ is the gaseous agent responsible for chemical inhibition and liberated during the decomposition/evaporation of the initial substances, *i.e.* $\mathcal{I}R = \text{NaOH}$ (KOH resp.) when NaHCO_3 (KHCO_3 resp.) is considered.

- The first step ($r_{\mathcal{I}R}$) is a recombination reaction that enhances the consumption of radical species R' . Alone, this reaction can not explain the high efficiency of chemical inhibition, as highlighted by Dixon-Lewis and collaborators [69, 70].
- The second step ($r_{\mathcal{I}}$) contribute to the re-generation of the gaseous agent $\mathcal{I}R$, while consuming another radical species R . When its rate is sufficiently high, it is able to support the first reaction leading to an auto-catalytic cycle.
- A set of radical species (R-R') is therefore associated to the inhibition cycle: for example, (H-OH-HCO) [71], (H-OH) [72] and (O-O) [73] for Br, Na and Fe containing species respectively.

The reason this auto-catalytic cycle is so efficient at inhibiting flames is related to the strong link between burning velocity and peak concentration of certain radical species (H for example) as evidenced in the 1960s [74] for H₂-O₂-N₂ flames, substantiated by the pioneering chain-branching model for flame velocity by Zeldovich [75] and much later by the theoretical derivations of Clavin and coworkers [76, p. 408]. The profound perturbation to the radical species chemistry induced by this auto-catalytic cycle has therefore a direct depleting effect on burning velocity, even at low gaseous agent concentration. The efficiency of an inhibition cycle ($r_{\mathcal{I}R}$)-($r_{\mathcal{I}}$) can therefore be characterized by the slope of the curve $s_L = f(Y_{\mathcal{I}R,u})$, where $Y_{\mathcal{I}R,u}$ is the mass fraction of the gaseous agent mixed with the reactants.

Chemical inhibition corresponds to a perturbation of the radical pool chemistry by enhancing chain-termination. The effective consumption source term of the radical species R and R' read:

$$(\dot{\omega}_{R',c})_{\text{eff}} = \dot{\omega}_{R',c} + \dot{\omega}_{\mathcal{I}R} = \dot{\omega}_{R',c} (1 + Y_{\mathcal{I}R} \mathcal{K}_{\mathcal{I}R}) \quad , \quad \text{with: } \mathcal{K}_{\mathcal{I}R} \equiv \frac{\dot{k}_{\mathcal{I}R}/W_{\mathcal{I}R}}{\dot{\omega}_{R',c}/\rho C_{R'}} \quad (3.1)$$

$$(\dot{\omega}_{R,c})_{\text{eff}} = \dot{\omega}_{R,c} + \dot{\omega}_{\mathcal{I}} = \dot{\omega}_{R',c} \left(\frac{\dot{\omega}_{R,c}}{\dot{\omega}_{R',c}} + Y_{\mathcal{I}} \mathcal{K}_{\mathcal{I}R} \mathcal{K}_{\mathcal{I}} \right) \quad , \quad \text{with: } \mathcal{K}_{\mathcal{I}} \equiv \frac{C_M \dot{k}_{\mathcal{I}}/W_{\mathcal{I}}}{\dot{k}_{\mathcal{I}R}/W_{\mathcal{I}R}} \quad (3.2)$$

which highlights the role of two non-dimensional rates:

- $\mathcal{K}_{\mathcal{I}R}$ measure the rate of the first inhibition reaction ($r_{\mathcal{I}R}$) with respect to the rate of consumption of radical R' .
- $\mathcal{K}_{\mathcal{I}}$ measure the rate of the second inhibition reaction ($r_{\mathcal{I}}$) with respect to the first step in the inhibition cycle. It controls the regeneration of the inhibitor agent $\mathcal{I}R$ during the cycle.

$\mathcal{K}_{\mathcal{I}}$ is a constant (low thermal sensitivity of radical recombination reactions [62]) but $\mathcal{K}_{\mathcal{I}R}$ is not. Nevertheless, we have shown in [64] that the value of $\mathcal{K}_{\mathcal{I}R}$ at the radical pool position (peak of H radical for example) is sufficient to completely describe the problem.

3.2.1.3 Flame inhibition efficiency: a kinetic point of view

In [62], we focused on flame inhibition chemistry associated to alkali metals and performed a time scale analysis of the inhibition problem to identify the main parameters controlling their inhibition efficiency against different mixture compositions (fuel, equivalence ratio, etc...). This is not presented here. Instead, we present a more general formulation of the problem described in [64]. In [64], we did not assume a specific gaseous agent nor a specific value for the rates of the inhibition cycle $\dot{k}_{\mathcal{I}R}$ and $\dot{k}_{\mathcal{I}}$.

Instead, they are all free parameters of the problem and we address the gas-phase flame inhibition problem from a kinetic point of view, driven by the two following questions: (Q1) can we define chemical bounds for flame inhibition based on the rates of the inhibition cycle ($r_{\mathcal{I}R}$)-($r_{\mathcal{I}}$) ?; (Q2) can we use these bounds to revisit the classification of flame inhibitors?

(Q1.1) Chemical limits to gas-phase flame inhibition: Analyzing the inhibition cycle ($r_{IR}-r_I$), two kinetic limits can be easily recognized, **both characterized by a constant mass fraction of inhibitor agent $Y_{IR} = cst.$ across the flame:**

- *dilution limit:* independently of the value of the rate of the regeneration reaction $\dot{\omega}_{\mathcal{I}}$, chemical inhibition is completely deactivated when $\dot{\omega}_{\mathcal{I}R} \rightarrow 0$, whereby the gaseous agent $\mathcal{I}R$ acts just as a diluent. Therefore, this limit represents a lower kinetic bound for the chemical inhibition efficiency of the inhibition cycle ($r_{IR}-r_I$). The reduction of the flame speed by diluents is explained by the thermal sensitivity of flames. This can be shown theoretically, using simple *ZFK*-type asymptotic analysis which allows to relate flame speed and burnt gas temperature, valid to leading order in the limit $Y_{dil} \rightarrow 0$ (see [64]):

$$\frac{T_b^0}{T_b} \approx 1 + \frac{\sigma^0 - 1}{\sigma^0} \left(\frac{c_{p,dil}}{c_{p,u}^0} \right) Y_{dil} \quad (3.3)$$

$$\frac{s_L}{s_L^0} \approx \sqrt{\frac{D_{th}}{D_{th}^0}} \exp \left(-\frac{\beta^0}{2} \left(\frac{c_{p,dil}}{c_{p,u}^0} \right) Y_{dil} \right) \quad (3.4)$$

$$\text{with: } \beta^0 \equiv \frac{\text{Ta}(T_b^0 - T_u)}{(T_b^0)^2} \quad \text{and} \quad \text{Ta} \equiv -2 \frac{\partial \ln(s_L)}{\partial (1/T_b)} \Big|_{Y_{dil} \rightarrow 0} \quad (3.5)$$

where the Zeldovich number β^0 is re-introduced and $\sigma^0 \equiv T_b^0/T_u$ denotes the diluent-free dilatation ratio. $c_{p,dil}$ and $c_{p,u}^0$ stand for the heat capacity of the diluent and the diluent-free mixture respectively, taken at the fresh gases. A reasonable agreement is observed between the predictions of Eq. (3.3)-(3.4) and the numerical results in Figure 3.1 even at large concentrations of diluent. More importantly, Eq. 3.3 shows that the controlling parameter of dilution is the non-dimensional heat capacity of the diluent $c_{p,dil}/c_{p,u}^0$, which takes the value 0.63, 0.51 and 3.16 for N_2 , CO_2 and He respectively, thereby explaining the higher thermal impact of He in Figure 3.1.

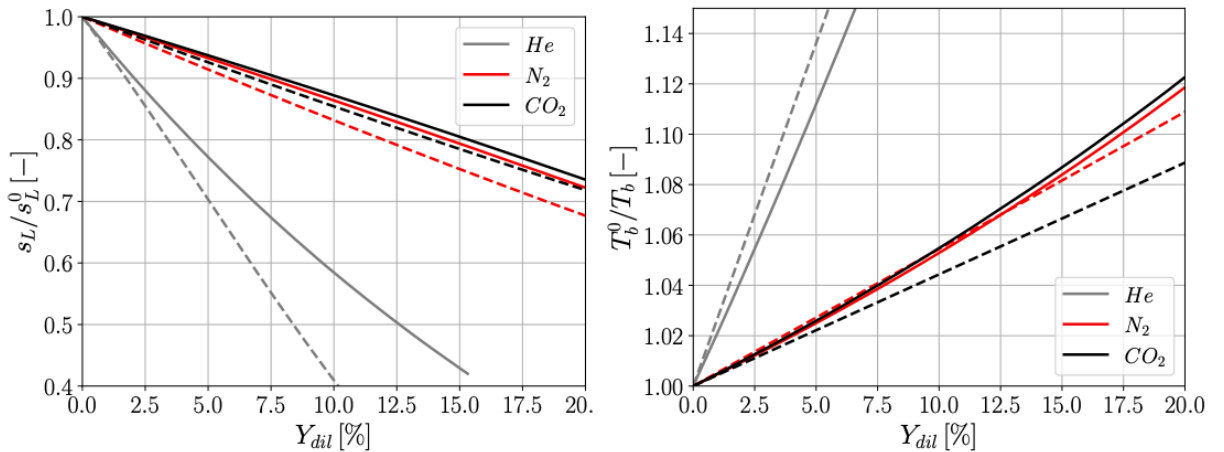
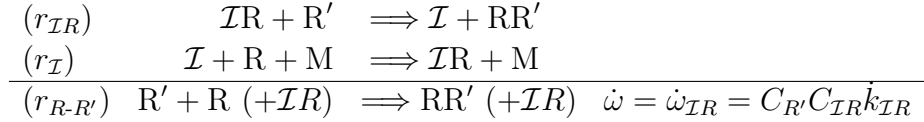
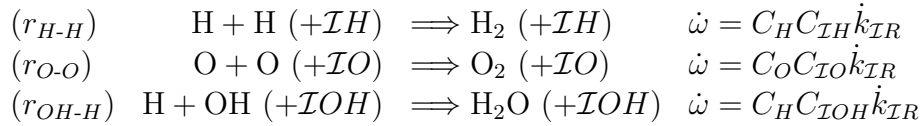


Figure 3.1: Evolution of the normalized flame speed s_L/s_L^0 (left) and burnt gas temperature T_b^0/T_b (right) with the diluent mass fraction for a H_2 /air flame at $\phi = 1.7$. Dashed lines correspond to the theoretical relations Eq. 3.4 and 3.3 respectively. Adapted from [64].

- *fast regeneration limit*: when $\dot{\omega}_{\mathcal{I}} = \dot{\omega}_{\mathcal{I}R}$, the gaseous agent $\mathcal{I}R$ is regenerated at the same rate as it consumes radical R via the first reaction. This ensures that the inhibitor agent $\mathcal{I}R$ concentration is constant inside the flame front which allows for a very efficient radical scavenging that can take place as long as radicals $R-R'$ are available. No further gain can be achieved by having an even faster second-step since the first reaction is limiting. Therefore, this limit represents an upper kinetic bound for the chemical inhibition efficiency of the inhibition cycle ($r_{\mathcal{I}R}-r_{\mathcal{I}}$), which reduces to the radical recombination reaction:



where the rate of the net reaction ($r_{R-R'}$) is 0-th order in R and the inhibitor agent $\mathcal{I}R$ acts as a third body with constant mass fraction. The inhibition cycle therefore reduces to a perturbation of the rate of radical recombination reactions already present in the flame sub-mechanism:



These three reactions are already present in H_2 /air chemistry mechanisms [77]. With

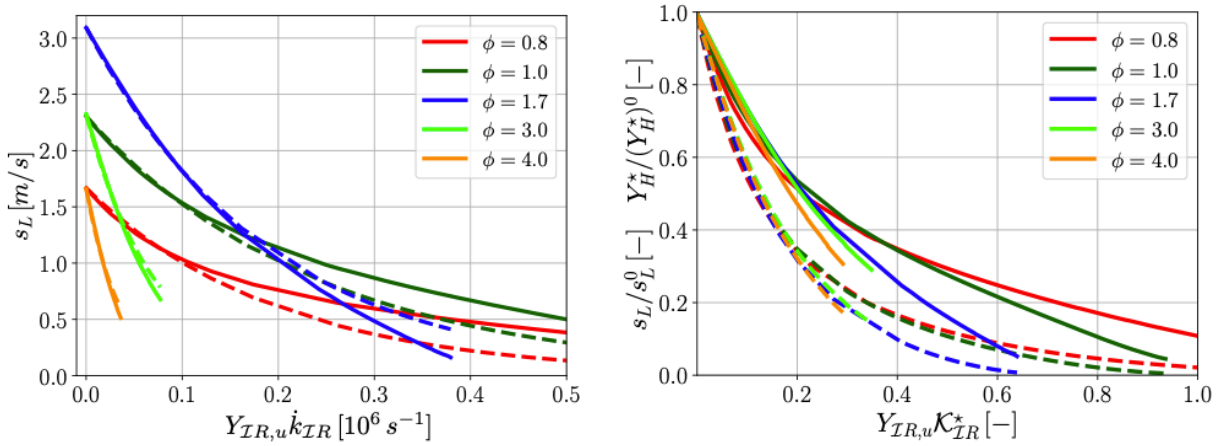


Figure 3.2: (left) Evolution of the flame speed s_L with the rate of the recombination reaction (r_{H-H}). (right) Evolution of the normalized flame speed and peak radical H mass fraction with the normalized rate of the recombination reaction (r_{H-H}). The results are shown for H_2 /air flames at different equivalence ratio ϕ . In (left), the numerical results (solid lines) are compared with the prediction of Eq. (3.6) (dashed lines). Adapted from [64].

their usual rates, they are not important for atmospheric very-lean H_2 /air flames [78]. Reactions (r_{H-H}) and (r_{OH-H}) are important for an accurate prediction of H radical peak concentrations in stoichiometric and rich mixtures [77]. However, the rate of

the reactions (r_{H-H}) - (r_{OH-H}) has a different form compared to their counterpart in the flame sub-mechanism. Fig. 3.2 shows the impact of the rate of the recombination reaction (r_{H-H}) on the flame speed for H_2 /air flames at different equivalence ratios. It shows that rich mixtures are much more sensitive to the perturbation of the rate of the recombination reaction (r_{H-H}) and that a collapse of all the curves is obtained when the rate of the recombination reaction (r_{H-H}) is scaled by the consumption rate of the radical $R' = H$ of the free flame, *i.e.* $\dot{\omega}_{IR}/\dot{\omega}_{c,R'}^* = Y_{IR,u}\mathcal{K}_{IR}^*$ where \mathcal{K}_{IR} is defined in Eq. (3.1) and $*$ indicates an evaluation at the radical pool position. Fig. 3.2(right) shows that this non-dimensional rate $Y_{IR,u}\mathcal{K}_{IR}^*$, a simple scalar parameter measuring the rate of (r_{H-H}) with respect to the consumption rate of the radical H at the free flame condition, is sufficient to account for the sensitivity of H_2 /air flames to the radical recombination reaction (r_{H-H}) : both in terms of radical H consumption and flame speed reduction. In a manner analogous to the dilution limit Eq. (3.4), we proposed a simple model for the chemical inhibition under the fast regeneration limit that stems from the observation that the flame speed reduction is exponential-like in $Y_{IR,u}\mathcal{K}_{IR}^*$ as suggested by Noto et. al [79]:

$$s_L \propto \exp(-\Gamma_{R-R'}Y_{IR,u}\mathcal{K}_{IR}^*) \implies \frac{\partial \ln(s_L)}{\partial Y_{IR,u}\mathcal{K}_{IR}^*} = -\Gamma_{R-R'} \quad (3.6)$$

$$\text{with } \mathcal{K}_{IR}^* \equiv \frac{\dot{k}_{IR}/W_{IR}}{\dot{\omega}_{c,R'}^*/C_{R'}^*} \quad (3.7)$$

$\Gamma_{R-R'}$ is equivalent to a non-dimensional semi-logarithmic flame speed sensitivity coefficient to the rate of the radical recombination reaction $(r_{R-R'})$. To show the pertinence of these two parameters $\Gamma_{R-R'}$ and $Y_{IR,u}\mathcal{K}_{IR}^*$, the analysis was carried out for the other cycles as well in Fig. 3.3. It highlights the drastic loss of inhibition efficiency with the cycle $O-O$ compared to the other cycles, which is also described by the low values associated to Γ_{O-O} . This result is in accordance with the proposed reduced mechanisms for H_2 /air combustion, in which the recombination reaction (r_{O-O}) is systematically neglected with negligible loss of accuracy [77, 78]. $H-H$ and $H-OH$ cycles exhibit similar inhibition efficiencies because they are linked by strongly coupled shuffle reactions describing the radical composition at the radical pool [77].

(Q1.2) Transition between chemical limits For a given inhibition cycle and a given flame, the efficiency of the inhibition cycle at reducing the flame speed depends on two scalar parameters: the rate of its two reactions $\mathcal{K}_{IR}^*\mathcal{K}_I$ evaluated at the radical pool position. The chemical inhibition efficiency lies within a peninsula illustrated in Fig. 3.4(right) for the $H-OH$ cycle, bounded by the two limites discussed above in answering (Q1.1):

- (Criterion for the dilution limit) An inhibitor can be qualified as a pure diluent when the rate of the first inhibition reaction is sufficiently low that the inhibitor does not have the time to consume reactants. More formally, we provide in [64] an explicit

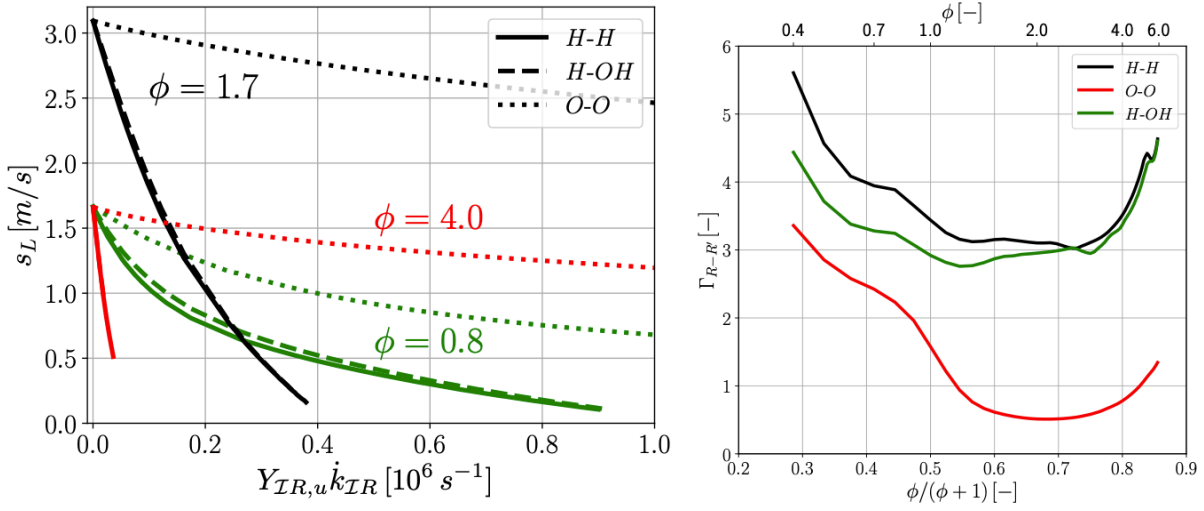


Figure 3.3: (left) H_2 /air flame sensitivity to the three recombination reactions (r_{H-H}), (r_{H-OH}) and (r_{O-O}) under the same rate $Y_{IR,u} \dot{k}_{IR}$ and for three equivalence ratios. (right) Evolution of the flame speed sensitivity parameter $\Gamma_{R-R'}$ with equivalence ratio for the three cycles (r_{H-H}), (r_{H-OH}) and (r_{O-O}). $\Gamma_{R-R'}$, defined in Eq. (3.6), measures the sensitivity of the flame speed to the inhibition cycle $R-R'$ under the fast regeneration limit. Adapted from [64].

criterion:

$$\frac{s_L}{s_L^0} \approx \sqrt{\frac{D_{th}}{D_{th}^0}} \exp\left(-\frac{\beta^0}{2} \left(\frac{c_{p,IR}}{c_{p,u}^0}\right) Y_{IR,u}\right) \quad \text{if} \quad \mathcal{K}_{IR}^* \ll \frac{\beta^0}{2\Gamma_{R-R'}} \left(\frac{c_{p,IR}}{c_{p,u}^0}\right) \quad (3.8)$$

which yields a value for $\mathcal{K}_{IR}^* \ll 0.5$ in reasonable agreement with the results of Fig. 3.4(left).

- (Criterion for the efficient single step inhibition) as soon as the rate of the first step is higher than the criterion provided above, chemical inhibition is activated. Without the support of the second step, *i.e.* $\mathcal{K}_I = 0$, an efficient single-step inhibition can still be achieved when:

$$\mathcal{K}_{IR}^* \gg \frac{\beta^0}{2\Gamma_{R-R'}} \left(\frac{c_{p,IR}}{c_{p,u}^0}\right) \quad \text{and} \quad \mathcal{K}_I \mathcal{K}_{IR}^* \ll 1 \quad (3.9)$$

When this condition is achieved, the high rate of the inhibition reaction compensates for the small mass fraction of radical H in the preheat zone of the flame and the inhibitor agent is entirely consumed very early inside the flame front. Past this point, no more chemical inhibition efficiency can be achieved without an inhibitor regeneration step $\mathcal{K}_I = 0$.

- (Criterion for the fast regenerative limit) Finally, an optimal flame inhibition is achieved when both steps of the inhibition cycle are fully activated, which formally

reads:

$$\mathcal{K}_{IR}^* \gg \frac{\beta^0}{2\Gamma_{R-R'}} \left(\frac{c_{p,IR}}{c_{p,u}^0} \right) \quad \text{and} \quad \mathcal{K}_I \gg \mathcal{K}_{IR}^* \quad (3.10)$$

as demonstrated in Fig. 3.4(right).

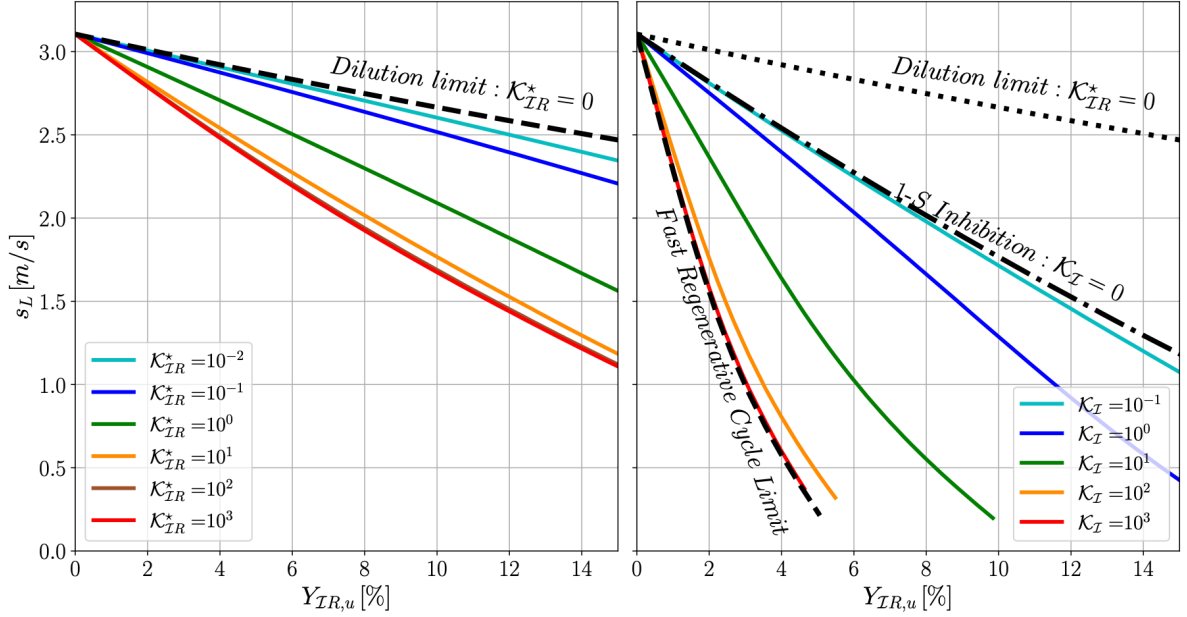


Figure 3.4: Evolution of the laminar flame speed s_L with mass fraction of inhibitor agent $Y_{IR,u}$ for a H_2 /air flame at $\phi = 1.7$ inhibited by a $H-OH$ inhibition cycle. (left) Case $\mathcal{K}_I = 0$, *i.e.* $H-OH$ cycle is reduced to a single step reaction $\mathcal{I}OH + H \rightleftharpoons \mathcal{I} + H_2O$ whose normalized rate is controlled by \mathcal{K}_{IR}^* . (right) Impact of different values of inhibitor regeneration rate $\mathcal{K}_I \neq 0$, with fixed $\mathcal{K}_{IR}^* = 10$. Adapted from [64].

(Q2) Implications for the classification of flame inhibitors The analysis shown above allowed to describe flame inhibition using exactly 5 parameters (a drastic reduction in the dimension of the parameter space of the problem):

- *Flame describing parameters:* the Zeldovich number β^0 which measures the flame thermal sensitivity and the coefficient $\Gamma_{R-R'}$ which measures the flame speed sensitivity to perturbation in the rate of some of its radical recombination reactions. These parameters are independent of the inhibitor or its cycle and can therefore be computed without the knowledge of inhibitor's chemistry.
- *Inhibitor describing parameters:* $c_{p,IR}/c_{p,u}^0$ characterizes the thermal action of the gaseous agent. The kinetic rates \mathcal{K}_{IR}^* and \mathcal{K}_I describe the efficiency of the radical scavenging reactions in depleting the radical pool.

These parameters are all non-dimensional and relate inhibitor properties to flame characteristics, whereby the destruction rate of the radical species in the free flame is systematically used as a scaling parameter for the rates of the inhibition reactions. One important point is that these 5 governing parameters are global variables which can be evaluated without the necessity to compute inhibited flames or experiments and require only two inputs: (1) an inhibitor-free flame profile computation and (2) a sub-mechanism for chemical flame inhibition.

Finding a good chemical inhibitor for newly considered mixtures, flames or thermodynamic conditions can be a tedious task as shown by the NGP [58] in the 1980s-1090s. Much more recent tentative applications of flame inhibition for H₂/air explosion mitigation [80] is also facing some serious challenges. The main problem is the large amount of combinations to be tested and analyzed. The present paper can serve as a guideline during screening phases. We proposed in [64] a paradigm, which allows a systematic and simple way to rank the inhibitor candidates and only inputs from inhibitor and flame chemistry:

- *Step 1: For a given flame, compute $\Gamma_{R-R'}$ for known inhibitor cycles.* This reduces to measuring the flame speed sensitivity to perturbations in the rate of recombination reaction associated to the fast regeneration limit of these cycles. These reactions are generally present in the flame mechanism. This step allows to identify the inhibition cycles to which the flame is the most sensitive (highest $\Gamma_{R-R'}$).
- *Step 2: Starting with the inhibition cycle with the highest $\Gamma_{R-R'}$, identify inhibitor candidates for which the inhibition mechanism is predominantly governed by each inhibition cycle.* This provides a preliminary ranking of the inhibitor candidates.
- *Step 3: Improved ranking based on increasing \mathcal{K}_{IR}^* and increasing \mathcal{K}_I .*

Of course, other considerations, outside of gas-phase chemistry, must be factored in. For example, liquid and solid inhibitors have a particle size to be minimized so that the chemical agent can be liberated inside the radical pool position. This is addressed in the next section.

3.2.2 A model for heterogeneous flame inhibition: explicit formulae for the critical particle size

The studies on gas-phase inhibition shown so far are only valid when the gaseous agent is already present in the unburnt gases. In practice, most efficient inhibitors are in solid or liquid form at ambient conditions and the gaseous agent is liberated when the solid/liquid inhibitors decomposes/evaporates inside the flame front. As stated in Section 3.2.1.1, the problem still reduces to pure gas-phase inhibition provided that the time scale of liberation, that we shall denote by τ_s , is very low compared to the flame residence time, namely $\tau_s \ll \tau_f \equiv \delta_L/s_L$. This condition may be verified when «small» particles are involved but is not a valid hypothesis in general. This begs the question of **what explicit criterion must a particle size satisfy for the particle to be deemed «small»?** And points to

a more general question of interest for industrial applications: **what explicit criterion must a particle size satisfy for the particle to decompose inside the flame front, thereby activation chemical inhibition?** We delved into these two questions in [63]. We present the main results here.

3.2.2.1 Problem statement

Suppose that an inhibiting dry powder is injected in the path of a freely propagating planar flame. P_s can be viewed as a discrete set of solid particles s composed of the solid inhibitor species \mathcal{I}_s . \mathcal{I}_s can be $(\mathcal{I}\text{HCO}_3)_s$ or $(\mathcal{I}_2\text{CO}_3)_s$ when $\mathcal{I}=\{\text{K}, \text{Na}\}$ for example. \mathcal{I}_s may be viewed as a carrier of gaseous agent $\mathcal{I}\text{R}$. The gaseous mixture is characterized by the mass fraction of gas $Z = \rho_g/(\rho_{P_s} + \rho_g) = \rho_g/\rho$, where ρ_{P_s} and ρ_g are the mass of powder and gas per unit volume respectively.

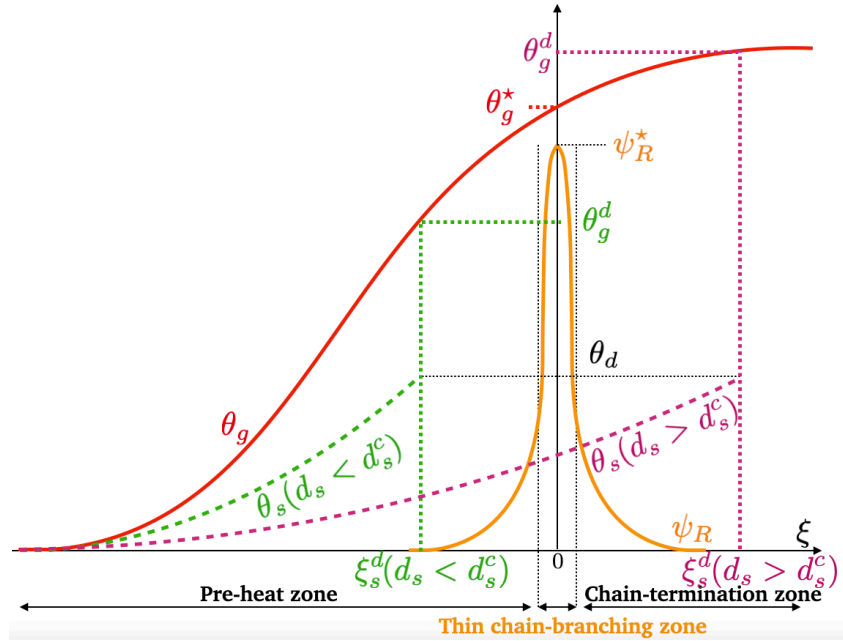
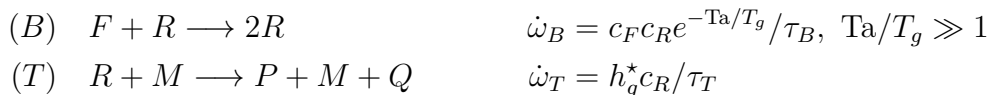


Figure 3.5: Schematic of the inhibited flame structure in the high activation energy limit $Ta/T_g^* \rightarrow +\infty$. Preheat and downstream zones of the flame are given by $\xi < 0$ and $\xi > 0$ respectively. The inhibiting particles temperature profile is depicted for two cases: (i) "small" particles, say for a particle size below a critical value d_s^c , where the decomposition temperature is reached inside the inner flame structure; (ii) "large" particles which reach decomposition in the burnt gases. Adapted from [63].

For chemistry, the choice has been made to take the simplest flame kinetics that includes radical species [81–83]. The model reads:



where T_g is the gas temperature. (B) is an autocatalytic chain-branching reaction by which a radical R reacts with the fuel F to form more radical species. (B) is thermally sensitive and under the high activation energy assumption ($Ta/T_g \gg 1$) is confined around a temperature denoted T_g^* , *i.e.* $\dot{\omega}_B = 0$ when $|T_g - T_g^*| > T_g/Ta \ll 1$. T_g^* is an unknown of the problem. Moreover, (B) is treated as non-exothermic and proceeds on a time scale τ_B . (B) is followed by the termination reaction (T) by which radical species are transformed into stable products P , which releases heat Q on a time scale τ_T . The function h_g^* is null when $T_g \leq T_g^*$ and unity otherwise. The results may be easily extended to the case $h_g^* = 1$.

The flame structure obtained with this chain-branching chemistry is illustrated in Fig. 3.5 with the non-dimensional variables: $\theta_g \equiv (T_g - T_u)/(T_{ad} - T_u)$, $\mathbb{Y}_k \equiv (W_F/W_k)(Y_k/Y_{F,u})$ and the reduced coordinates:

$$\xi \equiv \frac{1}{\sqrt{D_{th,u}\tau_T}} \int^x \frac{\rho_g}{\rho_{g,u}} dx' \quad (3.11)$$

Contrary to the single-step kinetics where the reaction zone is asymptotically pushed towards the burnt gases as $Ta/T_g \rightarrow \infty$, the chain-branching kinetics (B-T) de-correlate the thickness of the chain-branching zone, which effectively tends to zero as $Ta/T_g \rightarrow \infty$, from the temperature within the chain-branching zone θ_g^* , whose distance from unity is controlled by the ratio the reaction time scales τ_T/τ_B . For $\tau_T/\tau_B \gg 1$, the chain-termination zone takes more place in the flame structure and $\theta_g^* - 1 = O(1)$ is markedly far from unity. Inversely, when $\tau_T/\tau_B \ll 1$, the chemistry exhibits a thermal sensitivity similar to ZFK-type flames; *i.e.* $1 - \theta_g^* \ll 1$. This property is essential for studying H_2 /air flames whose structure exhibits a relatively large chain-termination zone.

We are interested in knowing how the particle size influences the position at which particles will reach the decomposition temperature, as illustrated in Fig. 3.5, with $\theta_s \equiv (T_s - T_u)/(T_{ad} - T_u)$. More specifically, we seek an explicit criterion for the particle size, of the type $d_s < d_s^c$, which would allow to characterize the particles with the potential of decomposing inside the flame front, thereby activating chemical inhibition (otherwise, they would decompose in the burnt gases with little to no chemical effect). A simplified decomposition model is assumed where the particle is only allowed to exchange heat with the surrounding gas below a given decomposition temperature T_d , mimicking the fact that the liberation of gaseous agent is known to be negligible below a temperature that depends on the inhibitor considered. The particles temperature and mass equations read:

$$\frac{dT_s}{dt} = (1 - h_s^d) (T_g - T_s) (C_{p,g}/C_{p,s}) / \tau_h \quad (3.12)$$

$$\frac{dm_s}{dt} = h_s^d \frac{m_s}{\tau_s} \quad (3.13)$$

$$\text{where } \tau_h \equiv (\rho_s d_s^2 \text{Pr}) / (6\mu_g \text{Nu}) \quad (3.14)$$

τ_s is a decomposition time scale, input of the problem. τ_h is the conductive heat transfer time scale, proportional to the square of the particle size d_s . Pr and Nu are the Prandtl

and Nusselt numbers respectively. μ_g is the gas viscosity. $C_{p,g}/C_{p,s}$ is the ratio of gas to particle calorific capacities. h_s^d is the step function:

$$T_s < T_d : h_s^d = 0 \quad \text{and} \quad T_s = T_d : h_s^d = 1 \quad (3.15)$$

It is acknowledged that equation (3.12)-(3.13) are far too simple to account for the intricacies of the inhibitor thermal decomposition process. They are however useful to represent the leading order behavior of the solid/gas conductive heat transfer while reducing the dimensionality of the thermal decomposition problem and drastically easing the analytical derivations.

3.2.2.2 The class of efficient particles: an explicit criterion

General solutions are provided in [63]. We restrict the discussion on one main result which describes the decomposition position in the gas temperature space, *i.e.* $\theta_g^d = \theta_g^d(\xi = \xi_s^d)$ with ξ_s^d the decomposition position (see Fig. 3.5) :

- For small particles, defined by $\xi_{s,d} < 0 \Leftrightarrow \theta_{g,d} \equiv \theta_g(\xi = \xi_{s,d}) < \theta_g^*$, the decomposition is reached in the pre-heat zone of the flame. The journey of the particles through the flame stops in the preheat zone and the thermal decomposition problem is chemically inert. Diffusion of heat in the flame and conductive heat transfer between gas and solid particles dictate the heating of the particles and $\theta_{g,d}$ depends on the non-dimensional heating characteristic length scale \mathcal{A}_h

$$\theta_{g,d} = \theta_d [1 + \mathcal{A}_h] = \theta_d \left[1 + \frac{(C_{p,s}/C_{p,g})\zeta^2}{6\text{Nu}(\rho_{g,u}/\rho_s)} \right] \quad \text{with,} \quad \zeta \equiv \frac{d_s}{\delta_-} = \frac{d_s}{D_{th,u}/s_L} \quad (3.16)$$

when the non-dimensional particle size ζ is scaled by the thickness of the preheat zone δ_- . Eq. (3.16) allows to obtain a condition, written in terms of particle size, that a particle must satisfy to fall into this class of small particles:

$$\theta_{g,d} < \theta_g^* \Leftrightarrow \zeta^2 \equiv (d_s/\delta_-)^2 < \frac{6\text{Nu}(\theta_g^*/\theta_d - 1)}{\rho_s C_{p,s}/(\rho_{g,u} C_{p,g})} \quad (3.17)$$

- Similarly, for larger particles that reach decomposition past the chain-branching zone, *i.e.* $\xi_{s,d} > 0 \Leftrightarrow \theta_g^* < \theta_g(\xi = \xi_{s,d}) \equiv \theta_{g,d} \leq 1$, chain-termination reactions start to play an import role in the heat transfer process because of their exothermic nature:

$$\theta_{g,d} = 1 + (\theta_g^* - 1)e^{-\zeta_L \mathcal{L}_R \xi_{s,d}} = \theta_d [1 - \mathcal{L}_R \mathcal{A}_h] + \mathcal{L}_R \mathcal{A}_h \mathcal{C}_g^s \quad (3.18)$$

where $\mathcal{C}_g^s = 1 - [\mathcal{A}_h/(1 + \mathcal{A}_h)] e^{-(\zeta_L/\mathcal{A}_h)\xi_{s,d}}$. According to Equation (3.18), the $\theta_{g,d} = f(\zeta)$ is controlled by the particle heating rate term \mathcal{A}_h and a term \mathcal{L}_R , defined in equation (3.19), which characterizes the relaxation of the radical species R to zero

via mass diffusion and chain-termination reactions:

$$\mathcal{L}_R \equiv \frac{\text{Le}_R}{2} \left(\sqrt{1 + \frac{4}{\varsigma_L^2 \text{Le}_R}} - 1 \right) \quad (3.19)$$

with $\varsigma_L = s_L / (\sqrt{D_{th,u}} / \tau_T)$ is the non-dimensional flame speed. Therefore, understanding the particle heating process for such particles requires additional information about the internal flame structure.

The set of particle sizes for which the decomposition position is reached inside the flame can be defined by $1 - \theta_{g,d} \geq \varepsilon$, where ε is a small number. According to equation (3.18), this is equivalent to the following condition on $\xi_{s,d}$: $(1 - \theta_g^*) e^{-\varsigma_L \mathcal{L}_R \xi_{s,d}} = \varepsilon$, which can be injected in equation (3.18) to give an analytical relation defining the critical particle heating time \mathcal{A}_h^c and equivalently the critical particle size ζ^c above which chemical inhibition is lost :

$$1 + \frac{1}{\mathcal{A}_h^c} = \frac{[\varepsilon (1 + \mathcal{L}_R)]^{\mathcal{A}_h^c / (\varsigma_L^2 \mathcal{L}_R)}}{(1 - \theta_d) (1 - \mathcal{A}_h^c / (\varsigma_L^2 \mathcal{L}_R))} \quad (3.20)$$

Provided that $\varepsilon (1 + \mathcal{L}_R) = O(1/\mathcal{A}_h^c) \ll 1$, one can expand the numerator on the rhs of Eq. (3.20): $x^x = 1 + x \ln(x) + O(x^2 \ln^2(x))$ as $x \rightarrow 0$ to obtain the following general criterion

$$\theta_{g,d} < 1 \iff (d_s / \delta_-)^2 < \frac{6\text{Nu} (1/\theta_d - 1)}{\rho_s C_{p,s} / (\rho_{g,u} C_{p,g})} [1 + \alpha (\delta_+ / \delta_-)] \quad (3.21)$$

where $\alpha \equiv -\ln(\varepsilon(1 + \mathcal{L}_R)) \geq 0$ and $\delta_+ / \delta_- = 1/\mathcal{L}_R = (1/\theta_g^* - 1)$ is the ratio of pre-heat to chain-termination length scales controlled by \mathcal{L}_R and equivalently the position θ_g^* of the chain-branching zone relative to burnt gases.

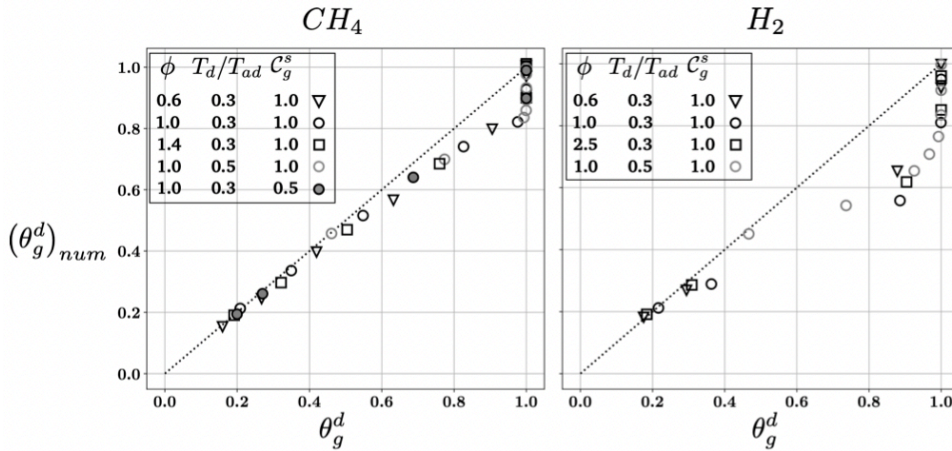


Figure 3.6: Decomposition position $(\theta_{g,d})_{num}$ computed numerically confronted to the value $\theta_{g,d}$ given by equation (3.16)-(3.18) for CH_4/air (a) and H_2/air (b) flames. Adapted from [63].

Eq. (3.21) is a general criterion linking the conductive heat transfer inside the flame to the complex chain-branching structure characterized by the ratio δ_+/δ_- . For most hydrocarbon flames, the chain-branching zone is located close to the burnt gases, so that the term $\delta_+/\delta_- \rightarrow 0$ in Eq. (3.21) can be neglected. However, for hydrogen/air flames, especially close to stoichiometry, the radical pool position can be quite far from the burnt gases, typically $\theta_g^* \approx 0.6$, in which case the term δ_+/δ_- increase the range of particle sizes able to decompose inside the flame, owing to the increased relative importance of the chain-termination zone in the flame structure. The analysis presented briefly in this section

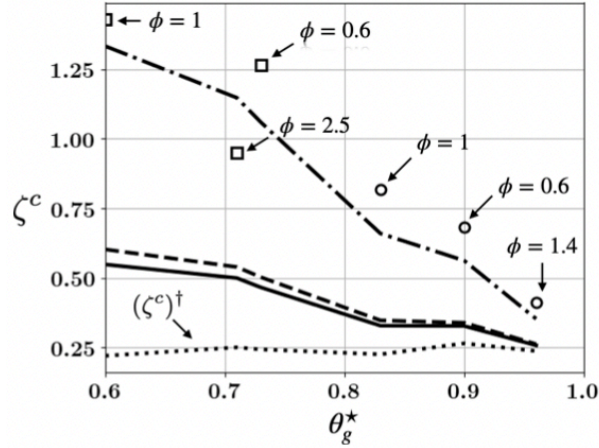


Figure 3.7: Critical particle size $\zeta^c = d_s^c/\delta_-$ evolution with chain-branching temperature θ_g^* . Symbols denote numerical values for CH₄/air (circles) and H₂/air (squares) flames with $T_d/T_{ad} = 0.3$, $C_g^s = 1$. Solid and dashed lines correspond to different approximations to equation (3.21). Dotted correspond to Eq. (3.22). Dot-dashed line correspond to (3.21) with $\alpha = 5.5$. Adapted from [63].

was confronted to detailed numerical simulations of the 1D flame/particle problem in [63]. The results for CH₄/air and H₂/air flames at different equivalence ratios, decomposition temperature and particle heat capacities are shown in Fig. 3.6. It shows the excellent agreement between the theoretical expressions and the numerical results for CH₄/air flames and the decrease in accuracy when switching to H₂/air flames.

Finally, a focus can be made on the critical particle size ζ^c above which particle decomposition is reached in the burnt gases. The dependence of ζ^c on the chain-branching temperature θ_g^* , obtained theoretically using Eq. (3.21) is confronted to the one obtained numerically. The numerical results confirm the trends predicted by Eq. (3.21): (1) a remarkable increase of the reduced critical particle size ζ^c with decreasing θ_g^* is indeed observed and can be explained, using Eq. (3.21), by the increase of the downstream flame zone thickness δ_+ with respect to the preheat (or upstream) zone thickness δ_- ; (2) ζ^c tends to its fast chain-termination counterpart, *i.e.* Eq. (3.21) with $\delta_+/\delta_- \rightarrow 0$ leading to:

$$\left(\frac{d_s^c}{\delta_-}\right)^2 \xrightarrow{\theta_g^* \rightarrow 1} \left((\zeta^c)^\dagger\right)^2 = \frac{6\text{Nu}(1/\theta_d - 1)}{\rho_s C_{p,s}/(\rho_{g,u} C_{p,g})} \quad (3.22)$$

Despite the complexity of the present problem, the analytical derivations performed

really capture the trends observed numerically, providing more insight into the role played by chain-branching and chain-termination reactions in this thermal problem. There is, however, a considerable discrepancy between the theoretical values and the one obtained numerically. A practical solution to this problem was proposed in [63], where α is set to be a free parameter in Eq. (3.21) and used to fit the numerical results. As shown in figure 3.7, using $\alpha = 5.5$ increases the accuracy of the analytical expressions. Although lacking rigor, this approach allows a practical use of the analytical criteria provided here while stemming from well-posed theoretical considerations.

3.3 Modeling challenges of the inhibition of deflagration waves

The application of flame inhibition to propagating deflagration waves exhibits some challenges directly related to the transient and N-dimensional nature of the problem, which are out of the scope for the 1D description provided in Section 3.2. We have proposed a first attempt at modeling the inhibition of self-propagating flames in [61]. The test case corresponds to a 2D planar CH_4/air flame propagating in a cloud of CH_4/air reactive mixture and a non-uniformly distributed layer of inhibitor particles. The inhibitor corresponds to sodium-bicarbonate. The test case is illustrated in Fig. 3.8 where case 0 corresponds to an homogeneous distribution and Case 2 to the most inhomogeneous one where no particles are present at the top of the domain. The inhibitor is modeled via a

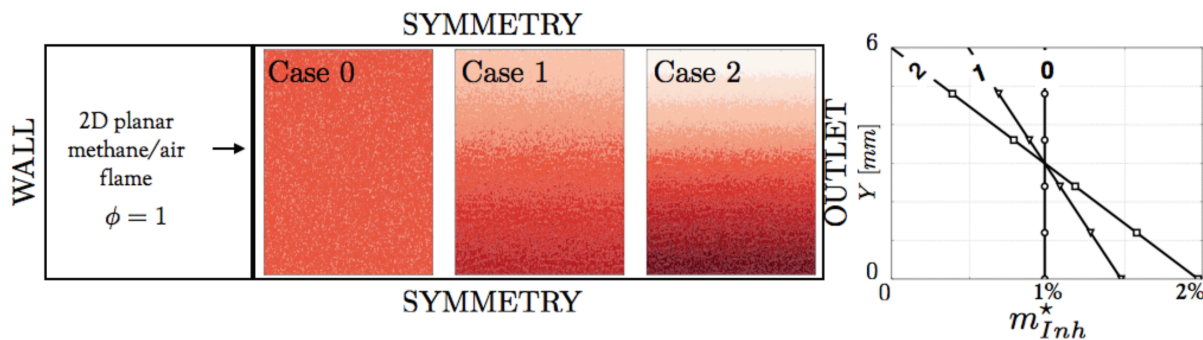
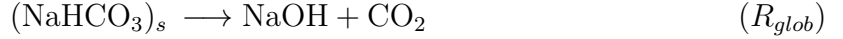


Figure 3.8: (left) Inhibitor distribution in the vicinity of a planar methane/air flame at stoichiometry and atmospheric conditions. The channel is 70 mm long and 6 mm wide. (right): Mass density distributions profile over the vertical axis for the three cases considered. Adapted from [61].

Lagrangian approach where all the inhibiting particles are tracked in time as detailed in [61]: (i) a point source approximation is used; (ii) Two-way mass, heat and momentum coupling between solid and gaseous phases are accounted for but collisions are neglected due to the low volume fractions considered; (iii) Stokes drag force is applied on the particles and in all simulations, the slip velocity of the particles remains small so that the particle Reynolds number is lower than 5 and the drag coefficient reads $C_d = 24/\text{Re}_p(1 + 3/16\text{Re}_p)$.

Similarly to Section 3.2.2, a simple single-step decomposition step is adopted:



where NaOH is the gaseous agent acting on flame radical pool chemistry. Major uncertainties surround the rate of the thermal decomposition of $(\text{NaHCO}_3)_s$ particles. The major relevant information is the temperature at which NaOH can be liberated (ie. $T_{decomp} = 1123K$). Therefore, a simplified model is proposed for the rate of reaction (R_{glob}):

- NaOH cannot be produced before the solid $(\text{NaHCO}_3)_s$ particle has reached T_{decomp} . Therefore, the mass of the particle is kept constant as long as $T_p \leq T_{decomp}$. The only source term left in the particle temperature equation is related to the gaseous conductive heat flux (Φ_g^c). For $T_p \leq T_{decomp}$:

$$\frac{dm_p}{dt} = 0 \quad (3.23)$$

$$\frac{dC_{p,p}T_p}{dt} = -\frac{\Phi_g^c}{m_p} \quad \text{where} \quad \Phi_g^c = \pi d_p N_u \frac{\lambda}{C_p} (C_p(T_p)T_p - C_p(T_\infty)T_\infty) \quad (3.24)$$

where d_p is the particle diameter, T_∞ is the farfield temperature, λ is the thermal conductivity and C_p the gas calorific capacity. $C_{p,p}$ is the particle calorific capacity. The Nusselt number is $N_u = 2$.

- Once T_{decomp} is reached, the particle undergoes fast decomposition. During this phase, the temperature of the particle T_p is assumed constant (Eq. (3.26)). t_p^* is, for each particle, the time when the decomposition temperature is reached: $T_p(t_p^*) = T_{decomp}$. The decomposition duration is fixed by the parameter $\tau_{decomp} = 10\mu s$ and kept small to ensure an almost instantaneous liberation of the gaseous agent. For $T_p = T_{decomp}$:

$$\frac{dm_p}{dt} = A\rho_p d_p \exp(-(t - t_p^*)/\tau_{decomp}) \quad (3.25)$$

$$\frac{dC_{p,p}T_p}{dt} = 0 \quad (3.26)$$

where ρ_p is the particle density and A is a constant set to $1 m^2/s$.

Such a model is too simple to account for all the details of the inhibition process. The model predicts an abrupt stepwise behavior of the inhibitor: if the particle reaches T_{decomp} inside the reaction region, it will decompose completely in the flame zone. Otherwise, it will vaporize without impacting the flame, which is certainly far from being true. Taking into account the temperature distribution inside the particle should improve this aspect of the model by reproducing the release of certain amount of Na-containing species inside the reaction zone for large particles due to surface decomposition. The set of equations above are useful to study numerically first order effects of sodium bicarbonate particles on flame propagation as long as their decomposition speed is large compared to all other phenomena.

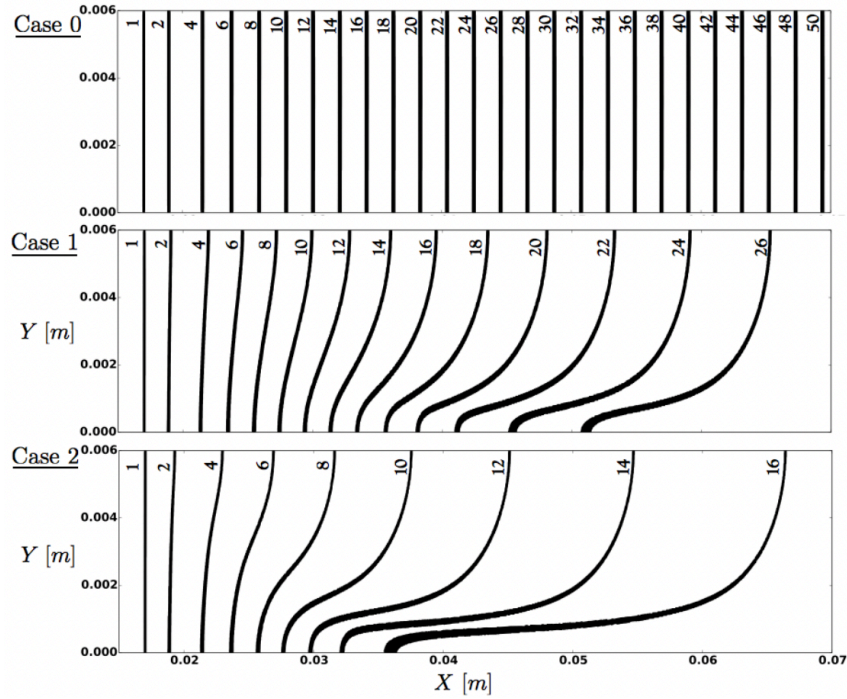


Figure 3.9: Propagation of a 2D initially planar methane/air flame in a inhomogeneous distribution of $(\text{NaHCO}_3)_s$ particles. The flame shape (isocurve of progress variable $c = 0.05$) and the corresponding time in milliseconds are shown for cases 0, 1 and 2. Adapted from [61].

An Analytically Reduced Scheme (ARS) was used to account for flame chemistry and the impact of the gaseous agent NaOH on the latter. The ARS contained 20 transported species, 156 reactions and 8 additional species in QSS.

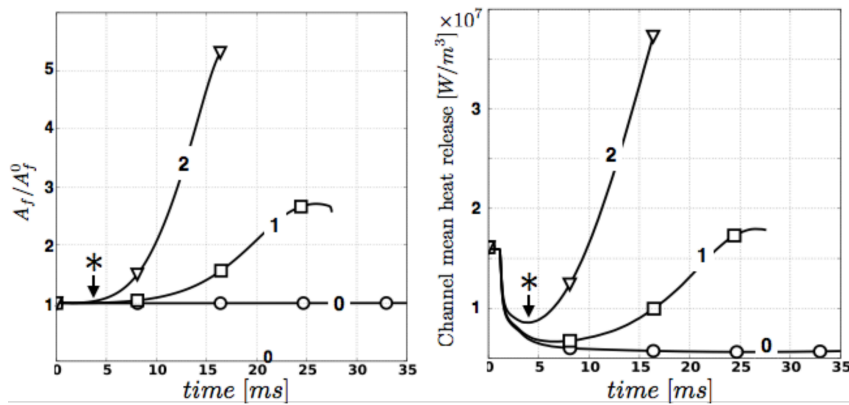


Figure 3.10: Flame response to $(\text{NaHCO}_3)_s$ particles distribution. Left: temporal evolution of the flame surface normalized by its initial value. Right: Temporal evolution of the mean heat release in the channel. The symbol * indicates the slope change in the heat release evolution for case 2 related to the transition from planar to finger shaped flame. Adapted from [61].

This first approach to the modeling of N-Dimensional heterogeneous flame inhibition

allowed to assess the effect of particles spatial distribution on the flame propagation. In practice, injection manifolds used to disperse inhibition powders in a gas can hardly guarantee an homogeneous particle distribution. Flame speed variations along the flame surface, in the case of inhomogeneous distribution, must be expected and they can induce flame surface increase which may offset inhibition effects as already suggested experimentally in the literature. The strong surface increase induced by this stratification of inhibitor is illustrated in Fig. 3.9 for the three cases.

Fig. 3.10 illustrates how the drastic increase in flame surface due to the stratified distribution of inhibitor can completely deplete the inhibition effect and even sustain flame acceleration for the extreme case 2. These first simulations showcase a potential counter-effect to flame inhibition when applied to propagating flames, something that is often overlooked in the literature. This has strong implications for the practical implementation of this mitigation solution against explosions since the homogeneity of the inhibitor prior to ignition can hardly be guaranteed simply because it depends on an unknown of the safety scenario: the ignition time, and more precisely the time delay between ignition and the start of the inhibitor dispersion. When this delay is too low, strong stratification can be expected and the kind of counter-effects highlighted with these first scenarios can be observed. This stresses the importance of developing reliable simulation tools to help in the design of injection strategies able to minimize the regions of strong stratification. We are not there yet and much must be done to enhance the predictive capabilities of the simulations shown here.

Main points of focus for future research efforts include: (i) the kinetics of thermal decomposition for powders, for which reliable parameters are scarce in the literature; (ii) the validity of the point-source approximation, which is far from being guaranteed in regions of high densities of inhibitors; (iii) the modeling of the flame/particle interactions for large scale problems, which is clearly lacking a rigorous validation especially for such strongly transient problems.

Mechanisms controlling the dynamics of reaction waves in novel combustion technologies

Sommaire

4.1	Flames embedded in porous media	53
4.2	Reaction waves in Pressure Gain Combustion (PGC) systems . .	62

4.1 Flames embedded in porous media

4.1.1 Context and funding

Flames within porous media present unique properties such as increased burning rate and broadened flammability limits, allowing stable combustion of very lean mixtures. The main mechanism underpinning this performance is commonly identified as the preheating of the fresh gases before the flame front, due to an upstream recirculation of combustion heat through the solid matrix. Heat recirculation may lead to a localized accumulation of enthalpy and temperatures above the equilibrium temperature - a feature often called superadiabatic or excess enthalpy combustion. Many coupled, multi-scale phenomena take place simultaneously, such as conduction, convection, interphase heat exchange, radiation and chemical reactions. This leads to a vast number of design possibilities and applications, but renders modelling generalizations more intricate. This section delves into their 1D modeling and 3D simulations.

All the work presented in this section on porous media combustion was part of the ERC project SCIROCCO, to which I contributed during my one-year stay at IMFT as a postdoctoral researcher. It was performed within the PhDs of **P. A. Masset** and **F.**

Muller. Their work is presented in Sections 4.1.2 and 4.1.3 respectively.

4.1.2 1D modeling of flames embedded in porous media

4.1.2.1 1D numerical simulations (SIM) and combustion regimes

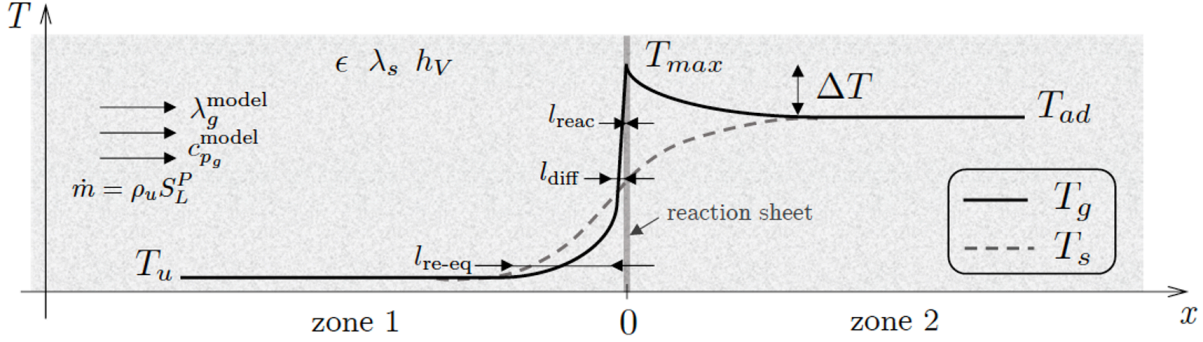


Figure 4.1: Illustration of the 1D porous media combustion problem. Adapted from [84].

The problem consists of a steady isobaric flame submerged in an infinite, inert and homogeneous porous medium, characterized by its porosity ϵ , thermal conductivity λ_s and volume heat transfer coefficient h_V with the gas. A 1D modeling of porous media combustion is possible thanks to the volume-averaging approach. A schematic of the problem is displayed in Fig. 4.1. This leads to the following set of fully coupled equations for the gas temperature T_g , species mass fraction Y_k and solid media temperature T_s (neglecting dispersion):

$$\begin{aligned} \dot{m} \partial_x Y_k + \partial_x J_k - \dot{\omega}_k &= 0, \\ \dot{m} c_{pg} \partial_x T_g - \partial_x (\lambda_g \partial_x T_g) + \sum_k c_{pg} k J_k \partial_x T_g + \sum_k h_k \dot{\omega}_k + \frac{h_V}{\epsilon} (T_g - T_s) &= 0 \\ \lambda_s \partial_x^2 T_s + \frac{h_V}{1-\epsilon} (T_g - T_s) &= 0, \end{aligned} \quad (4.1)$$

where c_{pg} and λ_g denote respectively the heat mass capacity of the mixture and the gas thermal conductivity. For each species k , J_k is the diffusive flux, $c_{pg,k}$ the heat mass capacity, h_k the mass enthalpy and $\dot{\omega}_k$ the mass production rate per unit volume. At the infinite upstream, the phase averaged mass flow rate is $\dot{m} \equiv \rho_u S_L^P$ equal to the product of the inlet density ρ_u and burning velocity S_L^P . For simplicity, the system is further assumed to be globally adiabatic, which neglects heat losses to the exterior, either by conduction, convection or radiation. The fresh mixture enters the domain at a temperature T_u and leaves at the equilibrium temperature T_{ad} .

The system of equations (4.1) was solved numerically by **P. A. Masset** in [84, 85] by coupling the CANTERA solver to an external, implicit centered finite differences solver to resolve the energy equation in the solid phase. The results are shown in Fig. 4.2 for increasing values of heat transfer coefficient h_V . 3 distinct combustion regimes can be observed, distinguished in terms of the relative values of three characteristic length scales of porous media combustion, depicted in Fig. 4.1, namely: (l_{re-eq}) defining the interphase

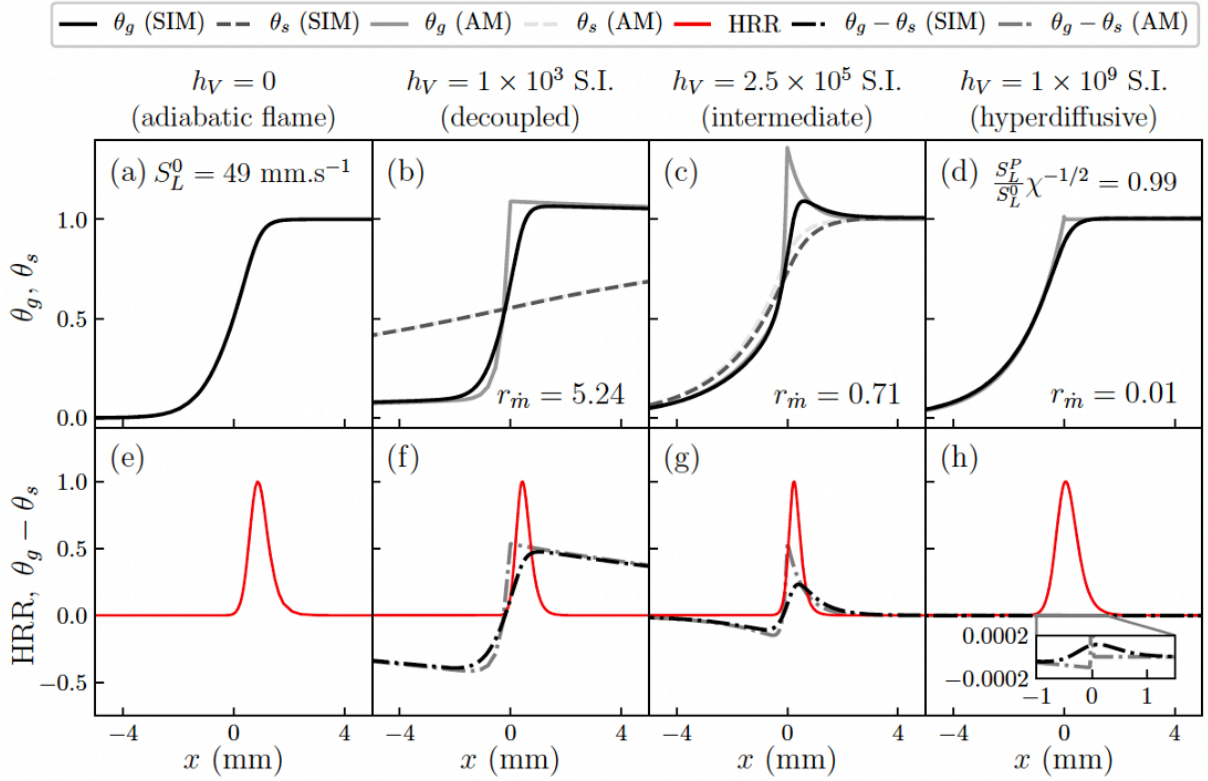


Figure 4.2: Solid and gas temperatures $\theta_{g,s} \equiv (T_{g,s} - T_u)/(T_{ad} - T_u)$, heat release rate and interphase out-of-equilibrium temperatures $\theta_g - \theta_s$ from the numerical simulations (SIM) and the analytical model (AM). Methane-air at $\phi = 0.5$. h_V in units of $W.m^{-3}.K^{-1}$. In case (b), θ_s for (AM) and (SIM) are superimposed. In case (d), $\theta_s \approx \theta_g$ both for (AM) and (SIM). Adapted from [84].

re-equilibration regions before and after the flame front, thereby representing the gas/solid out-of-equilibrium zone; (l_{diff}) related to heat diffusion in the gas phase; and (l_{reac}) defining the thickness of the reaction zone. Fig. 4.2 illustrates the three regimes that can be observed:

Decoupled regime - Figure 4.2(b) and (f) The decoupled regime was studied thoroughly in [85, 86]. It is characterized by large interphase non-equilibrium and small solid-temperature gradients, with extended re-equilibration zones before and after the flame front. On the scale of the flame, the solid temperature is nearly constant and the flame structure is very close to an adiabatic flame, shifted by a certain preheating temperature. In this regime, interphase heat transfer does not impact locally the flame structure and cleat scale separation is observed:

$$l_{re-eq} \gg l_{diff} \gg l_{reac}. \quad (4.2)$$

Hyperdiffusive regime - Figure 4.2(d) and (h) On the other side of the spectrum, the hyperdiffusive regime is achieved for large interphase heat transfer. In this regime,

solid and gas temperatures are almost equal, which means that a single-phase modelling is adequate. Little or no superadiabatic behavior is observed. The flame has a structure similar to an adiabatic flame, yet showing a smaller temperature gradient, indicating a larger effective diffusivity all across the flame front. This hints towards the denomination «hyperdiffusive». As shows the zoomed-in subplot of Figure 4.2(h), in that situation the re-equilibrium length scale is of the same order or smaller than the reaction length scale, indicating that interphase heat transfer plays a major role at the very heart of the flame front:

$$l_{\text{diff}} \gg l_{\text{reac}} \sim l_{\text{re-eq}}. \quad (4.3)$$

Intermediate regime - Figure 4.2(c) and (g) The intermediate regime covers a range of solutions for which the length scale of interphase re-equilibration $l_{\text{re-eq}}$ meddles with the classical length scale of diffusion in the gas phase l_{diff} , yet remaining larger than that of reaction:

$$l_{\text{diff}} \sim l_{\text{re-eq}} \gg l_{\text{reac}}. \quad (4.4)$$

This intermediate regime is governed by both superadiabatic and hyperdiffusive effects, where the maximal temperatures are found. Incidentally, this regime can be related to the «ultra-lean limit» studied by Pereira et al. in [87] with asymptotic theory.

4.1.2.2 Analytical formulae for the super-adiabaticity and burning velocity under the decoupled regime

Based on the observations of Section 4.1.2.1, it is possible to simplify the 1D problem (4.1) taking advantage of its characterizing scale separation property (4.2). In a manner analogous to the classical ZFK analysis, the reaction zone is considered as a discontinuity separating two chemically inert zones (1 and 2 in Fig. 4.1):

- the system (4.1) reduces to a chemically inert fully thermal problem $\mathcal{T}(\dot{m})$ that can be solved easily for T_s and T_g for a given value of mass flow rate \dot{m} . It provides the gas preheating ΔT at the discontinuity (reaction zone) as function of the mass flow rate and the parameters of the problem:

$$\frac{\Delta T}{T_{ad} - T_u} \equiv \eta_{rec} \approx \frac{\sqrt{h_V(1 - \epsilon)\lambda_s}}{2\dot{m}\epsilon c_{p_g}} \quad (4.5)$$

where η_{rec} measures the heat recirculation efficiency of the porous medium and can be shown to be not overly intense $\eta_{rec} \ll 5$. Eq. (4.5) shows that the preheating scales with the square root of the heat transfert coefficient ($\eta_{rec} \propto \sqrt{h_V}$) and is inversely proportional to the mass flow rate.

- the reaction zone is replaced by a jump condition similar to the one obtained for the fully adiabatic flame (thanks to scale separation). It provides the mass flow rate as

function of the preheating:

$$\frac{\dot{m}}{\rho_u S_L^0} \approx (1 + \alpha \eta_{\text{rec}}) \exp\left(\frac{1}{2} \frac{\beta \eta_{\text{rec}}}{1 + \alpha \eta_{\text{rec}}}\right) \quad (4.6)$$

where β is the Zeldovich number. Eq. (4.6) makes use of the thermal sensitivity of the reaction rate via the Arrhenius law: the preheating leads to an increase in burning velocity due to the increase in the temperature of the reaction zone.

Combining these two solutions leads to an implicit expression for \dot{m} whose resolution provides the value of \dot{m} consistent with both the non-reactive equations outside the reaction sheet and the local sensitivity of the flame to preheating. **P. A. Masset** showed in [85] that the following explicit formula is a good approximation of the recirculation-assisted speedup observed in porous media combustion :

$$\frac{\dot{m}}{\rho_u S_L^0} \approx 1 + \frac{\beta \sqrt{h_V(1-\epsilon)\lambda_s}}{2 \rho_u S_L^0 \epsilon c_{p_g}} \quad (4.7)$$

4.1.2.3 Porous media combustion: A Lewis-changing system

Substituting the heat exchange term $h_V(T_g - T_s)$ in the gas temperature equation in Eq. (4.1), we get:

$$\dot{m} c_{p_g} \partial_x T_g - \partial_x \left[\left(\lambda_g + \frac{1-\epsilon}{\epsilon} \lambda_s \frac{\partial T_s}{\partial T_g} \right) \partial_x T_g \right] + \sum_k c_{p_g,k} J_k \partial_x T_g + \sum_k h_k^0 \dot{\omega}_k = 0. \quad (4.8)$$

It is equivalent to a gaseous model of effective thermal conductivity:

$$\lambda_g^{\text{eff}} = \lambda_g + \frac{1-\epsilon}{\epsilon} \lambda_s \frac{\partial \theta_s}{\partial \theta_g}. \quad (4.9)$$

Interphase coupling can therefore be interpreted in terms of additional thermal diffusion, proportional to the ratio of solid and temperature gradients $\partial \theta_s / \partial \theta_g$. Since the species equation is not impacted directly by the heat transfer, this change in gas thermal diffusion translates into a change of Lewis number of the species, and specifically the fuel:

$$\frac{\text{Le}_F^{\text{eff}}}{\text{Le}_F} = 1 + \frac{(1-\epsilon)\lambda_s}{\epsilon \lambda_g} \frac{\partial \theta_s}{\partial \theta_g} \quad (4.10)$$

which directly relates the effective Lewis number to the interphase out-of-equilibrium parameter $\partial \theta_s / \partial \theta_g$. This effect of porous media combustion on the flame structure can be viewed directly in the space (Υ_F, θ_g) , in which only unity-Lewis number flames present straight lines (the base-line case correspond to a methane/air flame at $\phi = 0.5$). This is shown in Fig. 4.3. T

- in the decoupled regime, the flame operates as if embedded in an isothermal porous medium as observed in Figure 4.2(b) and (f), therefore $\partial \theta_s / \partial \theta_g \approx 0$ and interphase

out-of-equilibrium has no effect on the structure of the flame front: $Le_F^{\text{eff}} \approx Le_F$. This is essentially what is observed in Fig. 4.3, where the curve obtained in the decoupled regime corresponds to a simple translation of its adiabatic counterpart in temperature space due to preheating, essentially conserving the structure.

- The changing-Lewis property of porous media combustion is highlighted in Fig. 4.3 as we move away from the decoupled regime. In the hyperdiffusive regime, $\theta_s \sim \theta_g$ thus $\partial\theta_s/\partial\theta_g \sim 1$ as highlighted in Figure 4.2(d) and (h): the change in Lewis number harmonizes spatially, and the equations boil down to an adiabatic laminar free-flame of increased thermal conductivity $\lambda_g + (1 - \epsilon)\lambda_s/\epsilon$ and increased species Lewis number: $Le_F^{\text{eff}} \approx Le_F(1 + (1 - \epsilon)\lambda_s/(\epsilon\lambda_g))$. This equivalent flame, named Limit Hyperdiffusive Free-Flame (LHFF), is also shown in Fig. 4.3, where its structure is very close to the one obtained at the hyperdiffusive regime.

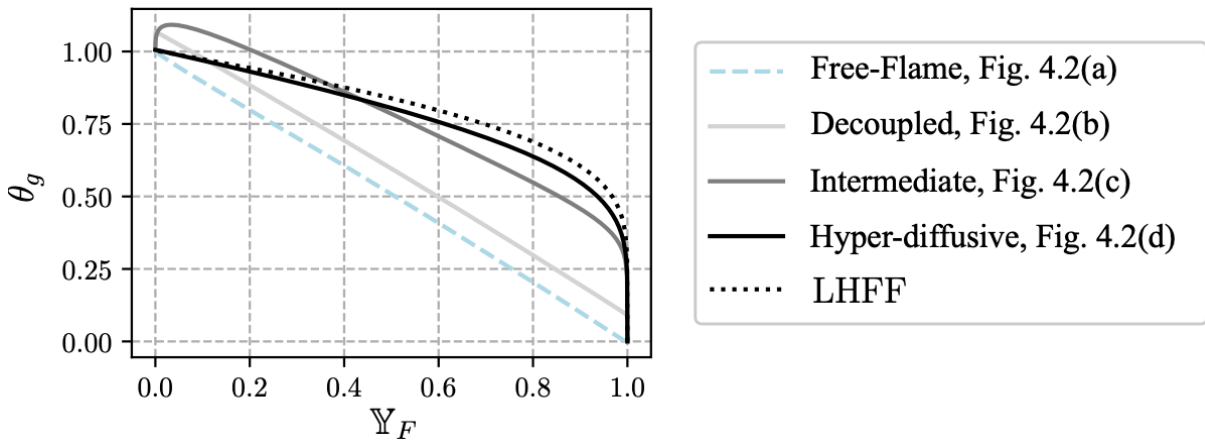


Figure 4.3: (Y_F, θ_g) representation of the flames in Fig 4.2. Adapted from [84].

The impact of mixture composition, fuel, chemistry description as well as finite thickness porous media was studied thoroughly in the PhD of **P. A. Masset** [84, 85] using this combination of theoretical derivations and numerical simulations. A proposition of regime classification based on non-dimensional controlling parameters was also discussed in [84].

4.1.3 3D simulations of flame stabilization in porous media

The work performed in the context of the PhD thesis of **P. A. Masset** allowed to investigate the governing principles of porous media combustion as well as pinpoint its driving parameters thanks to the volume averaging method. The main problem of the approach is that the whole geometrical complexity of porous matrices, for which an example is provided in Fig. 4.4, is reduced to a global porosity parameter. In the averaging process, the details of the flow at the pore scale are lost and the effects of flame wrinkling are not yet fully taken into account in volume averaged models. In the PhD thesis of **F. Muller**, we performed 3D Direct Pore-Level Simulations (DPLS) taken into account a realistic porous geometry obtained from an X-ray tomography of a ceramic foam. The porous

matrix is displayed in Fig. 4.4(left). An idea of the evolution of the porosity and surface density through the porous matrix is also provided in Fig. 4.4(right). Locus of minima in the porosity can clearly be observed in the 1D porosity profile which questions the use of a global porosity value in volume averaged equations.

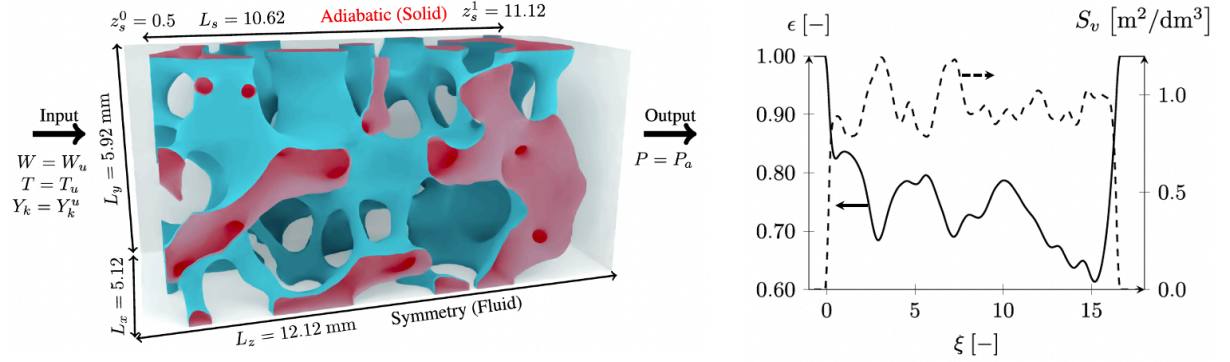


Figure 4.4: (left) Computational domain with the fluid-solid interface in blue and the solid boundary conditions in red. (right) Porosity ϵ and specific area S_v versus the normalised axial position $\xi = (z - z_s^0)/\delta_L^0$. Adapted from [88].

Performing 3D DPLS remains a challenging computational task because of the complexity of the geometry and the meshing constraints it entails. In the PhD of **F. Muller** we had to restrict the size of the porous matrix to simulate and the overall lengths of the computation domain are $L_x, L_y, L_z = 5.12, 5.92, 12.12$ mm. The simulation are not statistically independent of the geometry, however the size of the domain is sufficient to investigate the fundamental mechanisms of flame stabilization in porous media. The characteristic cell size was set to the small value of $20 \mu\text{m}$ for a total of 32 grid points in the flame front and 40 grid points per pore. Moreover, these simulations are only meaningful when the both the solid and gaseous phases are coupled, which required: (1) to mesh both the solid and the gas phases for a total of approximately 10 and 30 million cells in the solid and gaseous phases respectively, while the time step is around 1 ns; (2) to perform coupled simulations where the multispecies, reactive and compressible Navier-Stokes equations are solved in the gas phase and the energy equation is solved in the solid phase.

In [88] we restricted the analysis to the case of a premixed hydrogen-air flame with an equivalence ratio of $\phi = 0.3$ injected at a fixed temperature $T_u = 500$ K and constant inlet velocity W_u . The reference flame speed and flame thickness of the adiabatic planar free-flame at these conditions are $s_L^0 = 0.42$ m/s and $\delta_l^0 = 0.6$ mm. A key parameter that was varied in this study is the inlet velocity W_u to showcase the burning velocity enhancement that can be achieved due to heat recirculation and quantify the range of inlet velocity under which flame stabilization is possible. Stabilized flame solutions were obtained for the range $W_u \in [3, 6]$ m/s, which correspond to values with respect to the adiabatic free flame reference of $u \equiv W_u/s_L^0 \in [7, 14]$, highlighting the large enhancement of burning velocity.

Fig. 4.5(right) shows the tip of the flame surface $c = 1 - Y_{H_2} = 0.05$ obtained for the cases $u = 7$ and $u = 14$. A strongly corrugated flame surface is clearly visible, which seems

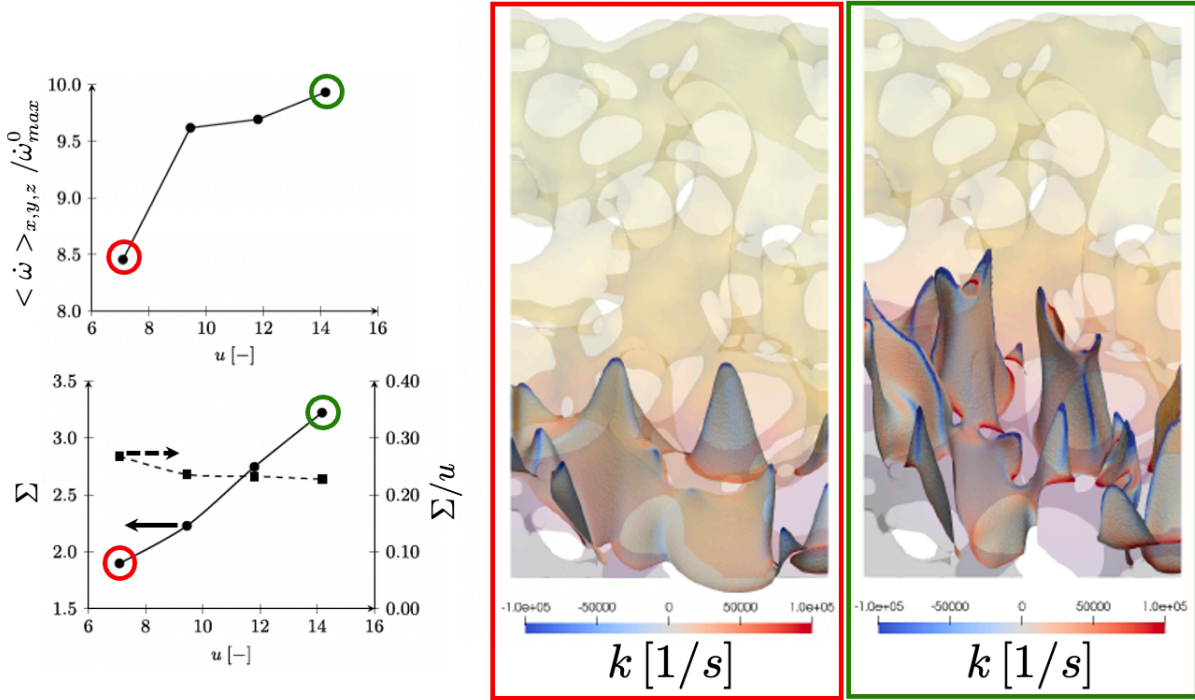


Figure 4.5: (left) Evolution of the normalized average heat release rate $\langle \dot{\omega} \rangle_{x,y,z} / \dot{\omega}_{max}^0$, normalized flame surface $\Sigma = \langle \|\nabla C\| \rangle_{x,y,z} / (L_x L_y)$ and ratio of normalized flame surface to normalized inlet velocity Σ/u with the reduced inlet velocity $u = W_u/s_L^0$. (right) Isosurface $c = 1 - Y_{H_2} = 0.05$ colored by the stretch rate k for two cases: $u = 7$ and $u = 14$. $\dot{\omega}_{max}^0$ corresponds to the peak heat release rate in the equivalent 1D planar free-flame. Adapted from [88].

to be enhanced when increasing the inlet velocity. For both values of u however, parts of the flame appear to be anchored at the leading side of the porous matrix. The drastic increase of flame surface Σ with inlet velocity (and the corresponding increase in the global heat release rate $\langle \dot{\omega} \rangle_{x,y,z} / \dot{\omega}_{max}^0$) is quantified in Fig. 4.5(left) and seems to follow a quasi-linear trend which is confirmed by the plateau observed for Σ/u : $\Sigma \approx 0.22u$. Fig. 4.6 allows to better grasp the complex flow field taking place inside the pores of the porous matrix. It also emphasizes two important features of porous matrices: (i) the strong anchoring mechanism that can take place, which leads to parts of the flame remaining attached to the leading solid structures (struts s_1 to s_4) even though the inlet velocity has been double; (ii) the strong elongation of the flame with increasing inlet velocity with chemical reaction taking place further downstream in high-porosity regions whenever the flame finds a suitable path through the matrix. These two features are out of grasp for volume averaging methods.

Finally, the impact of inlet velocity on the axial profiles of surface-average and surface extrema of gas temperature are displayed in Fig. 4.7. It highlights two important features not captured by volume averaging methods: (i) the surface average profile do not show any super-adiabaticity, contrary to the predictions of volume averaging methods; (ii) increasing the inlet velocity leads to a remarkable elongation of the flame front (pushing

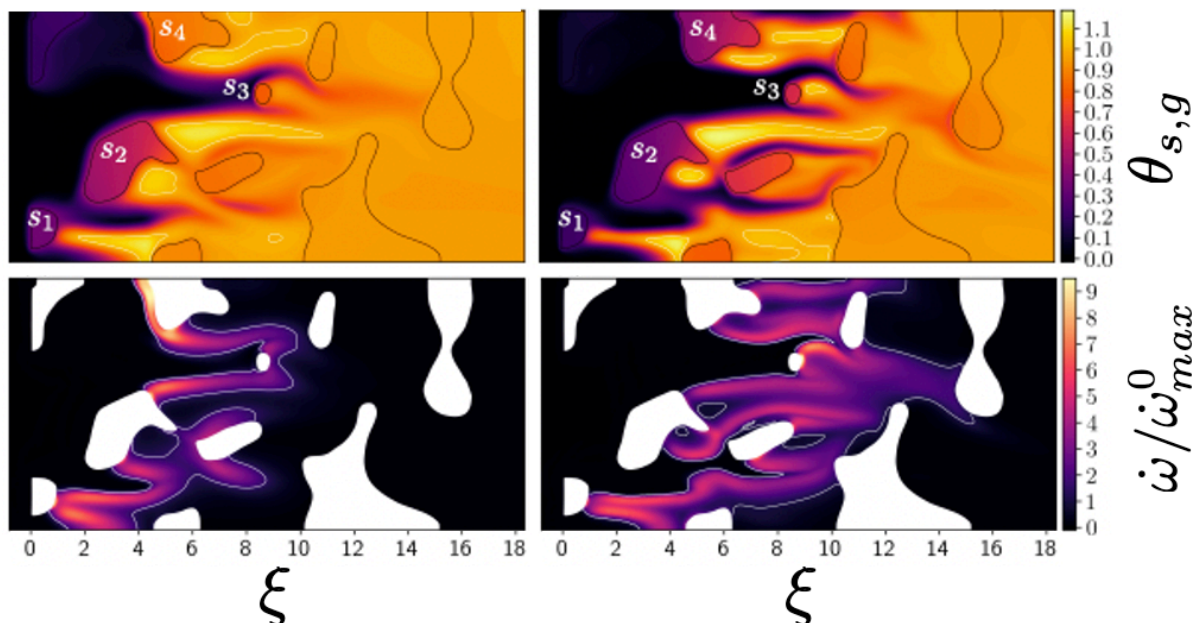


Figure 4.6: 2D cuts showing the normalized solid temperature θ_s , gas temperature θ_g and heat release rate $\dot{\omega}/\dot{\omega}_{max}^0$ for $u = 7$ (left) and $u = 14$ (right). $\dot{\omega}_{max}^0$ corresponds to the peak heat release rate in the equivalent 1D planar free-flame. Adapted from [88].

the surface-minima profile downstream and broadening the profile of surface averaged heat release rate) with parts of the flame remaining strongly attached to the leading parts of the porous matrix (surface-maximum profiles quasi-independent on the inlet velocity). This anchoring mechanism is responsible for the stabilization of flames in porous media at high inlet velocity, avoiding blow-off.

4.1.4 Outlook and future work

Both Volume Averaging Methods (VAM) and 3D DPLS were used to unveil the driving mechanisms of porous media combustion. The following conclusions can be drawn:

- many features observed in DPLS and playing a major role in the burning enhancement and flame stabilization in porous burners are completely absent from VA modeling. The longitudinal distribution of the flame fronts along the burner axis makes the spatially-averaged profiles much broader than in the VAM predictions, which model a unique flame front.
- not discussed here, but hydrodynamic dispersion is found to not drive directly the burning rate of the flames at pore scale in the DPLS, contrary to the VAM where the increase in diffusivities systematically enhances flame speeds.

Attempts at solving these problems were made by **P. A. Masset** in [89] by providing a new closure for the reaction rates in VAM based on a flamelet assumption and pore-scale observation from 3D DPLS. It accounts for flame wrinkling and eliminates the unwanted

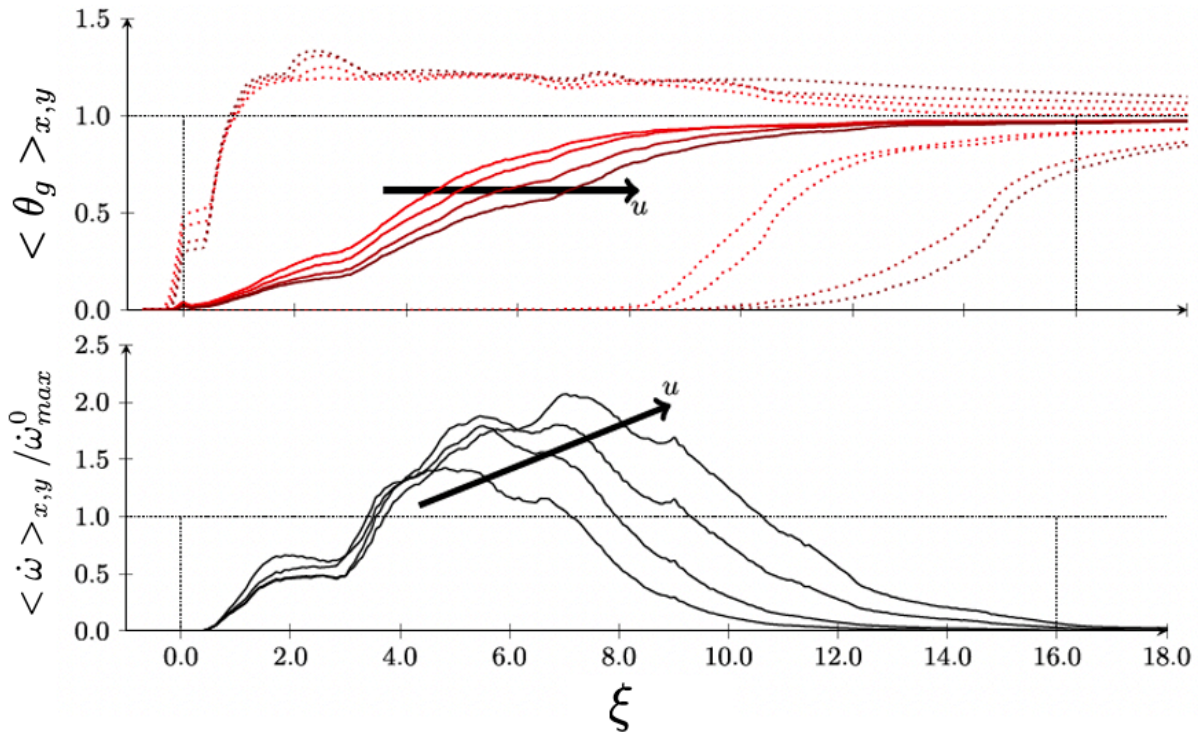


Figure 4.7: Surface averaged profiles of gas temperature θ_g and normalized heat release rate $\dot{\omega} / \dot{\omega}_{max}^0$ for increasing values of inlet velocity u : $u = 7, 9.5, 12, 14$. $\dot{\omega}_{max}^0$ corresponds to the peak heat release rate in the equivalent 1D planar free-flame. Dashed lines correspond to the axial profile of surface-maximum and minimum gas temperature. Adapted from [88].

effect of hydrodynamic dispersion on burning rate. Direct comparisons between 3D DPLS and the modified VAM results was performed by **P. A. Masset** in [89] by also feeding the VAM equations with effective properties estimated directly from 3D DPLS. The performance of the proposed model remains unsatisfactory however. Possible future work directions include the consideration of unsteady cases, different geometries/fuels, and the inclusion of radiation in both the DPLS and VAM, a mechanism of crucial importance in porous burners.

4.2 Reaction waves in Pressure Gain Combustion (PGC) systems

4.2.1 Context and funding

The work presented in this part of the manuscript was performed within the INSPIRE (INSpiring Pressure gain combustion Integration, Research, and Education) project. INSPIRE is a Marie Skłodowska-Curie Innovative Training Network (ITN), a consortium of universities, research laboratories and industries, aiming at studying both experimentally

and numerically the performance of Pressure Gain Combustion (PGC) solutions.

PGC corresponds to a radical change in the thermodynamic cycle followed in classical engines where the combustion part, a conventionally isobaric process (Brayton Cycle), is proposed to occur with a large increase in pressure by constraining the gas expansion by heat release. This can be done by replacing the constant pressure combustion by: (i) a Constant Volume Combustion (CVC), or (ii) detonative combustion either via Rotating Detonation Combustion (RDC) or Pulsed Detonation Combustion (PDC). By doing so, PGC theoretically enhances work extraction by expansion to the initial pressure, hence is supposed to theoretically increase the thermodynamic efficiency of the engine by 15 – 30% compared to conventional engines.

We focused on the challenges facing the high-fidelity simulations of CVCs and RDCs using LES. The theoretical motivation behind PGC systems, discussed just above, is purely steady and in contrast with the intrinsically unsteady nature of these devices. Both systems, CVC and RDC, exploit propagating reactive waves using an unsteady propagating deflagration front and a continuously rotating detonation front respectively. This unsteady aspect is of crucial importance for the performance analysis of PGC systems and for their integration in full engines with other components like compressor and turbine. Crucial modeling challenges are associated to the unsteady nature of CVC and RDC and are at the center of the PhD theses of **N. Detomaso** and **P. Stempf** respectively. LES has taken an increasingly significant role in these fields, but still requires advanced physical models to ensure predictive computations over successive operating cycles. The objective, during the INSPIRE project, was to extend the state of the art LES methods to deal with the complexities related to the reactive flow inside CVCs and RDCs.

4.2.2 Modelling challenges in the LES of CVC

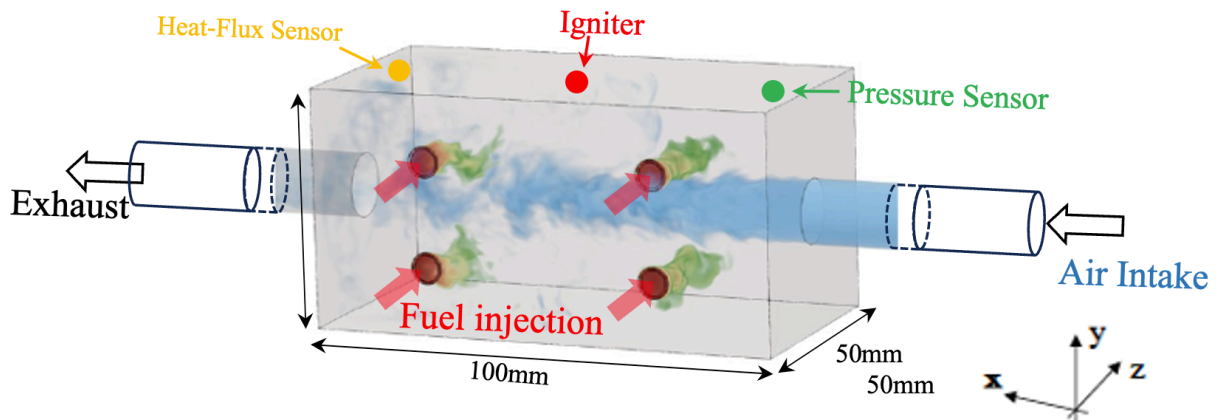


Figure 4.8: Schematic of the CV2 computation domain (Exhaust and intake pipe are not shown in their entire lengths).

During the PhD of **N. Detomaso**, we focused our attention on the CV2 test rig operated at Pprime laboratory (Poitiers, France) consisting of cyclic Pistonless CVC processes for air-breathing gas turbines applications. The configuration is simple and

illustrated in Fig. 4.8. Fig. 4.9 highlights the typical phases through which the combustion chamber goes (using the pressure signal averaged over several cycles and recorded with the pressure sensor shown in Fig. 4.8).

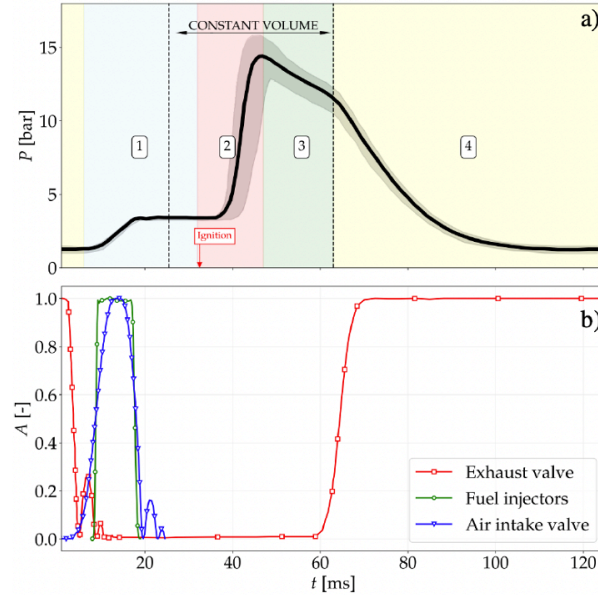


Figure 4.9: (a) Pressure signal averaged over seven sequence of 12 cycles. Colors represent the different phases repeated for each cycle. b) Section law of the admission valve, the fuel (C_3H_8 in CV2) injectors and the exhaust valve.

- (Admission phase) At the beginning of each cycle, Fuel (C_3H_8 in CV2) and Air admission valves are open to feed the combustion chamber with a reactive mixture. The associates pipes are displayed in Fig. 4.8. During the admission phase, highlighted in blue in Fig. 4.9, pressure increases in the combustion chamber and stabilizes to a plateau when C_3H_8 and Air admission are stopped.
- (Isochoric combustion phase) This phase, highlighted in red in Fig. 4.9, is initiated by igniting the reactive mixture obtained after the admission phase. The position of the igniter is illustrated in Fig. 4.8. This phase is characterized by a strong increase in pressure associated to the combustion in constant volume conditions.
- (Isochoric cooling phase) As soon as all the reactive mixture is burned, the pressure increase in the chamber is no longer assisted by combustion and an isochoric cooling phase is triggered where combustion products transfer heat to the structure of the combustion chamber.
- (Exhaust phase) A sharper decrease in pressure happens when the exhaust valves are opened to suck the combustion products left inside the combustion chamber. A relax to atmospheric pressure is then observed.

This sequence of phases is repeated for each cycle and has to be accurately reproduced in the LES to correctly predict of the pressure dynamics inside the combustion chamber.

Focus was paid, in the PhD of N. Detomaso, to develop a methodology able to solve the many challenges facing the LES of CVC. The major constituting bricks of this methodology, denoted by $M1 - M3$, are discussed in the following:

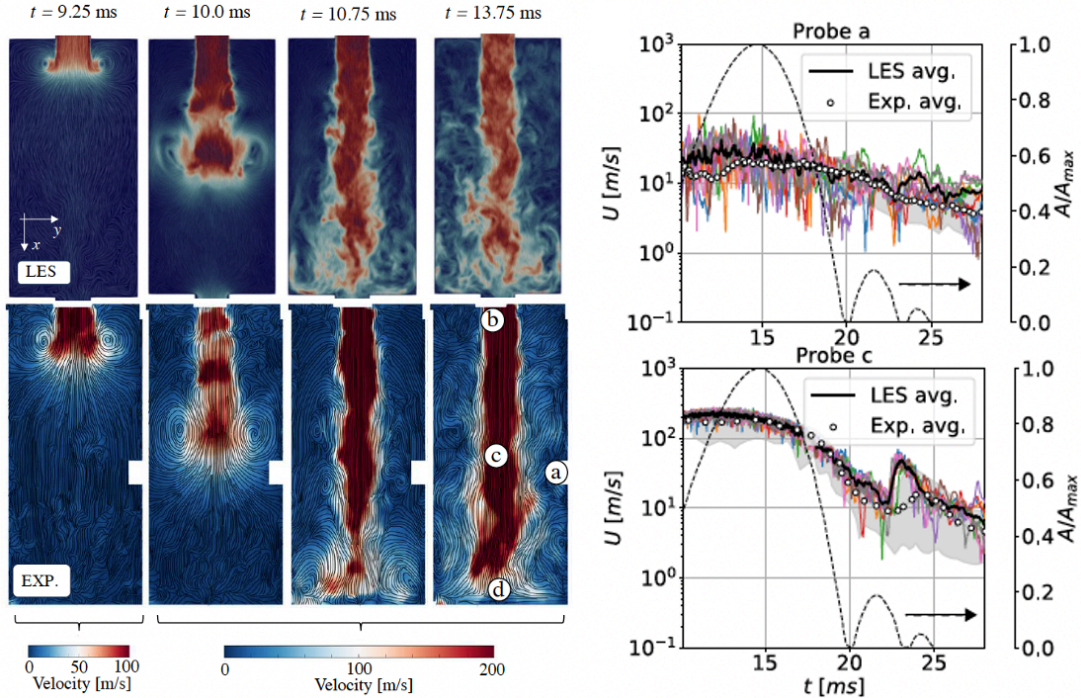


Figure 4.10: Comparison of the unsteady flow obtained experimentally (with PIV measurements) and with LES during Air intake. (left) Velocity fields. (right) Velocity magnitude measured at the ignition point (a) and at the middle point of the chamber (c). White dots represent the experimental ensemble average and the black line the numerical average. Black dashed line corresponds to the valve section law of the air stream. Adapted from [90].

4.2.2.1 (M1) Nozzle-based boundary condition for intake and exhaust

Pistonless CVCs, such as CV2, involve complex intake and exhaust phases, operated using valves. The section law for the Fuel, air and exhaust valves is shown in Fig. 4.9(b) and must be reproduced accurately in LES. Instead of simulating these processes involving moving bodies like in [91], which would have required a considerable computational cost, we assumed intake and exhaust valves (in CV2) to behave as convergent-divergent nozzles and replaced these valves with inlet and outlet boundary conditions [92]. In this modelling process, the flow passage, generated in time by the closure elements of valves, is assumed acting like the minimum section of a nozzle, where $A_t = Av(t)$ (where A_v is the valve section) is a function of time and corresponds to the section law characterizing the intake and exhaust valve systems (see Fig. 4.9). Although, this may be viewed as a crude assumption, its validity strengthens when valves are characterized by passage sections that regulate the streams, without any mechanical element that interact directly with the flow,

imposing a specific topology. The appropriate physical variables (e.g. u , T , Y_k and P) are computed during the simulation run-time following the section law imposed by the experiments and imposed using a NSCBC formalism.

The validation of this boundary condition is shown in Fig. 4.10 where the unsteady flow during Air intake obtained with LES is compared to experiments. The Nozzle-based boundary conditions are shown to accurately take into account the opening of the valve in Fig. 4.10(left) for $t < 15\text{ ms}$. Even though some differences can be observed in Fig. 4.10(right) between LES and experiments for $t > 22\text{ ms}$, when the valve exhibits partial openings, the intake phase is fairly reproduced by the LES with considerable reduction in computational cost and simulation complexity compared to strategies based on fully taking into account the moving bodies in LES, like in [91].

4.2.2.2 (M2) Reduced kinetic modelling for flames diluted with Residual Burnt Gases (RBG)

In piston-less CVCs, no mechanical piston expels the burnt products at the end of each cycle, and a non-negligible amount of them remain in the chamber and mix with air and fuel re-injected during the subsequent admission phase. This means that both turbulent combustion models and chemical schemes have to account for the impact of composition (fuel/air) and dilution by burnt gases on combustion in order to correctly predict flame propagation speed and its impact on pressure build-up during each cycle. In the PhD of **N. Detomaso**, a computationally effective 2-step chemical scheme was used and extended to account for the wide range of pressure, temperature and RBG dilution encountered during the combustion phase of the CVC cycle. The methodology is based on the pre-exponential adjustment of the rates of the 2-step scheme, similarly to [93], assuming the exact composition of RBG gases is known.

To fully characterize the composition of RBG-diluted C_3H_8 /air mixtures at the combustion phase of cycle n , it is shown in [90] that two parameters are sufficient:

$$\phi_r \equiv \frac{sY_{\text{C}_3\text{H}_8}^n}{Y_{\text{O}_2}^n} \quad \text{and} \quad \phi_{bg} \equiv s \frac{Y_{\text{C}_3\text{H}_8}^{*,n-1}}{Y_{\text{O}_2}^n + Y_{\text{O}_2}^{*,n-1}} \quad (4.11)$$

where s is the mass stoichiometric ratio ($s = 3.63$ for propane/air mixtures). ϕ_r measures the local equivalence ratio obtained by mixing the available fuel and Air at the beginning of the combustion phase of each cycle n . ϕ_{bg} however measures the amount of RBG gases, *i.e.* CO_2 and H_2O , diluting the current mixture and directly linked to the amount of fuel $Y_{\text{C}_3\text{H}_8}^{*,n-1}$ and oxydizer $Y_{\text{O}_2}^{*,n-1}$ burnt from cycle 0 to cycle $n - 1$ to produce the desired RBG dilution. The pre-exponential correction proposed in [90] is a function of these two mixture-characterizing parameters ϕ_r and ϕ_{bg} . When $\phi_{bg} = 0$, ϕ_r corresponds to the classical definition of equivalence ratio and the correction is not needed. When $\phi_{bg} > 0$, RBG dilution affects C_3H_8 /air flame properties by thermal inhibition (reduction in flame temperature and the subsequent reduction of flame speed by thermal sensitivity of the reaction rate). Fig. 4.11 shows that this effect is well captured by the 2-step scheme at

reduced computational cost compared to detailed chemistry.

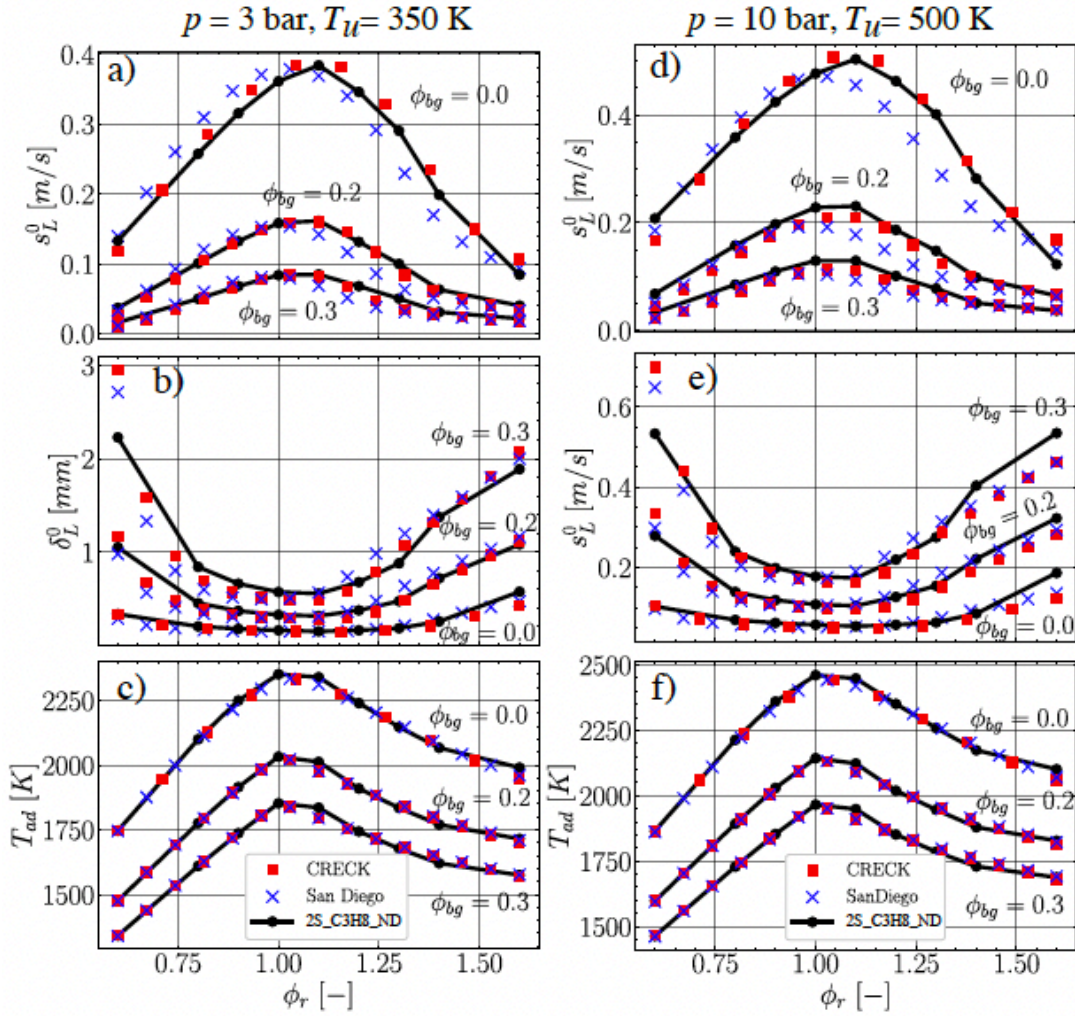


Figure 4.11: Validation of the 2-step chemical scheme developed by [90] for a large range of C_3H_8 /air mixtures at equivalence ratio ϕ_r with three levels of RGB dilution ϕ_{bg} . Adapted from [90].

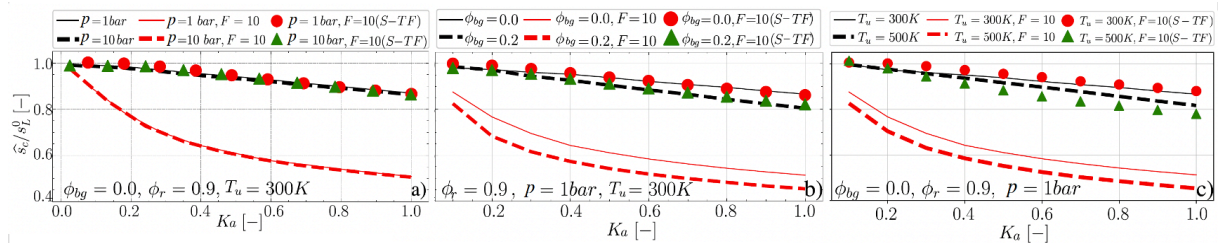


Figure 4.12: TF vs S-TF model in 1D premixed counterflow flames: flame speed vs Karlovitz number $Ka = k\delta_L^0/s_L^0$. a) effect of pressure; b) effect of RGB dilution; c) effect of fresh gases temperature.

4.2.2.3 (M3) S-TF for the accurate prediction of flame propagation in turbulent flows

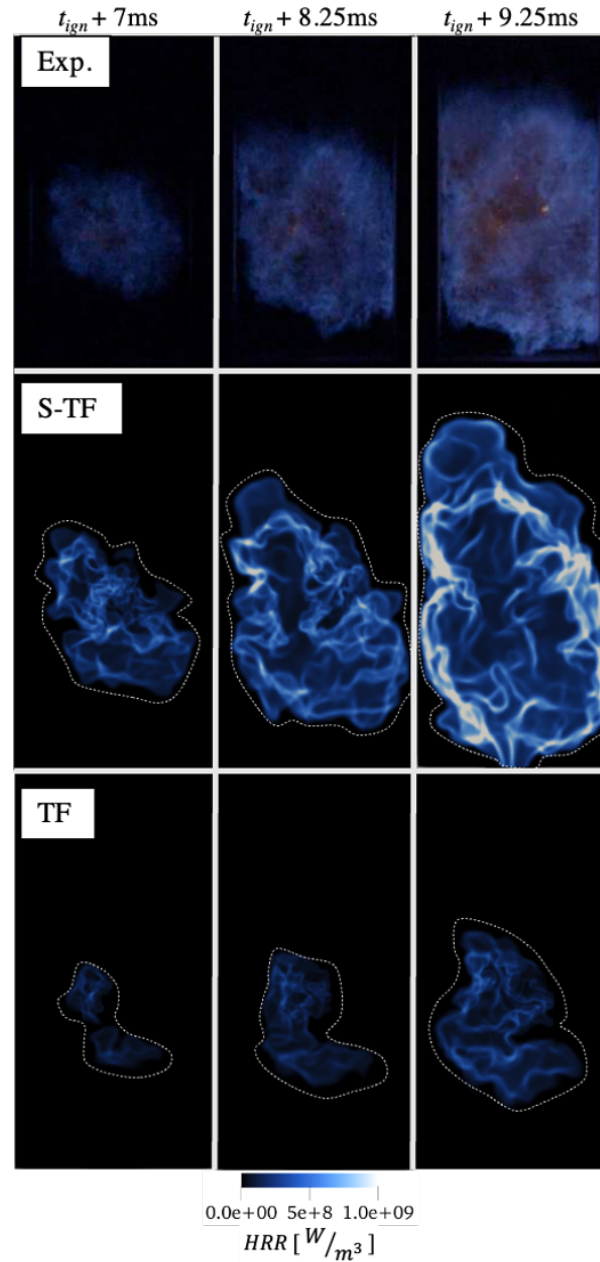


Figure 4.13: Experimental flame shape captured with the chemiluminescence technique compared with the heat release rate (HRR) signal computed with the LES simulation. White dashed line is used to highlight the flame. Adapted from [90].

The combustion phase in a CVC cycle is characterized by the propagation of a deflagration wave in a turbulent flow generated by the admission phase. Fig. 4.13 illustrates the evolution of the flame kernel in the chamber in both experiments and LES. It shows that as soon as the flame kernel is formed, the turbulent flow strongly affects its propagation leading to a markedly corrugated flame. Flame propagation in CVCs shares the similar

problems encountered in the LES of outwardly propagating spherical deflagrations discussed in chapter 2.1 and more specifically regarding the amplification of stretch effects by the flame thickening (TF) approach. Fig. 4.12 confirms that the TF approach also amplified stretch effects for C_3H_8 /air flames for all operating conditions considered, although here C_3H_8 /air are negatively influenced by stretch ($Le_{\text{eff}} > 1$). The application of the S-TF model Eq. 2.14, introduced in Section 2.1.4 for hydrogen applications, also solves the problem of stretch with TF here and even more efficiently than for hydrogen flames because of the relatively low stretch sensitivity of C_3H_8 /air flames compared to H_2 /air flames. The S-TF model was also extended in the PhD of **N. Detomaso** to account for pressure, temperature and RGB dilution variations as highlighted in Fig. 4.12. Its application to the CV2 test case in Fig. 4.13 confirms that the S-TF eliminates the strong stretch-based burning velocity-mitigating effect of TF and predicts a fairly accurate flame dynamics in the CVC.

Finally, Fig. 4.14 compares the pressure evolution inside the chamber obtained with both TF and S-TF models. The pressure evolution predicted with the classical TF model falls outside the experimental envelope. It underestimates the rate of overpressure generation during the combustion phase and does not allow enough time for the isochoric cooling phase (see Fig. 4.4a) to take place. The S-TF, on the other hand, corrects these behaviors and provides an accurate depiction of the pressure evolution during the whole cycle. These differences can be further supported by comparing the evolution of the averaged fuel consumption rate, representative of the averaged consumption speed $\langle s_c \rangle$, with the global stretch experienced by the flame:

$$\langle \dot{\omega}_F \rangle = \frac{1}{V} \int_V \dot{\omega}_F dV \quad \text{and} \quad \langle k \rangle = \frac{1}{S_f} \frac{dS_f}{dt} \quad (4.12)$$

with S_f the area of an isosurface of 1500K. The result is shown in Fig. 4.14(b). As the flame kernel develops, the average stretch it experiences reduces, and for sufficiently small values of stretch, both S-TF and TF provide similar results. However, and especially for the early stages of kernel development, the S-TF model corrects the amplification of the flame sensitivity to stretch observed with TF, and predicts considerably higher flame consumption speeds (for the same value of $\langle k \rangle$). This effect enhances the pressure rise during combustion (higher dP/dt) as expected. Note that the point of maximum consumption speed coincides with the maximum of dP/dt (star symbols).

4.2.3 Outlook and futur work

All these fundamental contributions allowed to derive an efficient LES methodology able to accurately predict: (1) the propagation of stretched flames in turbulent, non-homogeneous flows with burnt gases dilution, a problem at the heart of the combustion phase of CVC cycles; and (2) the complex injection of fresh gases and exhaust of burnt gases characterizing the admission and exhaust phases at very low computational cost. This resulted in reliable and predictive LES of CVCs over repeated cycles, as shown in [90].

Possible work directions include transitioning to liquid fuels since gaseous injection

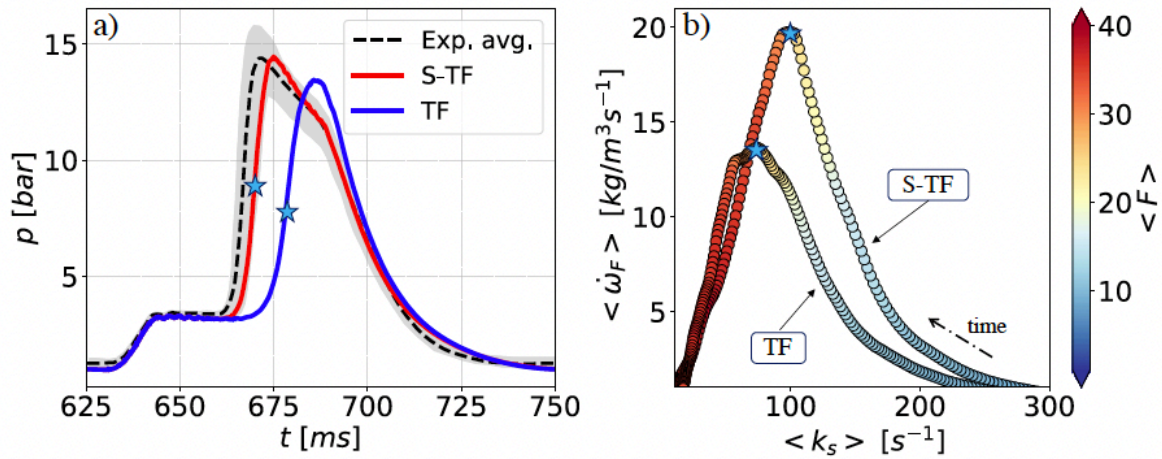


Figure 4.14: S-TF vs TF model over one cycle. a) Pressure signal b) Averaged fuel consumption rate as a function of the mean stretch. Locus of maximum pressure rise $(dP/dt)_{max}$ is indicated with the star-marker.

cannot allow the cyclic stability of autoignited cycles, since its vapor pressure limits the pressure drop in the fuel injection system. Liquid injection can be a reliable solution to stabilize the dynamics of consecutive auto-ignited cycles. However, this leads to numerical challenges in LES, which must be addressed in future work. Also worth mentioning is the importance of conjugate heat transfer in CVC systems during the isochoric cooling part, which should be subject of further research efforts.

4.2.4 Modelling challenges in the LES of RDC

Even though LES has established itself, over the past decades, as an indispensable tool for designing efficient combustion engines and unveiling the mechanisms governing their performance, including CVC systems as highlighted in Section 4.2.2, its applicability to Rotating Detonation Engines is not straightforward and suffers from the lack of a reference LES setup for reliable RDC simulations. The objective of the PhD of **P. Stremfpl** was to fill this gap by: (1) understanding the key ingredients controlling these simulations; and (2) identifying the crucial modeling issues that merits further investigations.

In the work of **P. Stremfpl** [95], we avoided relying on a 2D geometrical representation of the RDC chamber, often used in the literature to simplify the problem, and instead considered only simulations of a realistic full three-dimensional RDC tested at TU Berlin [94]. This includes the fuel (hydrogen here) and air plenums and their injection lines feeding a hollow-cylindrical combustion chamber. The LES of such complex RDC chamber gathers multiple difficulties, some which were the subject of particular attention:

- The geometrical meshing constraints of a full RDE configuration (chamber but also injection systems) can be difficult to satisfy in LES, especially for the TUB configuration where H_2 is injected through 100 small tubes resulting in 100 H_2 jets in cross-flow configuration with the main air stream (see Fig. 4.15(right)). For this

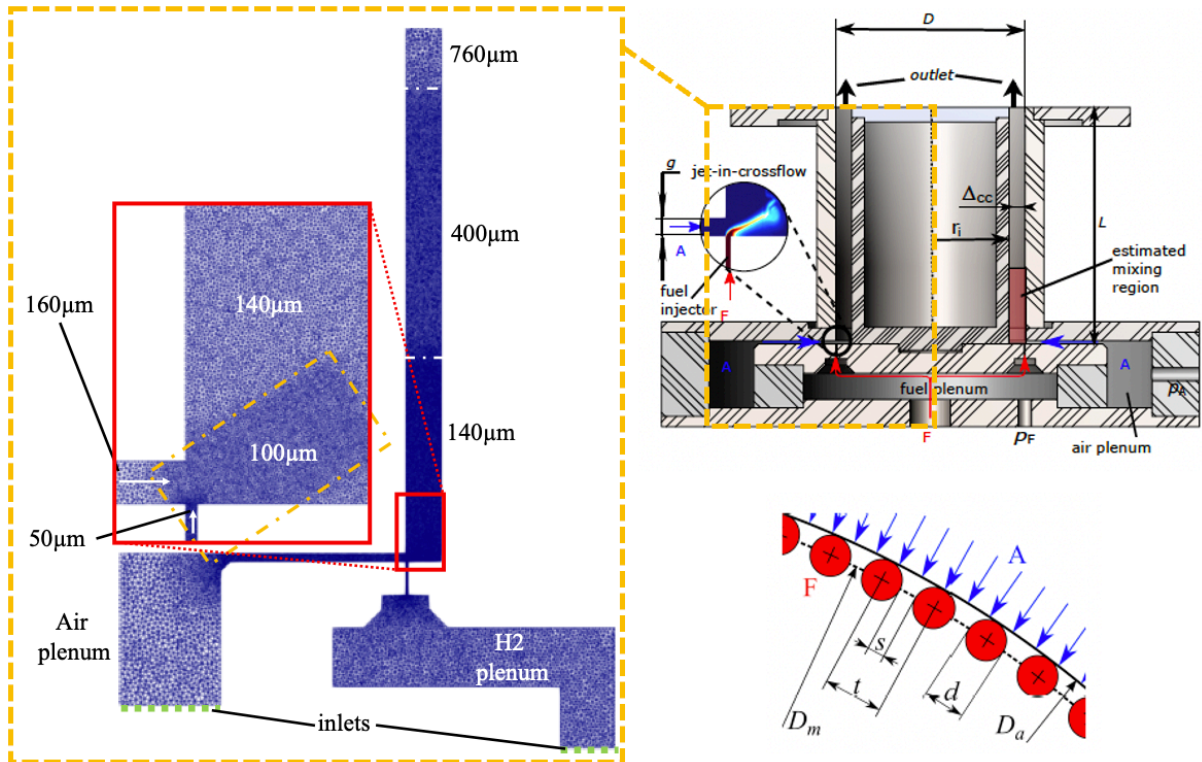


Figure 4.15: (left) Mesh strategy for the LES of a realistic full three-dimensional RDE tested at TU Berlin [94]. Number indicate the characteristic grid sizes used throughout the computation domain. (right) Corresponding cross section of the RDC of TU Berlin (A denotes air and F denotes fuel, *i.e.* H_2) and full illustration of the injection system.

reason, a dedicated meshing strategy (see Fig. 4.15(left)) was developed to properly resolve: (1) the flow in the feeding lines (at least 10 cells per H_2 tube diameter and air gap), (2) the jet in cross flow mixing at the bottom of the RDE chamber (with a resolution resulting from a dedicated mesh dependance study), and (3) the detonation wave passing though the reactive mixture.

- In a LES solver, the sub-grid scale viscosity ν_t controls the unresolved part of the mixing. The impact of SGS models, specifically developed for wall bounded flows WALE [96] and SIGMA [97], on the flow inside the RDC was assessed.
- The presence of multiple shock waves necessitates proper numerical treatments which consisted in the PhD thesis of **P. Stremfpl** of a localized artificial diffusivity [98], which activates only in regions of strong pressure gradients, leaving the remaining flow structures unaffected. A property of crucial importance to avoid impacting the mixing of fuel and oxydizer by numerical dissipation.
- A methodology was developed to design affordable reduced chemical schemes able to account for the global parameters of both detonations and deflagrations at relevant operating conditions. The contribution of the second mode (deflagration) is often overlooked when designing chemical schemes for RDC simulations despite its crucial

importance as stressed below.

- Igniting RDC chambers is a tedious task even for numerical simulations, and is often overlooked in the literature. A dedicated procedure to systematically ignite detonation waves inside RDE chambers was developed.

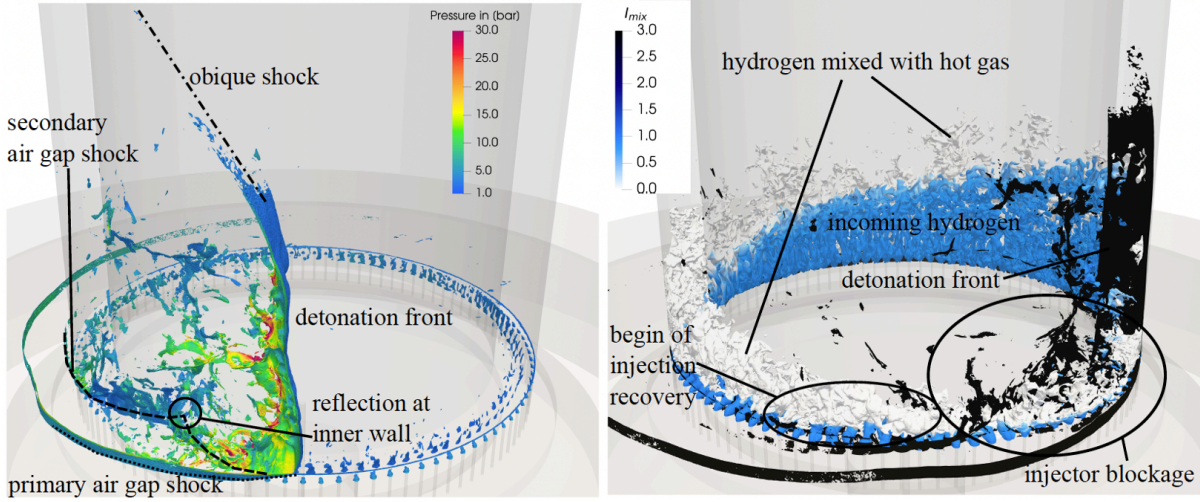


Figure 4.16: 3D visualization of the LES of a rotating detonation chamber. (Left) Isocontour of $|\nabla P|/P = 2000m^{-1}$ colored by static pressure showing the shock structures downstream the detonation wave responsible for the blockage of the air feeding gap; (Right) Isocontour of $|\nabla P|/P = 2000m^{-1}$ colored in black and isocontour of $Y_{H_2} = 0.0258$ colored by mixing indicator I_{mix} showing the fuel/air mixing layer forming after injection recovery.

The resulting setup allowed to capture the relevant structures controlling the performance of RDCs as shown in Fig. 4.16. Fig. 4.16(left) shows a complex detonation structure at the bottom of the combustion chamber as well as transverse shock waves propagating inside the air and H_2 feeding lines, thereby blocking momentarily the supply of reactive mixture inside the RDC chamber. Fig. 4.16(right) also shows the isocontour of fuel mass fraction $Y_{H_2} = 0.0258$ and highlights the blockage of H_2 just after the detonation passage. This isocontour is colored by a mixing indicator I_{mix} constructed based on the mixture fraction z :

$$I_{mix} = \frac{Y_{H_2} Y_{O_2}}{Y_{H_2}^m Y_{O_2}^m} = \frac{Y_{H_2} Y_{O_2}}{z_{nom} Y_{H_2}^0 Y_{O_2}^0 (1 - z_{nom})}, \quad (4.13)$$

where $z_{nom} \equiv \dot{m}_{H_2}/(\dot{m}_{H_2} + \dot{m}_{O_2}) = 0.0258$ in this case. I_{mix} is null whenever either or both H_2 and O_2 are null and is unity when both reactives are nominally mixed. Fig. 4.16(right) shows that when H_2 supply is recovered after the blockage, I_{mix} is still null at first and higher values are only observed a large distance after the detonation passage (half the circumference). This showcases the far-from ideal mixing characterizing the TUB setup where: (i) the air feeding line has more difficulty to recover from the blockage compared to H_2 ; and (ii) a significant amount of H_2 injected just after the blockage of H_2 lines is actually mixed with burnt gases from the previous cycle and hints at significant losses in the RDC of TUB.

Focus was then paid to two mixing-related problems of fundamental importance to the performance of RDCs :

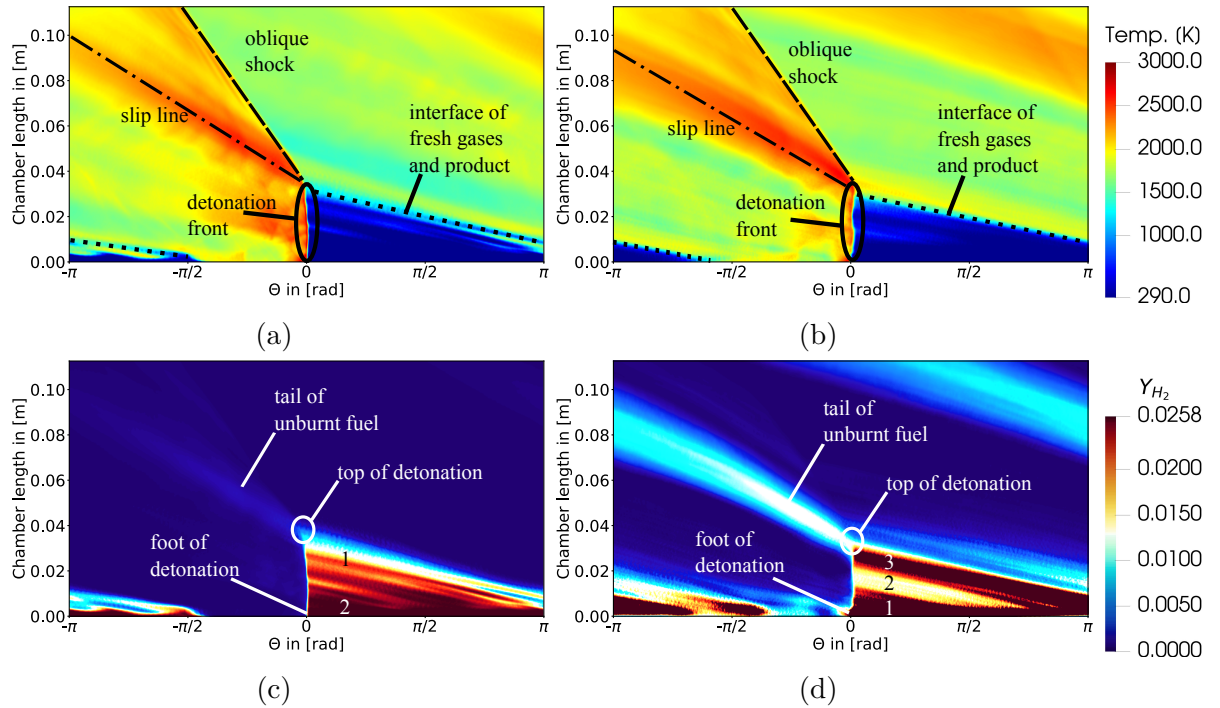


Figure 4.17: Comparaison between the premixed (a and c) and non-premixed (b and d) simulations in terms of phase averaged temperature and fuel mass fraction fields. The unwrapped field corresponds to a cut along 33% span width of the annulus.

4.2.4.1 Impact of mixing on detonation propagation

The LES simulations with the realistic injection system were systematically compared with their premixed counterpart (H_2 /air mixture at global equivalence ratio passing through all the feeding lines). The comparison is shown in Fig. 4.17. Simulations clearly show that the non-premixed case exhibits a relatively high amount of left-over fuel (see the tail downstream the detonation front in Fig. 4.17(d)) due to a combination of imperfect mixing and dilution by the combustion products of the previous cycles, thereby reducing the overall combustion efficiency $E = 1 - \dot{m}_{fuel}^{out}/\dot{m}_{fuel}^{in}$ of the RDE by 6 – 7%. Note that the premixed case is characterized by a combustion efficiency of 100%.

The far-from-ideal mixing observed in Fig. 4.17(d) can also be highlighted on phase-locked averaged cuts in front of the detonation, showing what the detonation front actually sees in front of it. This is shown in Fig. 4.18. The jet-in-crossflow configuration leads to a recirculation zone just above the air feeding gap where burnt products from the previous cycle are trapped and mixing of reactive material can not happen. Instead, mixing only occurs in the inner half of the combustion chamber which showcasing again the non-ideal conditions in which the detonation front propagates. This imperfect mixing leads to a reduced detonation speed compared to the premixed counterpart (reduction of almost 10% in these cases).

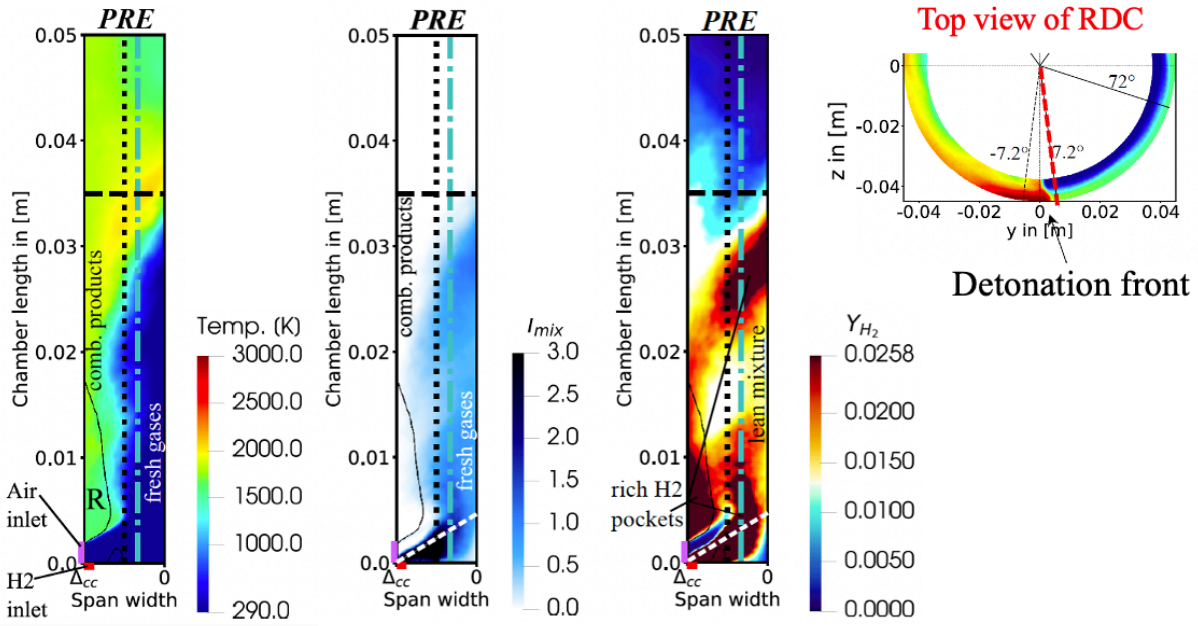


Figure 4.18: Phase locked averaged cuts in front of the detonation front (7.2° ahead). From left to right are shown temperature, mixing index and fuel mass fraction fields. A black iso contour at $u_z = 0$ reveals a re-circulation zone R in front of the detonation. The x -axis goes from 0 (at the inner wall) to $\Delta_{cc} = 7.6\text{mm}$ (at the outer wall).

4.2.4.2 Impact of parasitic deflagrative combustion on RDC efficiency

Fig. 4.16-4.18 show the existence of a large contact surface between reactive material and burnt gases that extend both in azimuthal and axial directions. This interaction between reactive mixture and burnt gases is a source of parasitic combustion where the mixture is not burnt in detonation mode, thereby constituting losses in thermodynamic efficiency. This is highlighted in Fig. 4.19 where parasitic combustion is observed for both premixed and non-premixed cases as a fundamental feature of RDC systems, but seems to be enhanced in the non-premixed case showcasing the non-ideal mixing observed in the injection system of the TUB test rig.

The amount of fuel burnt in deflagration and detonation modes was further scrutinized in all simulations. To do so, a local detonation index I_{det} was formulated [95] and used to compute the overall detonation efficiency of the engines E_{det} :

$$E_{det} = \frac{\int_V \dot{\omega}_k I_{det} dV}{\int_V \dot{\omega}_k dV} \quad (4.14)$$

The results are displayed in Fig. 4.20 and show that almost 20% of fuel in the premixed case burns in deflagration mode, a proportion that increases to 30 – 35% in the non-premixed cases. All this fuel burnt in deflagration mode does not participate in the pressure gain at the expense of the efficiency of the RDE. This result highlights the importance of including the deflagration burning as a constraint in the design of chemical schemes and LES combustion models, an issue that is almost completely overlooked in the literature.

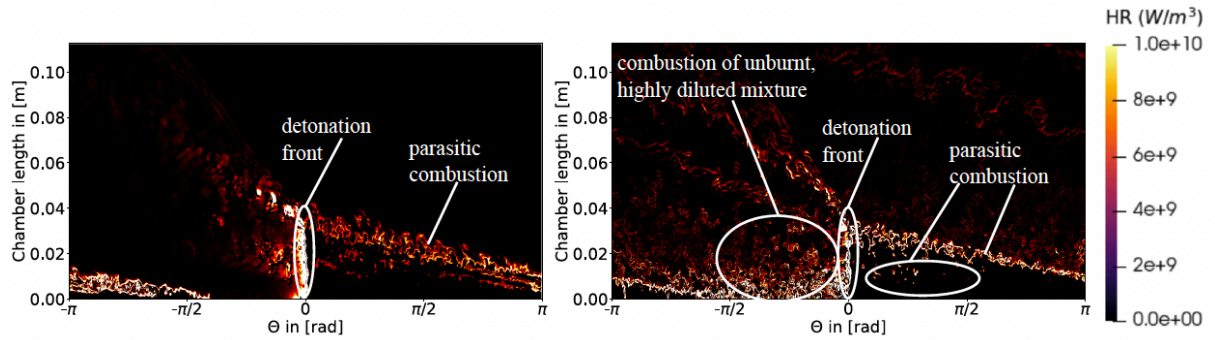


Figure 4.19: Instantaneous heat release rate fields in the premixed (left) and non-premixed (right) simulations. The unwrapped field corresponds to a cut along 33% span width of the annulus.

Finally, the work of **P. Stempf** stressed the strong impact of the rotating detonation wave and the burnt gases of previous cycles on the performance of the injection system, suggesting that cold flow simulations can only provide partial conclusions during the design process of the injection system and urging the community to include the reactive waves very early during the design process.

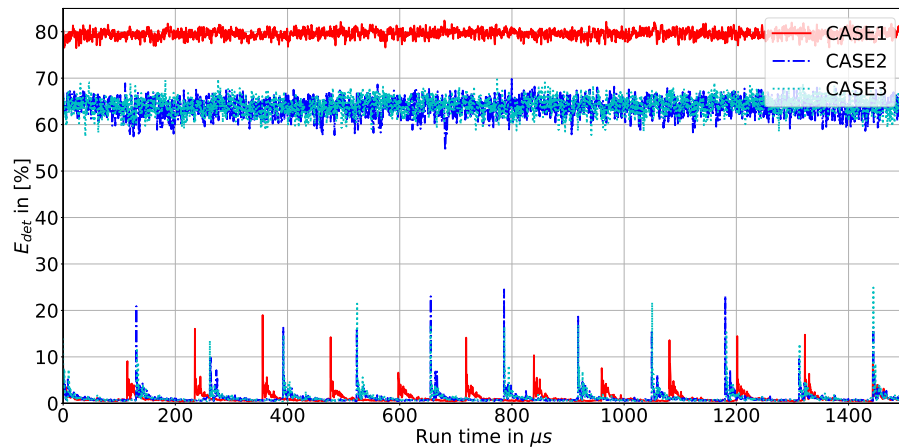


Figure 4.20: Detonation efficiency of the three investigated runs for 11 consecutive cycles. Bottom: probe pressure signals. CASE1 and CASE2 correspond to the premixed and non-premixed cases respectively. CASE3 differs from CASE2 by the LES subgrid-scale model used.

Outlook and futur work

My future research activities will continue to focus primarily on the modeling of reacting propagating waves, aiming at: (i) identifying the parameters controlling their propagation, and (ii) accurately reproducing their dynamics at relatively large scale using LES. I restrict this chapter to short-to-mid term research perspectives, *i.e.* ideas I would like to explore through projects that are either already funded or for which funding is currently actively sought.

5.1 Impact of mixture inhomogeneities on flame acceleration

Most of the existing research on flame acceleration predominantly addresses homogeneous mixture conditions. In most realistic safety scenarios, however, both ignition and flame propagation are expected to occur in mixtures characterized by some level of inhomogeneity, the nature and degree of which are strongly dependent on the scenario itself:

- Gas phase inhomogeneities: controlled by the time delay between gaseous leaks and ignition. The problem reduces to a gradient of fundamental flame properties along the flame surface, which can either enhance or mitigate flame acceleration compared to its homogeneous counterpart as shown in [45]. I have mentioned in Section 2.2, our first numerical investigations on the impact of stratification on flame acceleration both on the early stages of flame acceleration [38, 99] and in larger-scale scale obstructed channels [39]. These first attempts highlighted three specific problems that I would like to focus on in the near future: (1) the capacity of the TF-LES framework that we adopted in [39, 99] to accurately take into account the impact of local mixture inhomogeneities on flame burning must still be demonstrated; (2) not all mixture inhomogeneities can induce substantial enhancement of flame acceleration, and I would like to explore potential explicit criteria that mixture inhomogeneities must satisfy to actually matter, probably written in terms of gradient of fundamental burning velocity along local elements of flame surface; (3) all our investigations

[38, 99] highlight the fact that flame acceleration is influenced by the effective mixture inhomogeneity much less than it would have in the case of a frozen-in-time inhomogeneity, clarifying this aspect is needed to properly formalize point (2).

- Multi-phase inhomogeneities: for scenarios where the initial conditions are characterized by a combination of gas phase inhomogeneities as well as the presence of either solid or liquid phases. This is the case for explosions above liquid pools, as mentioned in Section 2.2.2 and/or in battery explosions where multi-component mixtures are liberated with the project of many micron-to-millimeter sized solid particles are also projected. The interaction of these liquid/solid particles with the flame can strongly influence flame acceleration. Here also, I would like to explore the capacity of the LES to properly take their presence into account by revisiting models already used at CERFACS to study multi-phase reactive flows for aeronautical applications.

These problems are of interest for CERFACS' industrial partners AIRBUS, TOTALEnergies, GRTGAz and AIRliquid, and will be explored with their support.

5.2 N-dimensional description of flame mitigation

The application of flame inhibition to propagating deflagration waves exhibits some challenges directly related to the transient and N-dimensional nature of the problem, which are out of the scope for the 1D description provided in Section 3.2. We have proposed a first attempt at modeling the inhibition of 2D self-propagating flames in [61], in which drastic simplifications were introduced to explore leading order effects and focus on potential counter-effects of flame inhibition that I intuited, anticipating the existence of conditions in which flame surface producing stratification effects could overcome the inhibition effects. I intend to pursue my research efforts in this direction, which will probably require to improve some modeling aspects used in [61], the main points of focus being: (i) the kinetics of thermal decomposition/evaporation of solid/liquid inhibitors, for which reliable parameters are unfortunately scarce in the literature; (ii) the intricate and strongly transient multi-phase inhibitor/flame interaction, which requires to accurately take into account the multi-shaped nature of some particles (powders) and the existence of locally high particle densities far from the dispersed condition under which classical point-source formalisms are formulated.

Given all these difficulties, we will stick to detailed investigations, leaving the research efforts on a potential LES formalism to a later stage. I am currently exploring options to fund this research.

5.3 LES strategy for capturing DDT

Despite decades of dedicated efforts, the investigation of DDT remains a challenging open problem characterized by the high disparity between the geometrical scales of the problem

and the constantly evolving physical scales of turbulent and reactive structures, all spanning a range of 5 to 7 orders of magnitude in space. However, the problem may be simplified by remarking that DDT, during its last critical stage, often takes the form of a shock-to-detonation transition. One can therefore bypass the flame acceleration phase and focus on its last critical stage SDT. This allows to focus on the role of shock wave dynamics during DDT and to drastically reduce the number of parameters controlling the problem. Even so, it is not clear whether SDT is triggered by a universal mechanism or by a variety of physical mechanisms depending on the range of its input parameters. We proposed to focus on this problem in the ANR project TRACKDEMO: a combined experimental and numerical investigation of the SDT problem in collaboration with the institut Pprime (Ashwin Chinnayya and Vincent Rodriguez). Focus will be paid to three specific modeling issues: (i) on-the-fly tracking of SDT precursors in detailed numerical simulations and associated criteria; (ii) investigation of potential conditions behind SDT failures and re-initiation; (iii) a formulation of a LES paradigm able to accurately reproduce the experimental database and DNS results produced in TRACKDEMO, and suitable for the numerical investigation of SDT/DDT in large scale and complex configurations. In (iii), different models are expected to be used depending on the local combustion regime (deflagration, detonation and auto-ignition). These regimes can even co-exist simultaneously during SDT, which calls for the implementation of methods capable of systematically identifying deflagration, detonation and auto-ignition zones, and automatically switching between different modeling formulations, chemistry descriptions, and resolution requirements when coupled to Adaptive Mesh Refinement (AMR) techniques. To do so, two options will be explored: (i) CSP based methods, of the type introduced in Section 2.3; and (ii) analytical criteria formulated in [100].

The project will effectively start in September 2024.

5.4 Plasma effects on hydrogen combustion

Another research axis that I would like to explore is related to the control of reaction waves via the use of non-equilibrium plasma which can produce atoms and radicals capable of enhancing the reactivity of combustible mixtures. The capacity of plasma discharges to reduced DDT run-up distances [101, 102] and influence detonation characteristics [103] has already been demonstrated in recent works. I would like to explore further these ideas anticipating two potential applications: (i) the control of detonation instabilities in rotating detonation chambers; (ii) forcing controlled ignition for active explosion mitigation systems (avoiding accumulation of reactive materials during leaks). Before focusing on the application itself, I will investigate the behavior of hydrogen flames under plasma discharges and electromagnetic conditioning, trying to understand the physical processes driving the interaction between hydrogen flames and electromagnetic fields and its impact on the chemical pathways of hydrogen combustion. Plasma effects of thermal nature (Non-equilibrium and equilibrium) and related to radical buildup will be delineated. Detailed simulations of the impact of plasma discharges on hydrogen combustion will be performed using the code AVBP-PAC, which is developed at CERFACS for plasma

assisted combustion.

This will be explored in the context of the funded MSCA ITN project ICHARUS in collaboration with imperial college (Andra Giusti). The project will effectively start in October 2024.

5.5 LES of Rotating Detonation Engines

The work of **P. Stremfpl**, summarized in Section 4.2.4, shows that LES can be used to understand the dynamics and stabilization mechanisms as well as overall performance of RDC systems. However, further research is needed to enhance the predictive capabilities of LES for RDC applications. Emphasis must be put (at least) on: (i) designing grid resolution criteria to accurately simulate curved detonations propagating in non-ideal conditions, criteria which are still missing today and can be coupled to adaptive mesh refinement techniques to impose these meshing constraints only in detonation regions; (ii) including the sensitivity of detonations to curvature ($D - \kappa$ curve [46]) in the design of reduced chemical schemes, which is completely overlooked in the simulations of RDCs today, despite its crucial importance; and (iii) perhaps most importantly, coupling the RDC chambers to a turbine stage to investigate how the flow obtained at the exhaust of the combustion chamber can be efficiently used for thrust generation (flow redirection, turbine design, ...).

These three aspects will be explored in the context of the MSCA ITN project H2POWRD which will start in October 2024.

Part II

Curriculum, Supervision and publications

Chapter 6

Narrative Curriculum Vitae, supervision and training

Sommaire

6.1 Narrative CV	83
6.2 Supervision and associated projects	84
6.3 Funded Projects (coordination, participation ...)	88

6.1 Narrative CV

In 2014, I received my engineering degree on applied mathematics at INSA Toulouse and a masters degree (Master de recherche) at Toulouse University III (Paul Sabatier). I then joined CERFACS for a PhD thesis focusing on the theoretical and numerical investigation of two explosion problems : (1) Heterogeneous chemical inhibition of deflagration waves, and (2) deflagration to detonation transition. During the following years, as a postdoctoral researcher, I extended my research activities to include heat-recirculation based combustion (SCIROCCO ERC project at IMFT) and pressure gain combustion (INSPIRE European project at CERFACS), while still contributing to the flame inhibition and DDT problems in collaboration with CERFACS.

In 2021, I had a break from research when I had the opportunity to join the hydrogen aircraft project at AIRBUS as a specialist in explosion safety. There I was responsible for the explosion prevention and mitigation strategies, a new topic for AIRBUS and strongly related to the introduction of hydrogen. This in-field engineering experience lasted one year. There I realized the serious limitations of current mitigation systems against fast-deflagrations and the crucial need for fundamental research on the subject. I decided then (November 2022) to join CERFACS as a permanent senior researcher and focus my research on the fundamental mechanisms controlling: (i) the propagation of flames and

their transition to fast-deflagrations and; (ii) the impact of various mitigation techniques on the propagation of reaction waves. Beyond safety applications, I still contribute to the modeling of propagating reaction waves in confined systems for propulsion applications: Constant-Volume-Combustion and Rotating detonation engines.

6.2 Supervision and associated projects

6.2.1 PhD students

Listed below are all the PhD students which I directly supervised or actively contributed in the supervision. Their associated funding project is also mentioned.

- **Pierre-Alexandre Masset [2019-2022]**
 - *Title:* Modelling challenges of stationary combustion in inert porous media
 - *Directors:* Laurent Selle
 - *Supervision:* 20% collaboration around the theoretical derivation and interpretation of Volume-averaged porous media equations
 - **Funding:** European ERC project SCIROCCO
 - *Publications:*
 - * P.-A. Masset, O. Dounia and L. Selle, Combustion regimes in inert porous media: From decoupled to hyperdiffusive flames, *Combustion and Flame*, 2022.
 - * P.-A. Masset, O. Dounia and L. Selle, Fully explicit formulae for flame speed in infinite and finite porous media, *Combustion Theory and Modelling*, 2021.

- **Jean-Jacques Hok [2021-2024]**
 - *Title:* Modelling strategy for the Large-Eddy Simulation of lean hydrogen-air explosions
 - *Directors:* Olivier Vermorel, *Co-supervisor:* O. Dounia (50%)
 - **Funding:** LEFEX project funded by TOTALenergie, GRTGAZ and AirLiquid
 - *Publications:*
 - * J.-J. Hok, O. Dounia, O. Vermorel, A Thickened Flame model extension for the simulation of lean hydrogen-air explosions in confined environments, *Combustion and Flame*, *under review*.
 - * J.-J. Hok, O. Dounia, N. Detomaso, T. Jaravel, Q. Douasbin, O. Vermorel, A modeling strategy for the Thickened Flame simulation of propagating lean hydrogen-air flames, *International Journal of Hydrogen Energy*, 2024.

- * N. Detomaso, Jean-Jacques Hok, O. Dounia, D. Laera, T. Poinso, A generalization of the Thickened Flame model for stretched flames, Combustion and Flame, 2023.
- * J.-J. Hok, O. Dounia, O. Vermorel, T. Jaravel, Effect of Flame Front Thermo-Diffusive Instability on Flame Acceleration in a Tube, ICDERS 2022.

- **Nicola Detomaso [2021-2024]**

- *Title:* Large Eddy Simulation of Constant Volume Combustion
- *Directors:* Florent Duchaine , *Co-supervisor:* O. Dounia (33%)
- **Funding:** European MSCA ITN project INSPIRE
- *Publications:*
 - * N. Detomaso, D. Laera, O. Dounia, C. Mocquard, F. Douchaine, T. Poinso, Thickened Flame LES methodology for turbulent propagating flames in non-homogeneous mixtures: application to a constant volume chamber., Proc. Combust. Inst., 2024
 - * N. Detomaso, J.-J. Hok, O. Dounia, D. Laera, T. Poinso, A generalization of the Thickened Flame model for stretched flames, Combustion and Flame, 2023.

- **Patrick Strempl [2021-2024]**

- *Title:* LES of Rotating Detonation Engines: Sensitivity and Physics
- *Directors:* Thierry Poinso , *Co-supervisor:* O. Dounia (50%)
- **Funding:** European MSCA ITN project INSPIRE
- *Publications:*
 - * P. Strempl, O. Dounia, D. Laera, T. Poinso, Effects of mixing assumptions and models for LES of Hydrogen-fueled Rotating Detonation Engines, International Journal of Hydrogen Energy, 2024.

- **Benjamin Vanbersel [2021-2024]**

- *Title:* Méthodes de raffinement de maillage automatique pour les simulations aux grandes échelles d'explosions de gaz
- *Directors:* Laurent Gicquel
- *Supervision:* 10% Collaboration around the LES of deflagration waves
- **Funding:** LEFEX project funded by TOTALÉnergie, GRTGAZ and AirLiquid
- *Publications:*
 - * B. Vanbersel, F. A. M. Ramirez, P. Mohanamuraly, G. Staffelbach, T. Jaravel, Q. Douasbin, O. Dounia, Olivier Vermorel, A systematic Adaptive Mesh Refinement method for Large Eddy Simulation of turbulent flame propagation, Flow Turbulence and Combustion, 2024.

- * B. Vanbersel, F. M. Ramirez, O. Vermorel, T. Jaravel, Q. Douasbin and O. Dounia, Large Eddy Simulations of a H₂-air explosion in a obstacle-laden chamber using Adaptive Mesh Refinement. European Combustion Meeting, 2023.
- * B. Vanbersel, F. M. Ramirez, O. Vermorel, T. Jaravel, Q. Douasbin and O. Dounia, Large eddy simulations of a hydrogen-air explosion in an obstructed chamber using adaptive mesh refinement, International Conference of Hydrogen Safety, 2023.
- **Loic De Nardi [2022-2025]**
 - *Title*: LES of hydrogen deflagrations in obstructed channels
 - *Directors*: T. Poinso, *Co-supervisor*: Q. Douasbin
 - *Supervision*: 20% Supervision around the LES modeling of Hydrogen deflagrations
 - **Funding**: STOHYC project funded by AIRBUS
 - *Publications*:
 - * L. De Nardi, Q. Douasbin, O. Dounia, T. Poinso, LES of H₂/CH₄/air deflagrations in an obstructed channel, Combustion and Flame, *under review*.
 - * L. De Nardi, H. J. V. Ruiz, Q. Douasbin, O. Dounia, T. Poinso, LES Modeling of High-Pressure Nitrogen Cross-Flow Jet Impact on Hydrogen-Air Deflagration, Proceedings of the combustion Institute, 2024.
- **E. M. Mur [2022-2025]**
 - *Title*: LES investigation of the impact of stratification on deflagrations
 - *Directors*: T. Poinso
 - *Supervision*: 33% Supervision around the LES modeling of Hydrogen deflagrations
 - **Funding**: STOHYC project funded by AIRBUS
 - *Publications*:
 - * E. M. Mur, O. Dounia, Q. Douasbin, O. Vermorel, Impact of stratification and global mixture properties on flame acceleration: a numerical study, Combustion and Flame, *under review*.
- **S. Missey [2022-2025]**
 - *Title*: LES investigation of the impact of stratification on deflagrations
 - *Directors*: Laurent Selle
 - *Supervision*: 20% Collaboration around the DNS and theoretical modelling of stratified deflagrations

- **Funding:** ESKHYMO PEPR project
- *Publications:*
 - * S. Missey, O. Dounia, L. Selle, Early-stage flame acceleration in stratified hydrogen-air mixtures: theory and simulation, Proc. Comb. Inst., 2024.

6.2.2 Postdoctoral researchers

- **Antony Cellier [2023-2024]**
 - *Title:* LES modelling of deflagrations in batterie containers and hydrogen storage facilities
 - **Funding:** funded by TOTALEnergies/SAFT
- **Jonathan Wirtz [2023-2024]**
 - *Title:* LES of fast deflgrations: upscaling and impact of dilution
 - **Funding:** funded by EDF

6.2.3 Master Students

- **Kevin Turgut [2024]**
 - *Title:* Analytical chemistry reduction methods for hydrogen combustion
- **Aman Kumar Panda [2023]**
 - *Title:* Implementation of the equations describing flame/inhibiting particles interaction in CANTERA
- **Jean-Jacques Hok [2020]**
 - *Title:* Numerical simulations of outwardly propagating spherical hydrogen flames
- **Benjamin Vanbersel [2020]**
 - *Title:* Adaptive mesh refinement strategies for explosions
- **Barthelemy Picherit [2013]**
 - *Title:* Dynamic subgrid-scale turbulent combustion models for the LES of gas explosions

6.3 Funded Projects (coordination, participation ...)

6.3.1 National and European projects

ANR projects :

- **TRACKDEMO (2023-2027)**

- *Objectives:* Combined experimental and numerical investigation of the shock-to-detonation transition phenomenon
- *Collaboration:* Strong collaboration with PPrime laboratory (Ashwin Chinayya and Vincent Rodriguez)
- *Role:* Principal Investigator on CERFACS side. Participation in writing the proposal, the submission process and coordination of the projet. Supervision of 1 PhD student.

European MSCA ITN projects :

- **H2POWRD (2024-2028)**

- *Objectives:* Consortium of European centers of expertise to train the futur generation of researchers on the fundamentals of rotating detonation propulsion technologies for gas turbine applications. Follow-up on INSPIRE.
- *Collaboration:* Strong collaboration with TU Eindhoven (Xiaocheng Mi)
- *Role:* Principal Investigator on CERFACS side. Participation in writing the proposal, the submission process. Supervision of 1 PhD student.

- **ICHARUS (2023-2027)**

- *Objectives:* Consortium of European centers of expertise to train the futur generation of researchers on the fundamentals of plasma assisted combustion for the control of hydrogen combustion.
- *Collaboration:* Strong collaboration with Imperial College (Andrea Giusti)
- *Role:* Principal Investigator on CERFACS side. Supervision of 1 PhD student.

- **INSPIRE (2020-2024)**

- *Objectives:* Consortium of European centers of expertise to train the futur generation of researchers on the fundamentals of rotating detonation propulsion technologies for gas turbine applications.
- *Role:* Principal Investigator on CERFACS side. Supervision of 2 PhD students.

European ERC projects :

- **SAFE-H2 (2025-2030)**
 - *Objectives:* Fundamentals of hydrogen safety
 - *Role:* Scientific leader for CERFACS
- **SCIROCCO (2019-2024)**
 - *Objectives:* fundamentals of hydrogen combustion in laminar burners and swirled combustion chambers.
 - *Role:* Postdoctoral researcher responsible for the DNS of flame stabilization in porous media. Supervision of 2 PhD students.

Industrial funded projects :

My research activities at CERFACS are also possible thanks to strong collaborations with our industrial partners. Notably, I am in charge of the management of the activities related to safety at CERFACS, among which the coordination of multiple large projects related to safety applications:

- **LEFEX (2019-2024)**
 - *Objectives:* Develop a predictive LES methodology for the reliable simulations of large-scale explosions
 - *Funding :* TOTALEnergie, GRTGAZ and AirLiquid
- **STOHYC**
 - *Objectives:* development of LES capabilities for the prediction of hydrogen fires and explosions in confined areas around aircrafts.
 - *Funding:* AIRBUS
- **Battery Safety**
 - *Objectives:* development of LES capabilities for the prediction of explosions in battery storage facilities.
 - *Funding:* TOTALEnergies and SAFT
- **Mitigation of hydrogen explosions**
 - *Objectives:* Investigation of the impact of diluents and water vapor on hydrogen explosions
 - *Funding:* EDF
- **Novel reduction techniques for combustion chemistry**
 - *Objectives:* Explore alternative kinetic reduction methods for heavy fuels
 - *Funding:* SAFRAN AE

Publications, conferences and lectures

7.1 List of publications

7.1.1 Publications under review

- [1] E. M. Mur, Q. Douasbin, O. Dounia, O. Vermorel, Mechanisms of flame acceleration in stratified hydrogen explosions: a numerical study, *International Journal of Hydrogen Energy*, *under review*.
- [2] J.-J. Hok, O. Dounia, O. Vermorel, A Thickened Flame model extension for the simulation of lean hydrogen-air explosions in confined environments, *Combustion and Flame*, *under review*.
- [3] F. A. M. Ramirez, Q. Douasbin, O. Dounia, O. Vermorel, T. Jaravel, Flame-turbulence interactions in lean hydrogen flames: implications for turbulent flame speed and fractal modelling, *Combustion and Flame*, *under review*.

7.1.2 Accepted Publications

- [1] L. De Nardi, Quentin Douasbin, O. Dounia, T. Poinsot, LES of H₂/CH₄/air deflagrations in an obstructed channel, *Combustion and Flame*, *in press*.
- [2] F. A. M. Ramirez, B. Vanbersel, O. Dounia, T. Jaravel, Q. Douasbin and O. Vermorel, Numerical study of the flame acceleration mechanisms of a lean hydrogen/air deflagration in an obstructed channel, *International Journal of Hydrogen Energy*, 2024.
- [3] N. Detomaso, D. Laera, O. Dounia, C. Mocquard, F. Douchaine, T. Poinsot, “Thickened Flame LES methodology for turbulent propagating flames in non-homogeneous mixtures: application to a constant volume chamber.”, *Proc. Combust. Inst.*, 2024.

-
- [4] L. De Nardi, H. J. V. Ruiz, Q. Douasbin, O. Dounia, Y. Poinso, “LES Modeling of High-Pressure Nitrogen Cross-Flow Jet Impact on Hydrogen-Air Deflagration”, Proc. Comb. Inst., 2024.
- [5] S. Missey, O. Dounia, L. Selle, “Early-stage flame acceleration in stratified hydrogen-air mixtures: theory and simulation”, Proc. Comb. Inst., 2024.
- [6] J.-J. Hok, O. Dounia, N Detomaso, T. Jaravel, Q. Douasbin, O. Vermorel, “A modeling strategy for the Thickened Flame simulation of propagating lean hydrogen-air flames”, International Journal of Hydrogen Energy, 2024 .
- [7] P. Strempl, O. Dounia, D. Laera, T. Poinso, “Effects of mixing assumptions and models for LES of Hydrogen-fueled Rotating Detonation Engines”, International Journal of Hydrogen Energy 62:1-16, 2024.
- [8] B. Vanbersel, F. A. M. Ramirez, P. Mohanamuraly, G. Staffelbach, T. Jaravel, Q. Douasbin, O. Dounia, O. Vermorel, “A systematic Adaptive Mesh Refinement method for Large Eddy Simulation of turbulent flame propagation”, Flow Turbul. Combust. 112:1127-1160, 2024.
- [9] F. Muller, O. Dounia, L. Selle, “Direct Pore-Level Simulation of hydrogen flame anchoring mechanisms in an inert porous media”, Phys. Fluids 36:013336, 2024.
- [10] O. Dounia, “From dilution to catalytic radical scavenging: regime transitions in gas-phase flame inhibition”, Combust. Flame 261:113294, 2024.
- [11] N. Detomaso, J. J. Hok, O. Dounia, D. Laera, T. Poinso, “A generalization of the Thickened Flame model for stretched flames”, Combust. Flame, 258:113080, 2023.
- [12] P. A. Masset, O. Dounia, L. Selle, “Combustion regimes in inert porous media: From decoupled to hyperdiffusive flames”, Combust. Flame, 241:112052, 2022.
- [13] O. Dounia, T. Jaravel, O. Vermorel, “On the controlling parameters of the thermal decomposition of inhibiting particles: A theoretical and numerical study”, Combust. Flame 240:11991, 2022.
- [14] T. Jaravel, O. Dounia, Q. Malé, O. Vermorel, “Deflagration to detonation transition in fast flames and tracking with chemical explosive mode analysis”, Proc. Combust. Inst. 38:3529-3536, 2021.
- [15] O. Dounia, O. Vermorel, T. Jaravel, T. Poinso, “Time scale analysis of the homogeneous flame inhibition by alkali metals”, Proc. Combust. Inst. 38:2371-2378, 2021.
- [16] P. A. Masset, O. Dounia, L. Selle, “Fully-explicit formulae for flame speed in infinite and finite porous media”, Combust. Theo. Model., 25:785-812, 2020.
- [17] O. Dounia, O. Vermorel, A. Misdariis, T. Poinso, “Influence of kinetics on DDT”, Combust Flame 200:1-14, 2019.

- [18] O. Dounia, O. Vermorel, T. Poinso, “Theoretical analysis and simulation of methane/air flame inhibition by sodium bicarbonate particles”, *Combust. Flame* 193:313-326, 2018.

7.1.3 Refereed conference paper

- [1] Francis Adrian Meziat Ramirez, Omar Dounia, Thomas Jaravel, Quentin Douasbin and Olivier Vermorel, Towards the LES of large-scale explosions: study of a larger-than-laboratory-scale H₂/air vented explosion, 15th International Symposium on Hazards, Prevention and Mitigation of Industrial Explosions, 2024.
- [2] B. Vanbersel, F. A. M. Ramirez, O. Vermorel, T. Jaravel, Q. Douasbin, O. Dounia, Large Eddy Simulations of a H₂-air explosion in an obstacle-laden chamber using Adaptive Mesh Refinement, European Combustion Meeting, 2023.
- [3] B. Vanbersel, F. A. Meziat Ramirez, O. Vermorel, T. Jaravel, Q. Douasbin, And O. Dounia, Large Eddy Simulations of a Hydrogen-Air Explosion in an Obstructed Chamber Using Adaptive Mesh Refinement, Int. Conf. Hydrogen Safety, 2023.
- [4] Jean-Jacques Hok, Omar Dounia, Olivier Vermorel, Thomas Jaravel, Effect of Flame Front Thermo-Diffusive Instability on Flame Acceleration in a Tube, Proc. Int. Colloq. Dyn. Explosions Reac. Syst. (ICDERS), 2022.

7.2 Invited talks

- [1] O. Dounia, Hydrogen, from deflagration to detonation. Hydrogen week in Toulouse: towards high pressure experiments and simulations, 2024.
- [2] O. Dounia, Advances in the LES of flame acceleration and DDT, European Combustion Meeting Workshop, Rouen (2023)
- [3] O. Dounia, Modeling of the inhibition of propagating flames, CFD for Combustion Safety Workshop, Toulouse, (2023).
- [4] O. Dounia, E. Riber, Towards decarbonizing industry and aviation: Modeling and Simulation of SAF and H₂ turbulent flames, Institute For Sustainable Aviation, ISAE SUPAERO, Toulouse (2023).
- [5] O. Dounia, Flame Acceleration mechanisms in H₂/air flames, HYRESPONDER workshop, CEA, Grenoble (2023).
- [6] O. Dounia, DNS of detonation re-initiation at the Chapman-Jouguet deflagration regime, The Young Researchers’ Forum on Detonation (2021). Recorded intervention

Bibliography

- [1] J. Goulier. ‘Comportements aux limites de flammes de prémélange hydrogène/air. Étude de la transition flamme laminaire-flamme turbulente’. PhD thesis. Université d’Orléans, Orléans, France, 2015.
- [2] Jean-Jacques Hok, Omar Dounia, Nicola Detomaso, Thomas Jaravel, Quentin Douasbin and Olivier Vermorel. ‘A modeling strategy for the Thickened Flame simulation of propagating lean hydrogen–air flames’. In: International Journal of Hydrogen Energy 78 (2024), pp. 1133–1141.
- [3] Pierre Pelce and Paul Clavin. ‘Influence of hydrodynamics and diffusion upon the stability limits of laminar premixed flames’. In: Journal of Fluid Mechanics (1982), pp. 425–443.
- [4] Jiao Yuan, Yiguang Ju and Chung K. Law. ‘Coupled hydrodynamic and diffusional-thermal instabilities in flame propagation at subunity Lewis numbers’. In: Physics of Fluids 17.7 (2005), pp. 1–10.
- [5] Y. Rastigejev and M. Matalon. ‘Nonlinear evolution of hydrodynamically unstable premixed flames’. In: Journal of Fluid Mechanics 554 (2006), pp. 371–392.
- [6] Moshe Matalon. ‘The Darrieus-Landau instability of premixed flames’. In: Fluid Dynamics Research 50.5 (2018).
- [7] C. Altantzis, C. E. Frouzakis, A. G. Tomboulides, M. Matalon and K. Boulouchos. ‘Hydrodynamic and thermodiffusive instability effects on the evolution of laminar planar lean premixed hydrogen flames’. In: Journal of Fluid Mechanics 700.June (2012), pp. 329–361.
- [8] T. L. Howarth and A. J. Aspden. ‘An empirical characteristic scaling model for freely-propagating lean premixed hydrogen flames’. In: Combustion and Flame 237 (2022), p. 111805.
- [9] Moshe Matalon and B. J. Matkowsky. ‘On the stability of plane and curved flames’. In: SIAM Journal of Applied Mathematics 44.2 (1984), pp. 327–343.
- [10] J. K. Bechtold and M. Matalon. ‘Hydrodynamic and diffusion effects on the stability of spherically expanding flames’. In: Combustion and Flame 67.1 (1987), pp. 77–90.

- [11] R. Addabbo, J. K. Bechtold and M. Matalon. ‘Wrinkling of spherically expanding flames’. In: Proceedings of the Combustion Institute 29.2 (2002), pp. 1527–1535.
- [12] D. Bradley, C. G.W. Sheppard, R. Woolley, D. A. Greenhalgh and R. D. Lockett. ‘The development and structure of flame instabilities and cellularity at low Markstein numbers in explosions’. In: Combustion and Flame 122.1-2 (2000), pp. 195–209.
- [13] Moshe Matalon. ‘Intrinsic flame instabilities in premixed and nonpremixed combustion’. In: Annual Review of Fluid Mechanics 39 (2007), pp. 163–191.
- [14] Jean-Jacques Hok, Omar Dounia, Olivier Vermorel and Thomas Jaravel. ‘Effect of Flame Front Thermo-Diffusive Instability on Flame Acceleration in a Tube’. In: Proceedings of the 28th ICDERS. 2022, pp. 1–6.
- [15] Christophe Clanet and Geoffrey Searby. ‘On the "Tulip Flame" Phenomenon’. In: Combustion and Flame 105.225 (1996).
- [16] Vitaly Bychkov, V’yacheslav Akkerman, Gordon Fru, Arkady Petchenko and Lars-Erik Eriksson. ‘Flame acceleration in the early stages of burning in tubes’. In: Combustion and Flame 150.4 (2007), pp. 263–276.
- [17] Damir M. Valiev, V’yacheslav Akkerman, Mikhail Kuznetsov, Lars Erik Eriksson, Chung K. Law and Vitaly Bychkov. ‘Influence of gas compression on flame acceleration in the early stage of burning in tubes’. In: Combustion and Flame 160.1 (2013), pp. 97–111.
- [18] T. D. Butler and P. J. O’Rourke. ‘A numerical method for two dimensional unsteady reacting flows’. In: Symposium (International) on Combustion 16.1 (1977), pp. 1503–1515.
- [19] P.J. O’Rourke and F.V. Bracco. ‘Two Scaling Transformations for the Numerical Computation of Multidimensional Unsteady Laminar Flames’. In: Journal of Computational Physics 203 (1979), pp. 185–203.
- [20] Forman A. Williams. Combustion Theory. Second. CRC Press, 1994.
- [21] Kenneth K. Kuo. Fundamentals of Turbulent and Multiphase Turbulent Combustion. Hoboken, NJ : John Wiley, 2012.
- [22] J. P. Legier, Thierry Poinot and Denis Veynante. ‘Dynamically thickened flame LES model for premixed and non-premixed turbulent combustion’. In: Proceedings of the Summer Program, Centre for Turbulence Research (2000), pp. 157–168.
- [23] William B Bush and Francis E Fendell. ‘Asymptotic Analysis of Laminar Flame Propagation for General Lewis Numbers’. In: Combustion Science and Technology 1 (1970), pp. 421–428.
- [24] P Clavin and G Joulin. ‘Premixed flames in large scale and high intensity turbulent flow’. In: Journal de Physique Lettres 44.1 (1983), pp. 1–12.
- [25] Paul Clavin and Pedro Garcia. ‘The influence of the temperature dependence of diffusivities on the dynamics of flame fronts’. In: Journal de Physique Théorique et Appliquée 2.2 (1983), pp. 245–263.

- [26] George K. Giannakopoulos, Christos E. Frouzakis, Shikhar Mohan, Ananias G. Tomboulides and Moshe Matalon. ‘Consumption and displacement speeds of stretched premixed flames - Theory and simulations’. In: Combustion and Flame 208 (2019), pp. 164–181.
- [27] Francis Adrian Meziat Ramirez, Benjamin Vanbersel, Omar Dounia, Thomas Jaravel, Quentin Douasbin and Olivier Vermorel. ‘Intrinsic instabilities in premixed hydrogen flames: parametric variation of pressure, equivalence ratio, and temperature. Part 2 – Non-linear regime and flame speed enhancement’. In: International Journal of Hydrogen Energy Accepted (2024).
- [28] Pierre Quillatre. ‘Simulation aux grandes echelles d’explosions en domaine semi-confine’. PhD thesis. Université de Toulouse, Toulouse, France, 2014.
- [29] Pedro S. Volpiani, Thomas Schmitt, Olivier Vermorel, Pierre Quillatre and Denis Veynante. ‘Large eddy simulation of explosion deflagrating flames using a dynamic wrinkling formulation’. In: Combustion and Flame 186 (2017), pp. 17–31.
- [30] Lukas Berger, Antonio Attili and Heinz Pitsch. ‘Intrinsic instabilities in premixed hydrogen flames: parametric variation of pressure, equivalence ratio, and temperature. Part 2 – Non-linear regime and flame speed enhancement’. In: Combustion and Flame 240 (2022), p. 111936.
- [31] Nicola Detomaso, Jean-jacques Hok, Omar Dounia, Davide Laera and Thierry Poinot. ‘A generalization of the Thickened Flame model for stretched flames’. In: Combustion and Flame 258 (2023), p. 113080.
- [32] Jean Jacques Hok. ‘Modelling strategy for the Large-Eddy Simulation of lean hydrogen-air explosions’. PhD thesis. Université de Toulouse, Toulouse, France, 2014.
- [33] P. Katzy. ‘Combustion Model for the Computation of Flame Propagation in Lean Hydrogen-Air Mixtures at Low Turbulence’. PhD thesis. 2021.
- [34] D Zivkovic and T Sattelmayer. ‘Fractal-based RANS Modeling of Darrieus – Landau and Thermal-diffusive Instability Effects on Lean Hydrogen Flames’. In: Proceedings of the 28th ICDERS. 2. 2022, pp. 1–6.
- [35] Fabrice Charlette, Charles Meneveau and Denis Veynante. ‘A power-law flame wrinkling model for LES of premixed turbulent combustion Part I: Non-dynamic formulation and initial tests’. In: Combustion and Flame 131.1-2 (2002), pp. 159–180.
- [36] Andrei N. Lipatnikov, Hsu Chew Lee, Peng Dai, Minping Wan and Vladimir A. Sabelnikov. ‘Transition from turbulence-dominated to instability-dominated combustion regime in lean hydrogen-air flames’. In: Combustion and Flame 259.November 2023 (2024), p. 113170.
- [37] T. L. Howarth, E. F. Hunt and A. J. Aspden. ‘Thermodiffusively-unstable lean premixed hydrogen flames: Phenomenology, empirical modelling, and thermal leading points’. In: Combustion and Flame 253 (2023), p. 112811.

- [38] Sebastien Missey, Omar Dounia and Laurent Selle. ‘Early stage flame acceleration in stratified hydrogen air mixtures: Theory and simulation’. In: Proceedings of the Combustion Institute 40.1 (2024), p. 105279.
- [39] E. Matas Mur, Omar Dounia, Quentin Douasbin and Olivier Vermorel. ‘Impact of stratification and global mixture properties on flame acceleration: a numerical study’. In: International Journal of Hydrogen Energy (Under Review).
- [40] Lorenz R. Boeck, Peter Katzy, Josef Hasslberger, Andreas Kink and Thomas Sattelmayer. ‘The GraVent DDT database’. In: Shock Waves 26 (5 Sept. 2016), pp. 683–685.
- [41] Olivier Colin and Michael Rudgyard. ‘Development of High-Order Taylor-Galerkin Schemes for LES’. In: Journal of Computational Physics 162 (2 Aug. 2000), pp. 338–371.
- [42] Priyank Saxena and Forman A. Williams. ‘Testing a small detailed chemical-kinetic mechanism for the combustion of hydrogen and carbon monoxide’. In: Combustion and Flame 145 (1-2 Apr. 2006), pp. 316–323.
- [43] F Nicoud and F Ducros. ‘Subgrid-Scale Stress Modelling Based on the Square of the Velocity Gradient Tensor’. In: Flow, Turbulence and Combustion 62 (1999), pp. 183–200.
- [44] Lukas Berger, Antonio Attili and Heinz Pitsch. ‘Intrinsic instabilities in premixed hydrogen flames: parametric variation of pressure, equivalence ratio, and temperature. Part 2 – Non-linear regime and flame speed enhancement’. In: Combustion and Flame 240 (June 2022).
- [45] Lorenz R. Boeck, Josef Hasslberger and Thomas Sattelmayer. ‘Flame acceleration in hydrogen/air mixtures with concentration gradients’. In: Combustion Science and Technology 186 (10-11 Nov. 2014), pp. 1650–1661.
- [46] John H. S. Lee. The Detonation Phenomenon. Cambridge University Press, 2008.
- [47] O. Dounia, O. Vermorel, A. Misdariis and T. Poinso. ‘Influence of kinetics on DDT simulations’. In: Combustion and Flame 200 (2019), pp. 1–14.
- [48] M. S. A. Ahmed. ‘Run-Up Distance From Deflagration to Detonation In Fast Flames’. PhD thesis. University of Ottawa, Ottawa, Canada, 2016.
- [49] Mohamed Saif, Wentian Wang, Andrzej Pekalski, Marc Levin and Matei I. Radulescu. ‘Chapman–Jouguet deflagrations and their transition to detonation’. In: Proceedings of the Combustion Institute 36.2 (2017), pp. 2771–2779.
- [50] T. Jaravel, O. Dounia, Q. Malé and O. Vermorel. ‘Deflagration to detonation transition in fast flames and tracking with chemical explosive mode analysis’. In: Proceedings of the Combustion Institute 38.3 (2021), pp. 3529–3536.
- [51] Alejandro Millán-Merino, Said Taileb and Pierre Boivin. ‘A new method for systematic 1-step chemistry reduction applied to hydrocarbon combustion’. In: Proceedings of the Combustion Institute 39.1 (2023), pp. 745–753.

- [52] Dimitris A. Goussis, Hong G. Im, Habib N. Najm, Samuel Paolucci and Mauro Valorani. ‘The origin of CEMA and its relation to CSP’. In: Combustion and Flame 227 (2021), pp. 396–401.
- [53] Zhaoyu Luo, Chun Sang Yoo, Edward S. Richardson, Jacqueline H. Chen, Chung K. Law and Tianfeng Lu. ‘Chemical explosive mode analysis for a turbulent lifted ethylene jet flame in highly-heated coflow’. In: Combustion and Flame 159.1 (2012), pp. 265–274.
- [54] Chao Xu, Ji Woong Park, Chun Sang Yoo, Jacqueline H. Chen and Tianfeng Lu. ‘Identification of premixed flame propagation modes using chemical explosive mode analysis’. In: Proceedings of the Combustion Institute 37.2 (2019), pp. 2407–2415.
- [55] T. F. Lu, C. S. Yoo, J. H. Chen and C. K. Law. ‘Three-dimensional direct numerical simulation of a turbulent lifted hydrogen jet flame in heated coflow: A chemical explosive mode analysis’. In: Journal of Fluid Mechanics 652. September 2015 (2010), pp. 45–64.
- [56] D. Trees and K. Seshadri. ‘Experimental Studies of Flame Extinction by Sodium Bicarbonate (NaHCO₃) Powder’. In: Combust. Sci. Technol. 122 (1997), pp. 215–230.
- [57] W. M. Pitts, J. C. Yang, R. A. Bryant, L. G. Blevins and M. L. Huber. ‘Characteristics and Identification of Super-Effective Thermal Fire-Extinguishing Agents’. <https://apps.dtic.mil/sti/citations/ADA418433>. 2001.
- [58] R. G. Gann. ‘The Final Report of the Next Generation Fire Suppression Technology Program’. In: NIST Technical Report (2007).
- [59] Gregory T. Linteris, Marc D. Rumminger and Valeri I. Babushok. ‘Catalytic inhibition of laminar flames by transition metal compounds’. In: Prog. Energy Comb. Sci. 34 (2008), pp. 288–329.
- [60] D. Roosendans and P. Hoorelbeke. ‘Industrial system for mitigation of vapor cloud explosions’. In: J. Loss. Prevent. Proc. 68 (2020), p. 104273.
- [61] Omar Dounia, Olivier Vermorel and Thierry Poinso. ‘Theoretical analysis and simulation of methane/air flame inhibition by sodium bicarbonate particles’. In: Combust. Flame 193 (2018), pp. 313–326.
- [62] O. Dounia, O. Vermorel, T. Jaravel and T. Poinso. ‘Time scale analysis of the homogeneous flame inhibition by alkali metals’. In: Proc. Combust. Inst. 38 (2021), pp. 2371–2378.
- [63] Omar Dounia, Thomas Jaravel and Olivier Vermorel. ‘On the controlling parameters of the thermal decomposition of inhibiting particles: A theoretical and numerical study’. In: Combust. Flame 240 (2022), p. 111991.
- [64] O. Dounia. ‘From dilution to catalytic radical scavenging: Regime transitions in gas-phase flame inhibition’. In: Combustion and Flame 261 (2024), p. 113294.
- [65] H.K. Chelliah, P.C. Wanigarathne, A.M. Lentati, R.H. Krauss and G.S. Fallon. ‘Effect of sodium bicarbonate particle size on the extinction condition of non-premixed counterflow flames’. In: Combust. Flame 134 (2003), pp. 261–272.

- [66] VI Babushok, KL McNesby, AW Miziolek and RR Skaggs. ‘Modeling of synergistic effects in flame inhibition by 2-H heptafluoropropane blended with sodium bicarbonate’. In: Combust. Flame 133 (2003), pp. 201–205.
- [67] Valeri I. Babushok, Gregory T. Linteris, Pol Hoorelbeke, Dirk Roosendans and Kees van Wingerden. ‘Flame Inhibition by Potassium-Containing Compounds’. In: Combust. Sci. Technol. 189 (2017), pp. 2039–2055.
- [68] V Babushok. ‘Chemical limits to flame inhibition’. In: Combust. Flame 115 (1998), pp. 551–560.
- [69] G. Dixon-Lewis and R.J. Simpson. ‘Aspects of flame inhibition by halogen compounds’. In: Symp. (Int.) Combust. 16 (1977), pp. 1111–1119.
- [70] G. Dixon-Lewis. ‘Mechanism of inhibition of hydrogen-air flames by hydrogen bromide and its relevance to the general problem of flame inhibition’. In: Combust. Flame 36 (1979), pp. 1–14.
- [71] R.M. Fristrom and P. Van Tiggelen. ‘An interpretation of the inhibition of C–H–O flames by C–H–X compounds’. In: Symp. (Int.) Combust. 17 (1979), pp. 773–785.
- [72] David E. Jensen and George A. Jones. ‘Kinetics of flame inhibition by sodium’. In: J. Chem. Soc., Faraday Trans. I 78 (1982), pp. 2843–2850.
- [73] Marc D. Rumminger and Gregory T. Linteris. ‘Inhibition of premixed carbon monoxide–hydrogen–oxygen–nitrogen flames by iron pentacarbonyl’. In: Combust. Flame 120 (2000), pp. 451–464.
- [74] P.J. Padley and T.M. Sugden. ‘Chemiluminescence and radical re-combination in hydrogen flames’. In: Symp. (Int.) Combust. 7 (1958), pp. 235–242.
- [75] Ya. B. Zeldovich. ‘Chain reactions in hot flames – an approximate theory of flame velocity’. In: Kinet. Katal. 11 (1961), pp. 305–318.
- [76] P. Clavin and G. Searby. Combustion Waves and Fronts in Flows. Cambridge University Press, 2016.
- [77] P. Boivin, C. Jiménez, A.L. Sánchez and F.A. Williams. ‘An explicit reduced mechanism for H₂–air combustion’. In: Proc. Combust. Inst. 33 (2011), pp. 517–523.
- [78] D. Fernández-Galisteo, A.L. Sánchez, A. Liñán and F.A. Williams. ‘One-step reduced kinetics for lean hydrogen–air deflagration’. In: Combust. Flame 156 (2009), pp. 985–996.
- [79] T. Noto, V. Babushok, A. Hamins and W. Tsang. ‘Inhibition effectiveness of halogenated compounds’. In: Combust. Flame 112 (1998), pp. 147–160.
- [80] Matthijs van Wingerden, Trygve Skjold, Dirk Roosendans, Antoine Dutertre and Andrzej Pekalski. ‘Chemical inhibition of hydrogen-air explosions: Literature review, simulations and experiments’. In: Process Saf. Environ. 176 (2023), pp. 1120–1129.
- [81] J. W. Dold. ‘Premixed flames modelled with thermally sensitive intermediate branching kinetics’. In: Combust. Theor. Model. 11 (2007), pp. 909–948.

- [82] P. Clavin and G. Searby. ‘Unsteady response of chain-branching premixed-flames to pressure waves’. In: Combust. Theor. Model. 12 (2008), pp. 545–567.
- [83] Paul Clavin and José C. Graña-Otero. ‘Curved and stretched flames: the two Markstein numbers’. In: Journal of Fluid Mechanics 686 (2011), pp. 187–217.
- [84] P.-A. Masset, O. Dounia and L. Selle. ‘Combustion regimes in inert porous media: From decoupled to hyperdiffusive flames’. In: Combustion and Flame 241 (2022), p. 112052.
- [85] P.-A. Masset, O. Dounia and L. Selle. ‘Fully explicit formulae for flame speed in infinite and finite porous media’. In: Combustion Theory and Modelling 25.5 (2021), pp. 785–812.
- [86] F Pereira, A Oliveira and F Fachini. ‘Asymptotic analysis of stationary adiabatic premixed flames in porous inert media’. In: Combust. Flame 156.1 (2009), pp. 152–165.
- [87] F Pereira, A Oliveira and F Fachini. ‘Theoretical analysis of ultra lean premixed flames in porous inert media’. In: J. Fluid Mech. 657 (2010), pp. 285–307.
- [88] F. Muller, O. Dounia and L. Selle. ‘Direct pore-level simulation of hydrogen flame anchoring mechanisms in an inert porous media’. In: Physics of Fluids 36.1 (Jan. 2024), p. 013336.
- [89] Pierre-Alexandre Masset, Florent Duchaine, Antoine Pestre and Laurent Selle. ‘Modelling challenges of volume-averaged combustion in inert porous media’. In: Combustion and Flame 251 (2023), p. 112678.
- [90] N. Detomaso, D. Laera, O. Dounia, C. Mocquard, F. Duchaine and T. Poinso. ‘Thickened Flame LES methodology for turbulent propagating flames in non-homogeneous mixtures: application to a constant volume chamber’. In: Proceedings of the Combustion Institute 40.1 (2024), p. 105237.
- [91] Laure Labarrere, Thierry Poinso, Antoine Dauplain, Florent Duchaine, Marc Bellenoue and Bastien Boust. ‘Experimental and numerical study of cyclic variations in a Constant Volume Combustion chamber’. In: Combust. Flame 172 (2016), pp. 49–61.
- [92] Nicola Detomaso, Davide Laera, Paul Pouech, Florent Duchaine and Thierry Poinso. ‘Large Eddy Simulation of a Pistonless Constant Volume Combustor: A New Concept of Pressure Gain Combustion’. In: J. Eng. Gas Turbines Power 145.2 (2023), pp. 1–10.
- [93] Clément Mocquard, Davide Laera, Jérôme Dombard and Thierry Poinso. ‘A two-step chemical scheme for auto-igniting and propagating kerosene flames at reheat conditions’. In: Combust. Flame 248 (2023), p. 112558.
- [94] Eric Bach, C.O. Paschereit, Panagiotis Stathopoulos and Myles D. Bohon. ‘An empirical model for stagnation pressure gain in rotating detonation combustors’. In: Proceedings of the Combustion Institute 38.3 (2021), pp. 3807–3814.

-
- [95] P. Strempl, O. Dounia, D. Laera and T. Poinso. ‘Effects of mixing assumptions and models for LES of Hydrogen-fueled Rotating Detonation Engines’. In: International Journal of Hydrogen Energy 62 (2024), pp. 1–16.
- [96] F. Ducros, F. Nicoud and T. Poinso. ‘Wall-Adapating Local eddy-Viscosity models for simulations in complex geometries’. In: ICFD. 1998, pp. 293–300.
- [97] Franck Nicoud, Hubert Baya Toda, Olivier Cabrit, Sanjeeb Bose and Jungil Lee. ‘Using singular values to build a subgrid-scale model for large eddy simulations’. In: Physics of Fluids 23.8 (Aug. 2011), p. 085106.
- [98] S. Kawai and S.K. Lele. ‘Localized artificial diffusivity scheme for discontinuity capturing on curvilinear meshes’. In: Journal of Computational Physics 227.22 (2008), pp. 9498–9526.
- [99] Loïc De Nardi, Héctor José Vargas Ruiz, Quentin Douasbin, Omar Dounia and Thierry Poinso. ‘LES Modeling of High-Pressure Nitrogen Cross-Flow Jet Impact on Hydrogen-Air Deflagration’. In: Proceedings of the Combustion Institute 40.1 (2024), p. 105263.
- [100] Alejandro Millán-Merino and Pierre Boivin. ‘A new single-step mechanism for hydrogen combustion’. In: Combustion and Flame 268 (2024), p. 113641.
- [101] Joshua A.T. Gray and Deanna A. Lacoste. ‘Enhancement of the transition to detonation of a turbulent hydrogen–air flame by nanosecond repetitively pulsed plasma discharges’. In: Combustion and Flame 199 (2019), pp. 258–266.
- [102] Joshua A.T. Gray and Deanna A. Lacoste. ‘Effect of the plasma location on the deflagration-to-detonation transition of a hydrogen–air flame enhanced by nanosecond repetitively pulsed discharges’. In: Proceedings of the Combustion Institute 38.3 (2021), pp. 3463–3472.
- [103] Mhedine Ali Cherif, Sergey A. Shcherbanev, Svetlana M. Starikovskaia and Pierre Vidal. ‘Effect of non-equilibrium plasma on decreasing the detonation cell size’. In: Combustion and Flame 217 (2020), pp. 1–3.